Search for right-handed W bosons and heavy neutrinos with the ATLAS experiment

Neofytos Themistokleous

A thesis presented for the degree of
Doctor of Philosophy

School of Physics and Astronomy
The University of Edinburgh
2023

Abstract

A search for heavy right-handed Majorana or Dirac neutrinos (N_R) and heavy right-handed W bosons (W_R) participating in the Keung-Senjanović (KS) process has been performed in events with a pair of energetic electrons or muons and two energetic jets. Events were selected from pp collision data with an integrated luminosity of 139 fb^{-1} collected by the ATLAS detector at $\sqrt{s}$ = 13 TeV. No significant deviations from the Standard Model expectation were observed. The results are interpreted within the theoretical framework of the Left-Right Symmetric Models (LRSM) and lower limits are set on masses of the W_R and N_R. For Majorana electron neutrinos, the excluded region extends to a W_R mass of 5.6 TeV and a N_R mass of 3.4 TeV. For Majorana muon neutrinos, W_R masses of up to 5.7 TeV are excluded, and N_R masses of up to 3.6 TeV. For Dirac electron neutrinos, the excluded region extends to a W_R mass of 6 TeV and to a N_R mass of 3.5 TeV. For Dirac muon neutrinos, W_R masses of up to 5.8 TeV are excluded, and N_R masses of up to 3.7 TeV. These limits improve upon previous results in the bibliography and are currently the most stringent in the world.

Lay summary

The Standard Model (SM), which currently offers the best description of particle physics at the smallest scales, agrees with experimental observation to a high degree of precision in almost all the ways that scientists have been able to test it. A class of particles known as neutrinos, however, is incorrectly described by the Standard Model for historical reasons. It was believed that neutrinos had no mass when the Standard Model was developed, but subsequent experiments have shown that they actually have very small masses.

It is possible to add a neutrino mass description to the Standard Model in several different ways. This thesis focuses on the combination of the Left-Right Symmetric Models (LRSM) and the SeeSaw Mechanism, as one such extension.

The SeeSaw Mechanism proposes that the masses of the known neutrinos are inversely proportional to the masses of some new, as-yet-undiscovered neutrinos. If the new neutrinos are heavy, it could provide an explanation for the unusually small mass of neutrinos in the SM. This could be compared to a SeeSaw, where the heavy neutrinos and light neutrinos balance each other.

In the Standard Model, forces act between particles by the exchange of force-carrying particles called 'bosons'. A remarkable property of the weak nuclear force, one of the fundamental forces described by the SM, is that, unlike other fundamental forces, it behaves differently toward a system than it would toward the mirror-reflected image of the same system. This occurs because the weak force bosons are left-handed - referring to their "chirality", a specific quantum mechanical attribute of particles. Keeping in mind that only particles of the same handedness may interact, the weak force only affects particles that are "left-handed".

The LRSM extend the weak force to include a right-handed component. The right-handed bosons proposed within LRSM must be heavy in comparison to the left-handed weak bosons to explain why we do not observe right-handed weak interactions occurring in nature, at much lower energy scales. Due to the equivalence of mass and energy, it takes a lot of energy to produce such heavy particles. If these heavy particles exist, it might be possible for them to be created in the Large Hadron Collider, the most powerful particle accelerator and collider in the world.

Data acquired by the ATLAS detector, one of the experiments at the Large Hadron Collider, was analysed in this thesis to look for evidence that one kind of LRSM right-handed boson, W_R, and new heavy neutrinos, N_R, had been generated. The range of W_R and N_R masses that may be produced by proton - proton collisions at the LHC is constrained by the energy at which these collisions take place and the amount of data collected. There was no evidence that these hypothesised particles were produced in the dataset collected. We can conclude with some degree of certainty that if they exist, they must be heavier than the range of W_R and N_R masses that have been explored with the existing collision energy of the Large Hadron Collider due to the non-observation of W_R and N_R.

Declaration

I declare that this thesis was composed by myself, that the work contained herein is my own except where explicitly stated otherwise in the text, and that this work has not been submitted for any other degree or professional qualification except as specified.

Parts of this work have been published in [1] while other parts are in the process of being published under the name: "Search for heavy Majorana or Dirac neutrinos and right-handed W_R gauge bosons in final states with charged leptons and jets at $\sqrt{s} = 13$ TeV with the ATLAS detector".

Acknowledgements

To begin with, I would like to express my gratitude to my supervisor, for his unwavering support during this journey. His trust in me to lead an analysis team and freedom to make independent decisions, while also being available for guidance, have been invaluable in my learning and growth. Thank you, Christos; looking forward to being your Facebook friend!

I was fortunate to have the opportunity and collaborate closely with Benjamin Wynne, whose advice and assistance have been instrumental during this adventure. His knowledge and experience in the field have been a constant source of guidance and support, and I have greatly benefitted from his expertise and insight.

I am grateful for the contributions and support of all members of my analysis team and group conveners. Their professionalism and cooperation have played a significant role in the success of our project. In addition, I would like to extend a special thank you to the ATLAS trigger community for their patience, the stimulating working environment, and for providing some of the most memorable moments of my PhD experience.

I am also thankful for the support of the University of Edinburgh, whose *Principal's Career Development* scholarship provided me with the opportunity to live and study in Edinburgh in the first place.

Contents

Acronyms

KS Keung-Senjanović. iii, xi, 1, 5, 15, 22–24, 63, 65, 66, 69, 71, 75, 85, 93, 107, 108, 112, 115, 117

LRSM Left-Right Symmetric Models. iii, v, vi, 1, 5, 15–24, 63, 69, 117

ID inner detector. xii, 29–35, 37, 42, 75–77, 80

TRP Trigger Rate Presenter. xii, 49–51, 53–59

SM Standard Model of particle physics. 1, 5–7, 10, 13–15, 17, 36, 48, 65, 71, 117

BSM Beyond the Standard Model. 1, 25, 29, 65

VEV Vacuum Expectation Value. 18, 19, 21, 71

LHC Large Hadron Collider. 25–30, 34

IP interaction point. 27, 28, 32, 41

MS muon spectrometer. 29–31, 41, 47, 77, 80

IS ATLAS Information Service. 49, 50, 54, 55, 57, 58

Introduction

The Standard Model of particle physics (SM) despite its remarkable success still faces a number of shortcomings. Searching for evidence of new, Beyond the Standard Model (BSM) physics is one of the main objectives of the ATLAS experiment at the Large Hadron Collider (LHC). The Left-Right Symmetric Models (LRSM) are one class of BSM theories that the ATLAS experiment is exploring. These theories are appealing for a variety of reasons. They can provide a reasonable explanation for the small masses of the known neutrinos and restore parity to the SM, by introducing a right-handed component to the left-handed weak force. LRSM predict the existence of heavy right-handed W bosons (W_R) and heavy right-handed neutrinos (N_R). The heavy right-handed neutrinos may be Dirac or Majorana particles (i.e. their own antiparticle), depending on the class of the LRSM.

This thesis presents an analysis that searches for evidence of W_R and N_R using data collected by the ATLAS experiment during Run2 (between the years 2015 - 2018). The target of the analysis is the Keung-Senjanović (KS) process, in which a proton-proton collision produces an initial W_R, which then decays to an N_R and a charged lepton; the latter then decays to a second W_R and a second charged lepton. We explore the case when the second W_R decays to a quark pair, giving rise to a "two leptons plus two jets" experimental signature. The mass hierarchy (which of the W_R or N_R particles is heavier) of the two BSM particles dictates whether the first or second W_R in the decay chain is off-shell. I and a few other members of a small analysis team within the ATLAS collaboration carried out the analysis.

In Part I, the foundations of the work in this thesis are laid out. The theoretical background of the analysis can be found in Chapter 1. Then, Chapter 2 describes the ATLAS detector with which the dataset used in the analysis was gathered.

Part II contains an introduction to the ATLAS trigger (Chapter 3) and a breakdown of my Trigger contributions in the experiment (Chapter 4).

Part III presents a search for heavy right-handed Majorana or Dirac neutrinos (N_R) and heavy right-handed W gauge bosons (W_R) participating in the KS process. Chapter 5 includes an introduction to the analysis and a description of my involvement in it, while Chapter 6 discusses the experimental and simulated datasets used. Chapter 7 contains the definitions of reconstructed objects used in the analysis and the event selection. Then in Chapter 8, the background estimation is explained, followed by the statistical analysis in Chapter 9. Finally, the results are presented and described in Chapter 10.

Part I

Foundations

Chapter 1

Theoretical Background

> *“There’s atoms, which is things that is too small to see, that’s what we’re all made of. And there’s things that are smaller than atoms, and that’s Particle Physics."*
>
> *Bod nodded and decided that Scarlett’s father was probably interested in imaginary things.*
>
> Neil Gaiman, The Graveyard Book

In this chapter, the theoretical background for the work in this thesis is presented. Initially, the Standard Model of particle physics (SM) and a selection of its issues are briefly introduced in sections 1.1 and 1.2. In section 1.3 the Dirac and Majorana mechanisms for generating fermion mass are mentioned, while sections 1.4 and 1.5 discuss the Left-Right symmetric models and the SeeSaw mechanism, focusing on how they can address the previously highlighted SM issues. Section 1.6 concludes this chapter’s discussion with a description of a process that is of interest in this thesis, the Keung-Senjanović (KS) process. It is an interaction predicted by the combination of the LRSM and the SeeSaw mechanism.

Throughout this chapter and the rest of this thesis, natural units in which Planck’s constant (h) = the speed of light in vacuum (c) = 1 will be used for convenience.

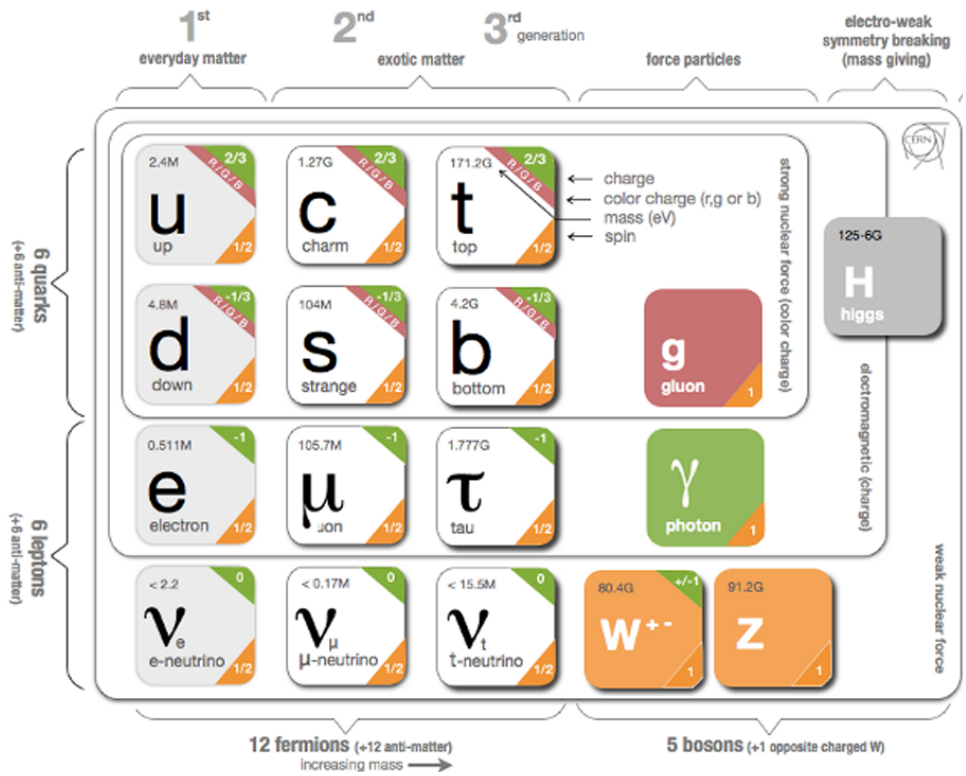

Figure 1.1: The particle content of the Standard Model of particle physics (SM). Fermions are divided into three generations with increasing particle masses, where the first generation makes up ordinary matter. Each generation contains an up-type and a down-type quark, a charged lepton, and a neutrino. The gluon, photon, and W/Z bosons are the force-carrying particles of the SM. The Higgs boson is responsible for generating the masses of the elementary particles and couples to all massive particles (except for neutrinos in the current SM). Figure reproduced from Ref. [8, 9].

1.1 The Standard Model

The SM [2–7] is a mathematical framework that combines the electromagnetic, weak, and strong forces into a single, coherent theory. It describes a great number of known subatomic interactions with high precision in terms of a relatively limited number of fundamental particles and their interactions. It accurately predicts the cross sections of many particle physics processes across many orders of magnitude, as shown in Figure 1.2.

The SM is made up of 12 matter fermion particles, their anti-particles, and the four force-mediating vector bosons, all of which are depicted in figure 1.1. Leptons and quarks are fermions that can be divided into three generations according to increasing mass (assuming normal hierarchy in neutrino masses). The electron (e), muon (μ), and tau (τ) are charged leptons with electric charge $-e$. For each generation of leptons, there is an electrically neutral lepton known as a neutrino (ν_e, ν_μ, and ν_τ).

The six quarks in the SM are divided into three generations of pairs. Up-type quarks - with electric charges of $+2/3e$ - are u, c and t, whereas down-type quarks - with electric charges of $-1/3e$ - are d, s and b.

The electromagnetic force is mediated by the electrically neutral, massless photon (γ).

The $W^{\pm}$ and Z^0 bosons (referred to as simply W and Z in this thesis) serve as the mediators of the weak force. They are massive, with $m_W = 80.379 \pm 0.012 GeV$ and $m_Z = 91.1876 \pm 0.0021 GeV$, respectively [10].

The strong force charge - often referred to as colour - has three possible values called red (r), green (g) and blue (b). The only fermions that carry it are the quarks. Quantum chromodynamics (QCD) describes the interactions of such charged particles carrying colour. Gluons are the mediators of the strong force; eight massless bosons coupling to the colour charge. Since they carry colour charge, they may interact with each other.

Originally, despite all observations, particles in the SM were mathematically massless. A theory allowing for a mechanism to generate the masses of the elementary particles in the SM through the coupling of massive SM particles to the Higgs field was proposed in 1964 by Higgs, Brout, and Englert [11, 12]. An important prediction of this theory is the existence of a scalar Higgs boson which was experimentally confirmed in 2012 with its discovery by the ATLAS and CMS experiments [13, 14]. The Higgs boson is the only fundamental scalar particle in the SM and its coupling to other particles (excluding the neutrinos in the current SM) is proportional to their mass. Particles that gain mass through this mechanism are called Dirac fermions (having an odd half-integer spin) and one of their characteristics is that they are distinct from their antiparticles. This topic is discussed further in section 1.3.

1.2 Selected issues within the SM

The SM is a remarkable scientific success, providing a coherent framework for understanding and predicting most physical phenomena in the Universe with high precision. Nevertheless, it remains incomplete, and there are hints towards more fundamental theories. This Section is concerned with two such issues: the fact that the weak force is parity violating and the non-existence of neutrino mass within the theory.

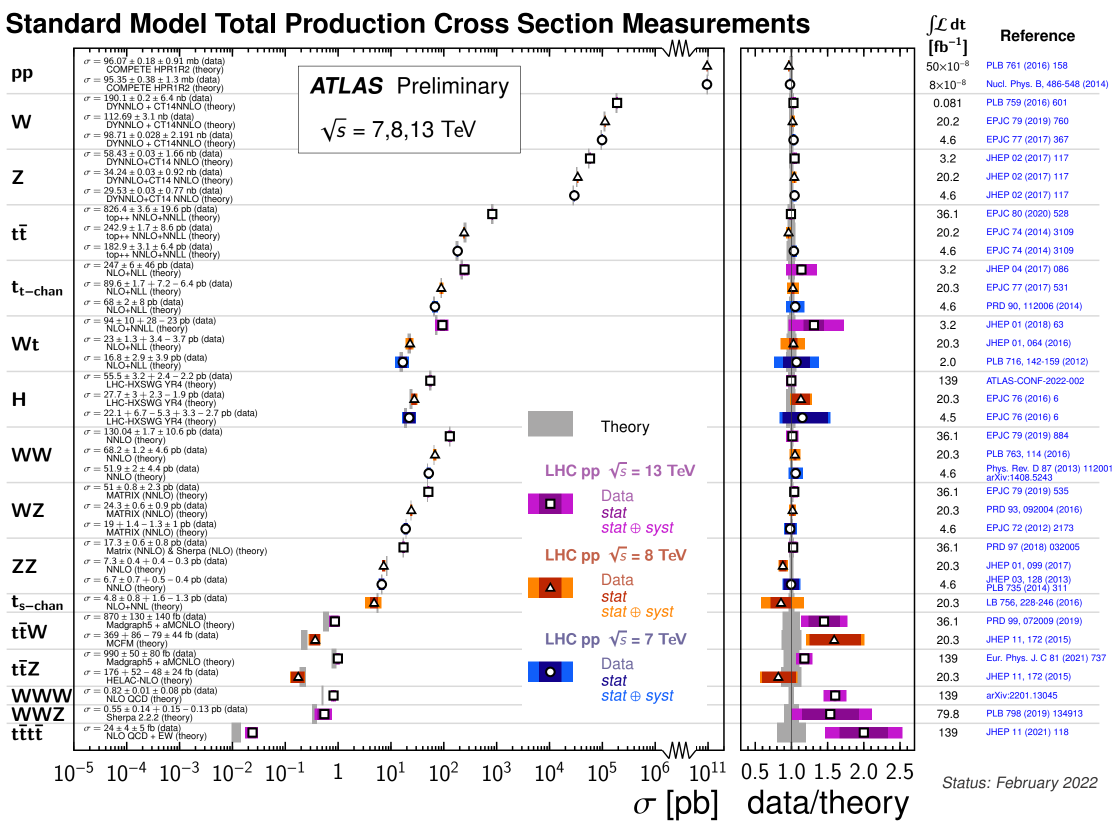

Figure 1.2: Summary of several Standard Model total production cross-section measurements, corrected for branching fractions, compared to the corresponding theoretical expectations and ratio with respect to theory. The associated references are included in a table on the right.

1.2.1 Relevant quantities

At this point, it would be useful to cover the concepts of parity, helicity, and chirality.

Parity describes a reflection through the origin of a particle's spatial coordinates, whereas parity transformation changes the sign of those coordinates. For a given system or variable, parity is defined as either even (+1) or odd (−1), conditional on whether it changes sign after parity transformation. As an example, the momentum of a particle (a vector quantity) has odd parity, since it changes under reflection.

The parity of a particle is the parity of its quantum mechanical state or wavefunction. According to Noether's theorem [15], if a system is invariant (behaves the same way) under a parity transformation, then parity is conserved within that system. Generalising that, if the universe behaves the same way when reflected, then parity is a conserved quantity. A force is parity-violating if it affects a system differently when the system is reflected in space.

Helicity is defined as the projection of a particle's spin onto its momentum. Momentum, as a vector, is affected by the parity operator, while spin, as a pseudovector, is not. As a result, the helicity of a particle is affected by the parity operator (has odd parity). A particle is right-handed if its momentum and spin are aligned, and left-handed if they are anti-aligned.

When a particle changes from having a right-handed to a left-handed helicity, its direction of motion also reverses. Therefore, for a particle to undergo a change in helicity, it must have a non-zero mass and be traveling slower than the speed of light. This is because particles with zero mass must always travel at the speed of light, and changing their helicity would require changing their direction of motion, which is not possible at the speed of light.

Chirality is a frame-independent intrinsic property of a particle, unlike helicity, and relates to the direction that a particle's wavefunction shifts when the particle is rotated. When a spin $1/2$ particle is rotated through 2π, the quantum mechanical state of the particle gains a factor of a minus sign. The chirality of such a particle defines the manner in which this minus sign is obtained in the complex plane: either by passing through i or $-i$. In the massless particle limit, helicity is equivalent to chirality.

In the rest of this thesis, right-handed and left-handed will be used to refer to chirality states, unless otherwise stated.

1.2.2 Parity violation in weak interactions

During the 1950s two seemingly different particles τ^+ and θ^+ were discovered. Even though they each had the same mass and lifetime, they decayed, via the weak force, to systems with different intrinsic parity states. This raised the suspicion that they could be the same particle and that parity might not be conserved by the weak force.

Lee and Yang [16] proposed experiments to further test the nature of the weak force since it had not been experimentally demonstrated that it conserved parity. Two decays could be chosen, one of which proceeded via the weak force and the other not. The first experimental proof of parity violation in weak interactions came soon after, when an asymmetry was measured in the direction of emission of electrons from the decay of Cobalt-60 atoms [17] and in the angular distribution of electrons from muon decays originating from pions decaying in a cyclotron [18]. It was confirmed that the τ^+ and θ^+ particles were one and the same particle, now referred to as the K^+. The decay of K^+ to two pions is parity-violating, since the K^+ has an intrinsic parity of -1 [19].

Within the SM, only particles with a left-handed component experience the weak force, since this is the experimental observation but there is no explanation as to why the weak force is parity-violating. Since parity is conserved in strong and electromagnetic interactions, the weak force is the notable exception in the SM.

Parity-violating processes are indeed counter-intuitive, but perhaps that is because a different operator is more appropriate to describe what we consider parity symmetry in everyday life: the combination of Charge (C) and Parity (P) symmetries. Building on top of that, it is believed that the combination of three symmetries Charge-Parity-Time (CPT symmetry) is a fundamental symmetry of nature. All three of Charge (C), Parity (P), and Time-reversal (T) symmetries have been experimentally observed to not be conserved by the weak force (CP combination as well); it is maybe possible, though, that their combination is conserved.

1.2.3 Neutrino masses

In the SM description neutrinos are massless, as, when it was developed, no evidence for neutrino mass had yet been found. As a result, no terms that would allow massive neutrinos were included in the Lagrangian.

Between the years 1957-1967 Pontecorvo, Maki, Nakagawa and Sakata formulated and expanded on the idea that neutrinos may be massive and oscillate between flavours [20–24].

What we refer to as a neutrino is a state that is generated as a result of a weak interaction. It is a flavour eigenstate: a neutrino is always produced with, or absorbed to give, a charged lepton of electron, muon, or tau flavour (ν_e, ν_μ, ν_τ). The neutrino produced alongside the charged electron is defined as an electron neutrino, and so on. Nonetheless, it is experimentally confirmed that the flavour eigenstates (states with a specific flavour) and the mass eigenstates (states with a definite mass) are not identical.

Consider the mass eigenstates ν_1, ν_2 and ν_3 that are distinct yet near in mass. Every time an electron is generated in a weak interaction, one of these mass eigenstates is formed (ensuring the energy and momentum are conserved at the weak interaction vertex). Assuming that they are produced with varying probabilities (for example, 10% of the time a ν_1 is created), if we could determine the mass of each eigenstate, we could track each mass state as it propagates. But experimental resolution is impossible because the neutrino masses are too tiny. We are aware that we have generated one of them, but we are unable to determine which one. As a result, what we create at the vertices of the weak interaction is a coherent superposition of the ν_i mass states. We refer to this coherent superposition as the electron neutrino:

$$|\nu_e >= U_{e1}|\nu_1 > +U_{e2}|\nu_2 > +U_{e3}|\nu_3 > \tag{1.1}$$

where U_{e1}, U_{e2}, U_{e3} are the coefficients of the coherent superposition of the electron neutrino with the mass eigenstates ν_1, ν_2, and ν_3, respectively.

If this is the case, the following things may occur: Let's say someone creates a neutrino at a source. This neutrino will have a distinct flavour, yet it will be created as a linear combination of states with distinct masses. The states of defined mass will propagate from the source to the detector. If the states have different masses, then the phase between them will vary as they move away from the source. The mass states at the detector will have different relative phases than the mass states had at the source; as a result, when we attempt to detect the mass states, it's likely that we will encounter a flavour state that wasn't initially there in the beam.

When a neutrino changes flavour, it is not changing its mass, but rather it is changing the specific combination of mass eigenstates that it is in. The total mass of the system remains the same, but the mass is redistributed among the different flavour states.

To put it concisely, we understand neutrino creation via flavour but time evolution via mass eigenstates. Neutrinos are created in flavour states, but their flavour can change over time through a process known as oscillation, which is governed by the neutrino's mass eigenstates.

When it comes to flavour and mass eigenstates, mixing angles are determined by a matrix known as Pontecorvo–Maki–Nakagawa–Sakata (PMNS) [20–24]:

$$\begin{aligned}\begin{pmatrix}\nu_e\\ \nu_\mu\\ \nu_\tau\end{pmatrix} &= \begin{pmatrix}U_{e1} & U_{e2} & U_{e3}\\ U_{\mu1} & U_{\mu2} & U_{\mu3}\\ U_{\tau1} & U_{\tau2} & U_{\tau3}\end{pmatrix}\begin{pmatrix}\nu_1\\ \nu_2\\ \nu_3\end{pmatrix}\\ &= \begin{pmatrix}1 & 0 & 0\\ 0 & c_{23} & s_{23}\\ 0 & -s_{23} & c_{23}\end{pmatrix}\begin{pmatrix}c_{13} & 0 & s_{13}e^{-i\delta_{CP}}\\ 0 & 1 & 0\\ -s_{13}e^{i\delta_{CP}} & 0 & c_{13}\end{pmatrix}\begin{pmatrix}c_{12} & s_{12} & 0\\ -s_{12} & c_{12} & 0\\ 0 & 0 & 1\end{pmatrix}\begin{pmatrix}\nu_1\\ \nu_2\\ \nu_3\end{pmatrix}\end{aligned} \tag{1.2}$$

The matrix is parameterized into three different mixing angles θ_{ij} with $i, j = 1, 2, 3$, in addition to δ_{CP}, a CP violating phase. $c_{ij} = \cos\theta_{ij}$ and $s_{ij} = \sin\theta_{ij}$. $|U_{\ell i}|^2$ is the probability for a neutrino created with flavour ℓ to be detected with mass m_i. A neutrino flavour eigenstate can be expressed as a weighted sum of mass eigenstates:

$$|\nu_\ell\rangle = \sum_i U_{\ell i}\,|\nu_i\rangle$$

Starting in 1969, the Homestake experiment recorded fewer than expected electron neutrinos arriving at Earth from the Sun, compared to solar models predictions at the time [25]. This was the first experimental observation for neutrino oscillations since if they could change flavour en route from the Sun, this would result in an apparent deficit in detected yield. The SNO collaboration [26] in 2001, utilising experiment sensitive to several solar neutrino types, demonstrated a statistically significant deficit, which can be explained with neutrino oscillations.

Super-Kamiokande [27], a large underground detector located in Japan, has also been instrumental in our understanding of neutrinos. The experiment began in 1983 and initially studied solar neutrinos, but it soon became apparent that it could also detect atmospheric neutrinos produced by cosmic rays interacting with the Earth's atmosphere. The experiment observed a deficit in the flux of atmospheric muon neutrinos, which provided evidence for the idea that neutrinos have mass and can change their flavor as they travel through space. Takaaki Kajita, the spokesperson of Super-Kamiokande, was jointly awarded the 2015 Nobel Prize in Physics for his contributions to the discovery of neutrino oscillations. Today, Super-Kamiokande continues to be a major player in the study of neutrinos, providing valuable insights into the properties and behavior of these elusive particles.

As a result of a variety of atmospheric, reactor, and beam neutrino oscillation studies, it has been established that the squared-mass difference between all possible combinations of neutrino masses, as well as the mixing angles in the PMNS matrix, are not equal to zero [28].

Direct measurements of neutrino mass have provided only upper bounds so far. For electron and muon neutrinos, the most stringent upper mass limits come from the KATRIN experiment [29] at 0.8 eV (90% CL) and 1.1 eV (90% CL) respectively. The upper limit on tau neutrino mass is the highest at 18.2 MeV, and comes from the ALEPH Collaboration [30]. There is also an upper limit on the sum of the neutrino masses from cosmology; $\sum m_\nu$ can be as large as 0.9 eV [31].

It is now clear that neutrinos have non-zero masses, however small. There currently exist a variety of models attempting to incorporate this fact as a part of SM in such a way as to preserve the degree of parity violation that is observed at low energies.

1.3 Dirac and Majorana Neutrino masses

A seemingly straightforward question regarding neutrinos remains unanswered: Are matter and anti-matter neutrinos two distinct particles, or is the neutrino its own antiparticle? In other words, are neutrinos Dirac or Majorana particles?

Neutrinos are Dirac particles if the total lepton number (L) is conserved. In this case neutrino ν_i and antineutrino $\bar{\nu}_i$ have different lepton numbers: $L(\nu_i) = -L(\bar{\nu}_i) = 1$. Neutrinos are Majorana particles if there is no conserved quantum number which allows distinguishing neutrino or antineutrino.

1.3.1 Dirac Neutrinos

It is possible to introduce Dirac masses for neutrinos to the SM by introducing right-handed SU(2) singlet neutrino components [32]. As such, neutrinos could then be described using the Dirac equation [33] and their masses generated via the Higgs mechanism, through mixing between the left- and right-handed components.

For Dirac fermions, every right-handed chirality component is matched with a left-handed antiparticle component and vice versa. If particle and antiparticle components are accounted for, these fermions have four degrees of freedom and the total lepton number L is conserved. The standard mass term for the Dirac fermions, via the Yukawa coupling [34], is of the form

$$m\overline{\psi}\psi = m(\overline{\psi}_L\psi_R + \overline{\psi}_R\psi_L) \tag{1.3}$$

where ψ ($\overline{\psi}$) is the particle's (antiparticle's) wavefunction, $\psi_L = P_L\psi$ and $\psi_R = P_R\psi$. P_L and P_R are projection operators that satisfy

$$P_L^2 = P_L \quad \text{and} \quad P_R^2 = P_R \quad (P_LP_R = P_RP_L = 0, P_L + P_R = I)$$

Through this approach, neutrino masses can be introduced to the SM without the need for new physics. Right-handed neutrinos may have eluded discovery because their interactions are many orders of magnitude weaker than ordinary neutrinos. This, together with how small the neutrino masses are, is considered by many theorists as a serious flaw of the theory. There are reasons to believe that a different mechanism is responsible, like Majorana, which is described in the next section.

1.3.2 Majorana Neutrinos

It may be the case that Neutrinos have two degrees of freedom [35–37] (compared to four that Dirac neutrinos would have); either a right-handed particle component and a left-handed antiparticle component, or left-handed particle component and a right-handed antiparticle component. Two-component neutrinos can generate mass via the Majorana mechanism [38]. Majorana particles are their own antiparticles, meaning that they have the property

$$\psi^c = \psi \text{ where } \psi^c = \hat{C}\overline{\psi}^T \text{, and } \hat{C} \text{ is the charge conjugation operator} \tag{1.4}$$

which means that only electrically neutral particles, like neutrinos, can satisfy. The Majorana mechanism allows particles with two components to have mass, with terms of form

$$m\bar{\psi}_L^c\psi_L \text{ or } m\bar{\psi}_R^c\psi_R \tag{1.5}$$

Two-component neutrino Majorana mass terms can be achieved by adding extra Higgs fields. If, however, the need for introducing neutrino masses is considered as a chance to restore parity to the SM as a whole, then the LRSM are another possibility that is perhaps more appealing to consider. Within them, and via the Seesaw Mechanism, neutrino masses are generated. Seesaw Mechanisms describe a situation in which the masses of some as-yet-undiscovered neutrinos are inversely proportional to the masses of the established left-handed neutrinos. As a result, the masses of the known neutrinos can be made to be very light, provided that the masses of the new neutrinos are made to be very heavy.

1.4 Left-Right Symmetric Models (LRSM)

LRSM are a class of models attempting to address the issues discussed in section 1.2, by restoring parity to the SM and introducing a mechanism for the generation of neutrino masses. A key feature is the addition of a right-handed component to the weak force, allowing left- and right-handed fermions to take part in weak interactions. These models are appealing since they are a rather simple SM extension.

The idea of left-right symmetry was first suggested in 1974 by Pati and Salam, as an attempt to unify the quarks and leptons under a set of four colour charges [39] and it was developed into the first LRSM a year later [40–43]. There have been a number of LRSM put forward since then; the key distinctions between them may be found in the gauge structure, the scalar fields, the matter contents, and/or the seesaw mechanism.

The LRSM variants described in this section predict heavy, right-handed W bosons (W_R), while, in the next section, their See-Saw extensions predict heavy, right-handed neutrinos (N_R). The KS process, involving W_R and N_R, is discussed in Section 1.6, and is the focus of the analysis.

LRSM introduce the $SU(2)_R$ gauge group, a right-handed analogue to the left-handed weak gauge group $SU(2)_L$. The weak hypercharge $U(1)_Y$ is being exchanged with $U(1)_{B-L}$, where B is the baryon number and L the lepton number. The electric charge is then extended as:

$$Q = T_3 + \frac{Y}{2} \longrightarrow T_{3_L} + T_{3_R} + \frac{B-L}{2}$$

where $T_{3_L} = T_3$ is the weak isospin under $SU(2)_L$, and T_{3_R} is the weak isospin under

$SU(2)_R$.

Right-handed neutrino components are introduced, forming doublets with the existing right-handed lepton components:

$$\psi_L = \begin{pmatrix} \nu_{\ell_L} \\ \ell_L \end{pmatrix} \quad \psi_R = (\ell_R) \longrightarrow \begin{pmatrix} \nu_{\ell_R} \\ \ell_R \end{pmatrix}$$

where $\ell = e, \mu, \tau$. The right-handed lepton doublet has $T_{3_R} = \pm\frac{1}{2}$ and $T_{3_L} = 0$, whilst the left-handed lepton doublet has $T_{3_R} = 0, T_{3_L} = \pm\frac{1}{2}$. Both doublets have $B - L = -1$.

The gauge fields associated with $SU(2)_L$ and $SU(2)_R$ are $\vec{W}_L$ and $\vec{W}_R$ respectively, where:

$$\vec{W}_{L,R} = \begin{pmatrix} W_1 \\ W_2 \\ W_3 \end{pmatrix}_{L,R}$$

$\vec{W}_L$ is identical to the SM $\vec{W}$ with elements W_1, W_2 and W_3, and B is associated with $U(1)_{B-L}$ in the same way it is for the SM $U(1)_Y$. The gauge coupling constants between the respective gauge fields and lepton fields are g_L for $SU(2)_L$, g_R for $SU(2)_R$, and g' for $U(1)_{B-L}$.

The part of the LRSM Lagrangian that concerns the interaction of the LRSM gauge bosons with fermions is [32, 40]:

$$\begin{aligned}
\mathcal{L}^{\text{LRSM}}_{\text{gauge}} &= g_L \left[\bar{q}_L \gamma_i \frac{\vec{\sigma}}{2} q_L + \bar{\psi}_L \gamma_i \frac{\vec{\sigma}}{2} \psi_L \right] \cdot \vec{W}^i_L \\
&+ g_R \left[\bar{q}_R \gamma_i \frac{\vec{\sigma}}{2} q_R + \bar{\psi}_R \gamma_i \frac{\vec{\sigma}}{2} \psi_R \right] \cdot \vec{W}^i_R \\
&+ g' \left[\frac{1}{6} \bar{q} \gamma_i q - \frac{1}{2} \bar{\psi} \gamma_i \psi \right] B
\end{aligned}$$

where q_L and q_R are the SM left- and right-handed quark doublets, γ_i are the Dirac matrices and σ are the Pauli matrices. In order to ensure the model is parity conserving the Lagrangian is required to be invariant under:

$$\psi_L \longleftrightarrow \psi_R \quad q_L \longleftrightarrow q_R \quad \vec{W}_L \longleftrightarrow \vec{W}_R$$

This requires that the $SU(2)$ coupling constants are set to be equal ($g_R = g_L$).

Spontaneous symmetry breaking then occurs to break the LRSM gauge group down to the

SM pre-spontaneous symmetry breaking group:

$$SU(2)_L \times SU(2)_R \times U(1)_{B-L} \longrightarrow SU(2)_L \times U(1)_Y$$

Following this, the usual SM spontaneous symmetry breaking (SSB) occurs, which ensures that the LRSM looks like the SM at low energy scales:

$$SU(2)_L \times U(1)_Y \longrightarrow U(1)_{EM}$$

Different Higgs multiplets are introduced in different LRSM versions, and will be described in the following sections. The nature of the first SSB stage is dependent on the Higgs multiplets introduced.

It is possible to formulate LRSM which add a right-handed singlet neutrino component to the SM and the neutrino masses are obtained via the Higgs mechanism. This method is not preferred though, since it does not explain the smallness of the known neutrino masses as the coupling constants between the right- and left-handed neutrino components would be arbitrary [32]. That is why modern versions of LRSM including the Seesaw mechanism are preferred.

1.5 Seesaw mechanism

Particle Physics theory research has been trying to understand why neutrino masses are so much smaller than the masses of other fermions of the standard model even before it was proven that they have mass. A bit more than 40 years ago, four independently written papers [44] proposed the Seesaw mechanism; a class of neutrino mass models that could generate both a viable neutrino mass spectrum and mixing pattern in addition to new phenomenology: non-conversation of lepton number and new particles, possibly observable at collider experiments.

It is possible to introduce neutrino mass via the Seesaw Mechanism without embedding it in the LRSM [32, 45], but this would not be explaining the parity-violating nature of the weak force. In this section, two LRSM variants are discussed: the Type-I Seesaw Mechanism [46–49] referred to in this thesis as the Type-I LRSM, and the Inverse Seesaw Mechanism [50, 51], referred to as the Inverse LRSM [52–54].

1.5.1 Type-I Seesaw

In the Type-I LRSM, the SM Higgs doublet is replaced with a bidoublet ϕ and a triplet Δ with forms:

$$\phi = \begin{pmatrix} \phi_1^0 & \phi_1^+ \\ \phi_2^- & \phi_2^0 \end{pmatrix} \quad \Delta_{L,R} = \begin{pmatrix} \frac{1}{\sqrt{2}}\Delta^+ & \Delta^{++} \\ \Delta^0 & -\frac{1}{\sqrt{2}}\Delta^+ \end{pmatrix}_{L,R}$$

This set of Higgs fields is left-right symmetric, as can be seen from the fields' T_{3_R} and T_{3_L} values. ϕ has $T_{3_R} = \pm\frac{1}{2}, T_{3_L} = \pm\frac{1}{2}$ and $B - L = 0.\Delta_R$ has $T_{3_R} = \pm 1$, $T_{3_L} = 0$, whilst Δ_L has $T_{3_R} = 0, T_{3_L} = \pm 1$. Both have $B - L = 2$.

The Higgs fields spontaneously gain Vacuum Expectation Value (VEV)s [49]:

$$\langle\phi\rangle = \begin{pmatrix} \kappa & 0 \\ 0 & \kappa' \end{pmatrix} \quad \langle\Delta_R\rangle = \begin{pmatrix} 0 & 0 \\ v_R & 0 \end{pmatrix}_R \quad \langle\Delta_L\rangle = \begin{pmatrix} 0 & 0 \\ 0 & 0 \end{pmatrix}_L$$

The introduction of a VEV for the neutral Δ_R component $\left(\Delta_R^0\right)$ breaks the LRSM gauge group to $SU(2)_L \times U(1)_Y$. It is important that Δ_L does not have a similarly induced VEV in order to prevent possibly large corrections to the light neutrino mass [55, 56]. The VEVs for ϕ take care of breaking $SU(2)_L \times U(1)_Y$ to $U(1)_{EM}$.

New LRSM gauge bosons $W_R^\pm$(referred to as W_R throughout this thesis) and Z_R are formed post-SSB, along with the familiar SM gauge bosons, from the mixing of the pre-SSB gauge fields [32, 43, 55]. In general, the mass states of the charged bosons are a mixture of the W_L and W_R states, and the κ' controls the degree of mixing. By choosing $\kappa \gg \kappa'$, mixing between W_L and W_R states is suppressed [32, 43] and the W_L and W_R can be treated as the mass states. A similar effect occurs whereby the mass states of the heavy neutral gauge bosons are mixtures of the Z and Z_R states, but as $v_R \to \infty$ this mixing is suppressed and Z and Z_R can be treated as mass states [32]. The set of gauge boson states are therefore, in the limit $v_R \gg \kappa \gg \kappa'$:

$$
\begin{aligned}
W_L^{\pm} &= \frac{1}{\sqrt{2}}\left(W_L^1 \pm W_L^2\right) \\
W_R^{\pm} &= \frac{1}{\sqrt{2}}\left(W_R^1 \pm W_R^2\right) \\
Z &= W_L^3 \cos\theta_W - W_R^3 \sin\theta_W \tan\theta_W - B\tan\theta_W\sqrt{\cos 2\theta_W} \\
Z_R &= W_R^3 \frac{\sqrt{\cos 2\theta_W}}{\cos\theta_W} - B\tan\theta_W \\
\gamma &= \left(W_L^3 + W_R^3\right)\sin\theta_W + B\sqrt{\cos 2\theta_W}
\end{aligned}
$$

where θ_W is the SM Weinberg angle defined by $\sin\theta_W = e/g$, where $g = g_L = g_R$. In the limit $v_R^2 \gg \kappa^2 + \kappa'^2$ [47, 55], the masses of the bosons are given by:

$$
\begin{aligned}
m_{W_L}^2 &\simeq \frac{g^2}{2}\left(\kappa^2 + \kappa'^2\right) \\
m_{W_R}^2 &\simeq \frac{g^2}{2}\left(\kappa^2 + \kappa'^2 + 2v_R^2\right) \\
m_Z^2 &\simeq \frac{1}{\cos^2\theta_W} m_{W_L}^2 \\
m_{Z_R}^2 &\simeq \frac{\cos^2\theta_W}{2\cos 2\theta_W} m_{W_R}^2 \\
m_\gamma &\simeq 0
\end{aligned}
$$

By choosing $v_R \gg \kappa \gg \kappa'$, it is ensured that the LRSM gauge bosons are heavier than the SM gauge bosons.

The part of the Type-I LRSM Lagrangian that concerns the interaction of the LRSM Higgs fields with leptons is [55, 57] (shown for one generation for simplicity):

$$
\begin{aligned}
\mathcal{L}_{\text{mass}}^{\text{LRSM}} &= h_{D_1}\bar{\psi}_L\phi\psi_R + h_{D_2}\bar{\psi}_L\tilde{\phi}\psi_R \\
&\quad + h_M\left(\bar{\psi}_L^c\Delta_L\psi_L + \bar{\psi}_R^c\Delta_R\psi_R\right) + \text{ H.c.}
\end{aligned}
$$

where $\tilde{\phi} = \sigma_2\phi^*\sigma_2$ and '+ H.c.' indicates Hermitian conjugate terms have been omitted. The terms in the Lagrangian preceded by $h_{D_{1,2}}$ are Dirac mass terms, and $h_{D_{1,2}}$ are the coupling strengths. Terms preceded by h_M can be identified as Majorana mass terms, with h_M as the coupling strength. Following the two SSB stages, once the VEVs $\langle\phi\rangle$ and $\langle\Delta_R\rangle$ have been substituted into the Lagrangian, the lepton mass is given by:

$$m_\ell = h_{D_1}\kappa' + h_{D_2}\kappa$$

For the neutrinos, a mass matrix for the ν_L and ν_R is obtained:

$$\begin{array}{c} \\ \nu_L \\ \nu_R \end{array} \begin{array}{c} \begin{array}{cc} \nu_L & \nu_R \end{array} \\ \begin{pmatrix} 0 & m_\ell \\ m_\ell & m_R \end{pmatrix} \end{array}$$

where $m_R = h_M v_R$. This matrix has eigenvalues of:

$$m_{\nu_{L,R}} = \frac{m_R \pm \sqrt{m_R^2 + 4m_\ell^2}}{2}$$

which in the limit $m_R \gg m_\ell$ (from $v_R \gg \kappa, \kappa'$), and expanding via a Taylor series, gives two masses:

$$m_{\nu_L} \simeq \frac{m_\ell^2}{m_R}$$
$$m_{\nu_R} \simeq m_R$$

This is where the name 'Seesaw Mechanism' originates: as m_R increases, m_{ν_R} increases whilst m_{ν_L} decreases. In this way, the Type-I LRSM contains a natural reason for the small masses of the known neutrinos, and the LRSM gauge bosons and right-handed neutrinos could have masses that are within the reach of the LHC, assuming they exist.

As a reminder that ν_R are heavy in the context of this model, N_R will be used to refer to them in the rest of this thesis. Because h_M is a free parameter, the mass hierarchies $m_{W_R} > m_{N_R}$ and $m_{N_R} > m_{W_R}$ are both possible. As the ν_L and N_R resulting from the Type-I Seesaw Mechanism are Majorana particles, lepton number violating processes are predicted to occur involving them.

1.5.2 Inverse Seesaw

The Inverse Seesaw Mechanism, like the Type-I Seesaw Mechanism, provides a way to naturally explain the small masses of the known neutrinos. The Inverse Seesaw Mechanism was originally implemented in the context of superstring theories [50, 51], but can also arise within an LRSM [53, 54, 58].

There are several ways to implement the Inverse Seesaw Mechanism in an LRSM, with different choices of Higgs multiplets. One way is to introduce a pair of Higgs doublets $\chi_{L,R}$, alongside ϕ and $\Delta_{L,R}$:

$$\chi_{L,R} = \begin{pmatrix} \chi^+ \\ \chi^0 \end{pmatrix}_{L,R}$$

χ_R has $T_{3_R} = \pm\frac{1}{2}, T_{3_L} = 0$, whilst χ_L has $T_{3_R} = 0, T_{3_L} = \pm\frac{1}{2}$. Both have $B - L = 1$. A set of singlet fermions S, with $T_{3_{L,R}} = 0$ and $B - L = 0$ are also introduced.

ϕ and Δ_R gain the same VEVs as in the Type-I LRSM, and χ_R gains a VEV:

$$\chi_R = \begin{pmatrix} 0 \\ \lambda_R \end{pmatrix}_R \quad \chi_L = \begin{pmatrix} 0 \\ 0 \end{pmatrix}_L$$

The part of the Lagrangian that concerns the interaction of the Higgs fields with leptons is (shown for one generation for simplicity):

$$\begin{aligned} \mathcal{L}_{\text{mass}}^{\text{LRSM}} &= h_{D_1}\bar{\psi}_L\phi\psi_R + h_{D_2}\bar{\psi}_L\tilde{\phi}\psi_R \\ &+ h_{N_1}\bar{\psi}_L\chi_L S + h_{N_2}\bar{\psi}_R\chi_R S + h_S S^c S \\ &+ h_M\left(\bar{\psi}_L^c\Delta_L\psi_L + \bar{\psi}_R^c\Delta_R\psi_R\right) + \text{ H.c.} \end{aligned}$$

where $h_{N_{1,2}}$ are the couplings between $\phi_{L,R}^-$ and S, and h_S is the S self coupling. Following the substitution of the VEVs $\langle\phi\rangle$, $\langle\Delta_R\rangle$ and $\langle\chi_R\rangle$, the lepton mass is given by:

$$m_\ell = h_{D_1}\kappa' + h_{D_2}\kappa$$

as in the Type-I LRSM. A mass matrix is formed for the ν_L, ν_R and S:

$$\begin{array}{c} \\ \nu_L \\ \nu_R \\ S \end{array}\begin{array}{c} \begin{array}{ccc} \nu_L & \nu_R & S \end{array} \\ \begin{pmatrix} 0 & m_\ell & 0 \\ m_\ell & m_R & m_N \\ 0 & m_N & m_S \end{pmatrix} \end{array}$$

where $m_R = h_M v_R, m_N = h_N \lambda_R$ and $m_S = 2h_S$. From this matrix, two mass eigenstates are formed from ν_R and S :

$$m_{N_{R_{1,2}}} = \frac{m_R \pm \sqrt{m_R^2 + 4m_N^2}}{2}$$

In the limit $m_R \longrightarrow 0$, there are two equal magnitude, opposite sign solutions:

$$\left|m_{N_{R_1}}\right| = \left|m_{N_{R_2}}\right| = m_N.$$

In this situation, a pseudo-Dirac N_R [59] is formed from the combination of the Majorana $N_{R_{1,2}}$. For a pseudo-Dirac N_R formed in this way, as $m_R \longrightarrow 0$, the amount of lepton number violation also tends to zero [58, 60]. The simplest way to ensure $m_R = 0$ is to remove the $\Delta_{L,R}$ entirely. As $m_R \longrightarrow 0$, the light neutrino mass is given by:

$$m_{\nu_L} = \frac{m_S m_\ell^2}{m_N^2}$$

so, like in the Type-I Seesaw Mechanism, m_{ν_L} decreases as m_{N_R} increases. The pseudo-Dirac N_R will be referred to as a Dirac N_R throughout the rest of this thesis.

1.6 The Keung-Senjanović (KS) Process

The KS process [61] is a hypothetical decay based on the LRSM and the Seesaw mechanism that involves the production of right-handed W bosons (W_R) and right-handed neutrinos (N_R). The Feynman diagram for this process can be seen in figure 1.3. Initially, a W_R

decays to a N_R and a charged lepton. Afterwards, assuming that there is no mixing between the W_L and W_R, the N_R decays to a second W_R and another lepton. Finally, only the case where the second W_R decays to two quarks is considered. The final state of the KS process is, therefore, two charged leptons and two jets (lljj).

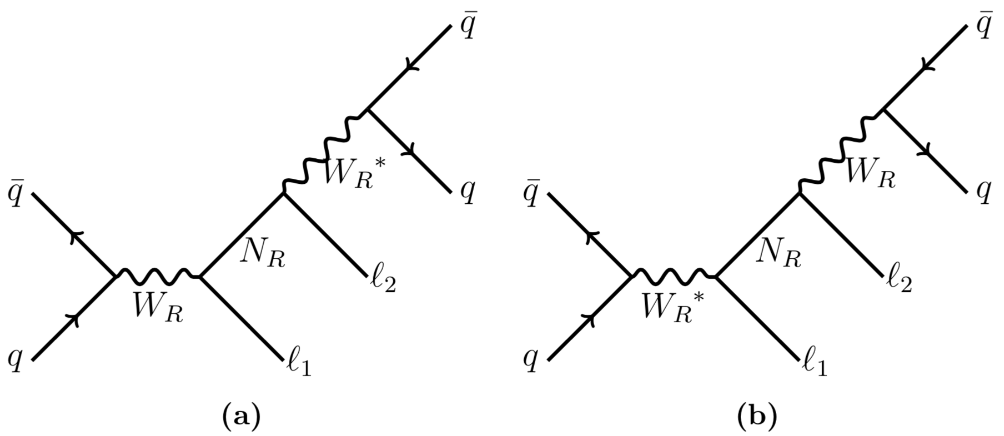

Figure 1.3: The leading Feynman diagram for the KS process, for (a) the $m_{WR} > m_{NR}$ case and (b) the $m_{WR} < m_{NR}$ case. The * next to a particle denotes that it is off-shell. Adapted from [61].

When $m_{W_R} > m_{N_R}$ the second W_R in the decay chain must be produced off-shell; this is known as the nominal hierarchy case and the on-shell W_R mass can be reconstructed from the invariant mass of the $lljj$ system. Alternatively, in the $m_{N_R} > m_{W_R}$ case, the first W_R is off-shell. In this inverse hierarchy case, the W_R mass can be reconstructed from the jj system. This case is heavily suppressed in terms of cross-section. The mass of the N_R can be found from the $lljj$ system in both cases.

Dirac and Majorana N_R can both participate in the KS process, with the same production cross section [58]. The Majorana nature of the N_R can be inferred from the ratio of events containing opposite-sign (OS) or same-sign (SS) charged leptons. A Majorana N_R would permit lepton number violating processes in the Type-I LRSM version discussed earlier. The produced leptons in the final state would then be charged with the same sign 50% of the time and the opposite sign 50% of the time. Alternatively, in the Inverse LRSM version, N_R are Dirac particles, and the final state leptons will have opposite-sign charges 100% of the time.

This thesis does not explore any potential mixing of N_e, N_μ, and N_τ, hence only final states with the same flavour leptons are investigated. Considered are final states with two electrons (eejj) or two muons ($\mu\mu jj$), also termed as the electron and muon channels, respectively.

1.6.1 Exclusion limits for the KS process

The KS process in the $eejj$ and $\mu\mu jj$ final state has been studied by both ATLAS and CMS collaborations using $\sqrt{s}$ = 7 TeV [62, 63], $\sqrt{s}$ = 8 TeV [64, 65] and $\sqrt{s}$ = 13 TeV [61, 66–68] collision data.

The current most stringent exclusion limits on LRSM W_R and Majorana N_R masses are derived by the CMS experiment [68] at $\sqrt{s}$ = 13 TeV. When all four final state particles (2 leptons and two jets) can be reconstructed, called the resolved regime, the W_R mass upper limits are 4.7 TeV in the electron channel and 5.0 TeV in the muon channel. When W_R mass » N_R mass and one or both of the leptons are reconstructed together with the jet, referred to as the boosted regime, this limit extends to 4.8 (electron) and 5.4 (muon) TeV.

Other bounds on heavy W bosons and N masses exist from double beta decay, dijet [69, 70], $t\bar{b}$ resonance [71, 72] searches. Table 1.6 presents the limits from these searches.

Analysis	Luminosity $\left(\text{fb}^{-1}\right)$	Observed limit (TeV)
ATLAS dijet [69]	139	3.80
CMS dijet [70]	137	3.60
ATLAS tb [71]	36.1	3.45
CMS tb [72]	137	3.50

(1.6)

Chapter 2

The LHC and the ATLAS Experiment

> “*If you build it, they will come*”
>
> Ray Kinsella, Field of Dreams

CERN (Conseil Européen pour la Recherche Nucléaire or European Organisation for Nuclear Research) was founded in 1954 near Geneva, Switzerland to support collaboration between countries involved in high-energy particle physics research. The LEP (Large Electron-Positron) collider, constructed at CERN, was the largest particle accelerator in the world until 2000 when the construction of the Large Hadron Collider (LHC) [73] (figure 2.1) began in the same tunnels.

2.1 The Large Hadron Collider (LHC)

The LHC,with a circumference of 26.7 km, is the largest accelerator and collider ever built, designed for proton-proton (*pp*) collisions and heavy ion collisions such as lead–lead (*Pb-Pb*). It was constructed to study the electroweak symmetry-breaking mechanism and the (until then) elusive Higgs boson. Following the discovery of such a Higgs-like particle in 2012 [13, 14]), the LHC switched focus to other Beyond the Standard Model (BSM) models. To search for those rare exotic physics processes, the LHC requires large centre-of-mass energies and instantaneous luminosity.

Protons are being pre-accelerated before entering the LHC in what is called the injector chain which is a series of smaller accelerators (fig 2.1). The process begins at the LINAC2

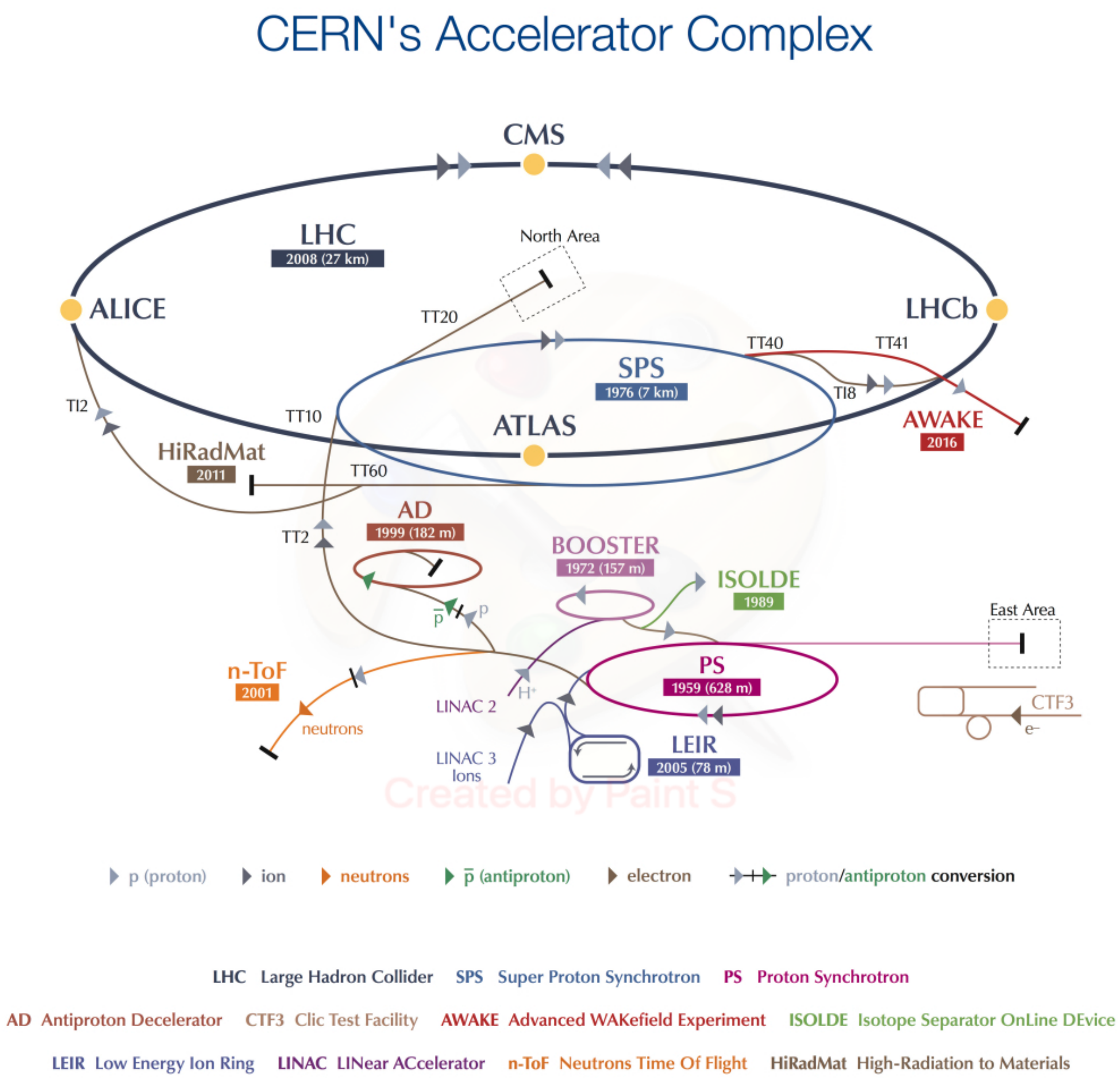

Figure 2.1: Layout overview of the CERN accelerator complex. The LINAC2 accelerates protons from rest, they are then injected into increasingly larger synchrotrons: the Proton Synchrotron Booster (PSB, or "Booster"), the Proton Synchrotron (PS), and the Super Proton Synchrotron (SPS). As the final step, the protons are injected into the LHC and are accelerated up to a design beam energy of 6.5 TeV (Run 2). Figure adapted from Ref. [74].

linear accelerator [75] where hydrogen gas over a distance of 33 m is accelerated to energies of around 50 MeV through radio-frequency (RF) accelerator tanks [75], resulting in the hydrogen atoms losing their electrons.

Subsequently, the proton beam is going through a sequence of three synchrotrons in which it is accelerated using RF cavities along the beam pipe and directed using synchronously increasing dipole magnetic fields. Firstly, the Proton Synchrotron Booster (PSB) accelerates the beams to an energy of 1.4 GeV and has a circumference of 157 m, followed by the Proton Synchrotron (PS) that increases the energy to 25 GeV with a circumference of 628 m, and finally, the Super Proton Synchrotron (SPS) accelerates the beam to 450 GeV energies through its 7 km ring before they are being injected to the LHC. The LHC can then accelerate each bunch up to 7 TeV, resulting in a proton-proton centre-of-mass energy of $\sqrt{s} = 14$ TeV.

In the LHC, through separate pipes, two proton beams circulate in opposite directions. Those beams intersect in four interaction points, each being one of the large LHC experiments: ATLAS [76] and CMS [77] are general-purpose experiments designed for high-energy proton-proton collisions, ALICE experiment [78] is designed for heavy-ion collisions, and LHCb [79] is a single-arm, forward experiment designed for flavour physics.

At the interaction points, the beams can be made to cross, therefore letting the protons in each of the counter-rotating bunches to collide. The expected rate dN/dt of collision events for a process with cross-section σ is given by

$$\frac{dN}{dt} = \mathcal{L}\sigma \longrightarrow N = \int \mathcal{L}\sigma dt,$$

where $\mathcal{L}$ is the instantaneous luminosity. The total number of expected collision events (N) for any given process is equivalent to the time-integrated luminosity L which is equal to $\int \mathcal{L} dt$.

The target instantaneous luminosity of the LHC is $L = 10^{34}\,\text{cm}^{-2}\,\text{s}^{-1}$ [73]. The LHC has been operating with up to twice its design luminosity during Run2.

Each LHC bunch contains $O(10^{11})$ protons, and the LHC is designed to store 2808 proton bunches in each beam, which results in a nominal bunch spacing of 25 ns [73]. This leads to a collision rate of around 40 MHz at each interaction point (IP).

As a result of the high luminosity, the LHC has produced a peak number of more than 60 interactions per bunch-crossing - and the average pile-up multiplicities during Run 2 was 34 [80] - making for highly complex final states.

2.2 The ATLAS Experiment

The ATLAS experiment, figure 2.2, uses a cylindrical design with approximate rotational symmetry in the azimuthal plane and forward-backwards symmetry along the beam axis. The nominal IP of the LHC beams is positioned at the centre of the detector, and serves as the origin of the coordinate system.

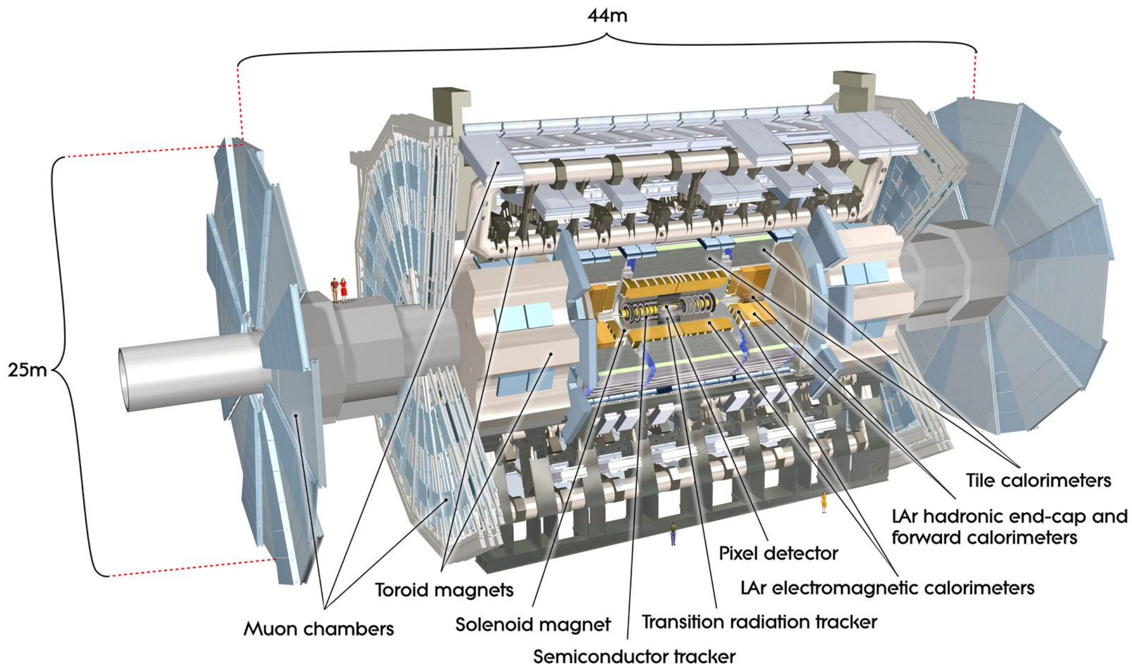

Figure 2.2: Computer-generated image of the ATLAS detector, highlighting each sub-detector [82].

The ATLAS detector design is to be almost hermetic in the azimuthal plane, and to provide the largest coverage in pseudo-rapidity. The goal is to reduce potential energy leakage in the transverse plane and to guarantee a large geometric acceptance of final state particles. It is impossible to design a collider experiment with perfect 4π solid angle coverage because of the beam-pipe, which at the LHC has an inner radius of 25 mm [81].

ATLAS is one of the two general-purpose detectors at the LHC that discovered the Higgs boson. It is able to reconstruct a variety of particles; for example hadrons, electrons, muons, taus, and photons. All those particles were used to study the different Higgs boson decay modes [83].

Pseudorapidity (η) is a quantity used in particle physics to describe the angle of a particle relative to the beam axis. It is defined as $\eta = -\ln[\tan(\frac{\theta}{2})]$. This quantity is used in ATLAS and other detectors because it is invariant under boosts along the beam axis and provides information about the detector geometry and colliding particles. Pseudorapidity is often preferred over the polar angle θ because it is a more natural variable to use in the context of high-energy physics experiments. This is because the distribution of particles produced tends to be more uniform in pseudorapidity than in the polar angle.

The detector is designed as a group of nested sub-detectors at increasing radii from the IP, each aiming to measure different properties of the particles created in collision events.

These sub-detectors are:

Inner detector (ID) that calculates the location of space points along the trajectory of electrically charged particles, without affecting the trajectory itself. The ID consists of the Pixel detector, the semi-conductor tracker (SCT), and the transition radiation tracker (TRT).

Calorimeters that calculate the direction and total energy of most electromagnetically and hadronically interacting particles via full absorption. The calorimeter system comprises the electromagnetic calorimeter (ECAL) and hadronic calorimeter (HCAL); and

Muon spectrometer (MS)) that calculates the direction and momentum of muons passing through the calorimeters and inner detector, as well as providing specialised trigger capabilities. The MS consists of the monitored drift tube chambers (MDTs), cathode strip chambers (CSCs), resistive-plate chambers (RPCs), and thin-gap chambers (TGCs).

The ATLAS sub-detectors are shown in Figure 2.3. For larger coverage and better measurements in the forward regions, namely at large $|\eta|$, the detectors are subdivided into the barrel and end-cap components: the central barrel component has active elements parallel to the beam-pipe, while the forward end-cap components are placed perpendicular to the beam-pipe, at each end of the barrel.

The 40 MHz nominal *pp* collision rate in the ATLAS experiment is much larger than the maximum rate at which the experiment is able to record collision events for reconstruction and analysis, which is roughly 1 kHz [76]. Most of the collision events are not of key interest, since decays involving e.g. Higgs boson production and hypothesised BSM processes, are extremely rare. As a result, the ATLAS trigger system (detailed in section 3) performs a quick online selection to achieve this massive reduction in event rate while retaining a high acceptance of interesting physics processes. During Run 2, the ATLAS experiment recorded data with detector up-time and so-called "good data quality" efficiencies of $\geq 95\%$. This made it possible for the ATLAS experiment to efficiently utilise the LHC luminosity, recording 139 fb^{-1} of data as can be seen in Figure 2.3.

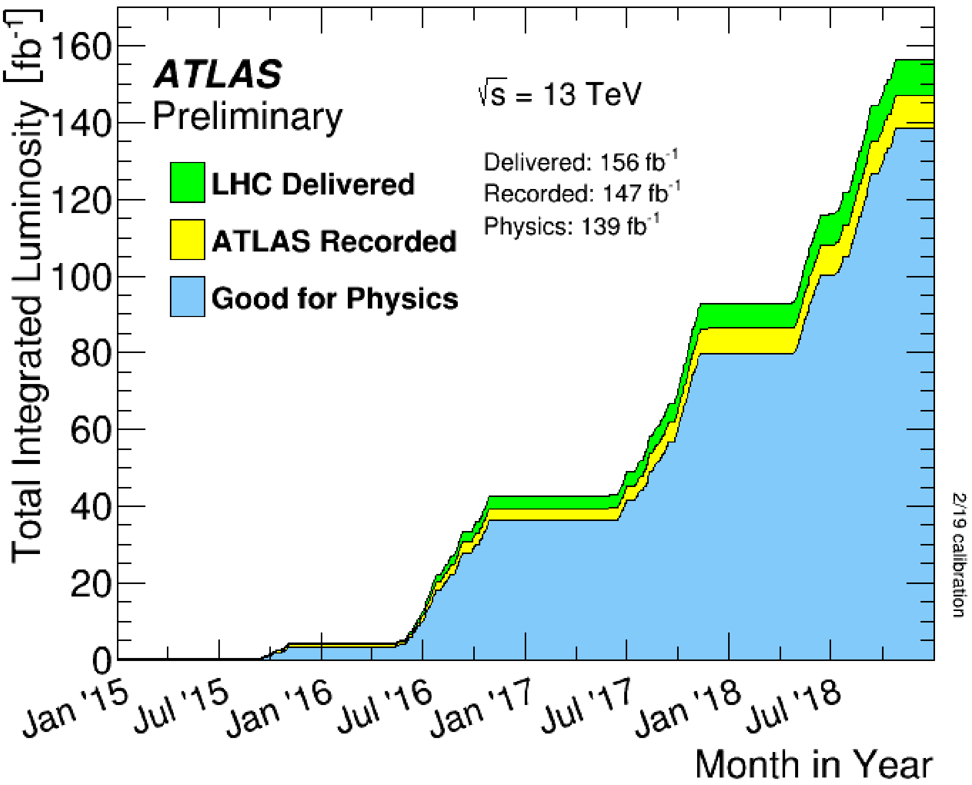

Figure 2.3: Cumulative integrated luminosity and data quality over the duration of the LHC Run 2. Figure from Ref. [80].

2.3 Magnet system

For charge identification and accurate momentum calculation in the ID and MS, the trajectory of charged particles is curved through the Lorentz force. This is achieved by a combination of a solenoidal magnet and a three-part toroidal magnet, as can be seen in Figure 2.2,

The central solenoidal magnet encloses the ID with a radius of 1.2 m and an axial length of 5.3 m [76, 84]. It generates a 2 T axial magnetic field, which forces the electrically charged particles to bend in the transverse plane. The solenoid is a thin superconducting magnet with a thickness of 4.5 cm (approx. 0.66 radiation lengths, X_0), designed to decrease the amount of material upstream of the calorimeters as much as possible.

To contribute additional bending of muon trajectories for the MS [76] a group of one barrel and two end-cap toroidal magnet components are used, downstream of the calorimeters. A closed, circular 0.5-1 T magnetic field is generated in the transverse plane by those magnets, almost perpendicular to the muon trajectories. These air-core toroid magnets range from radius 4.7 m to 10 m with an axial length of 25.3 m.

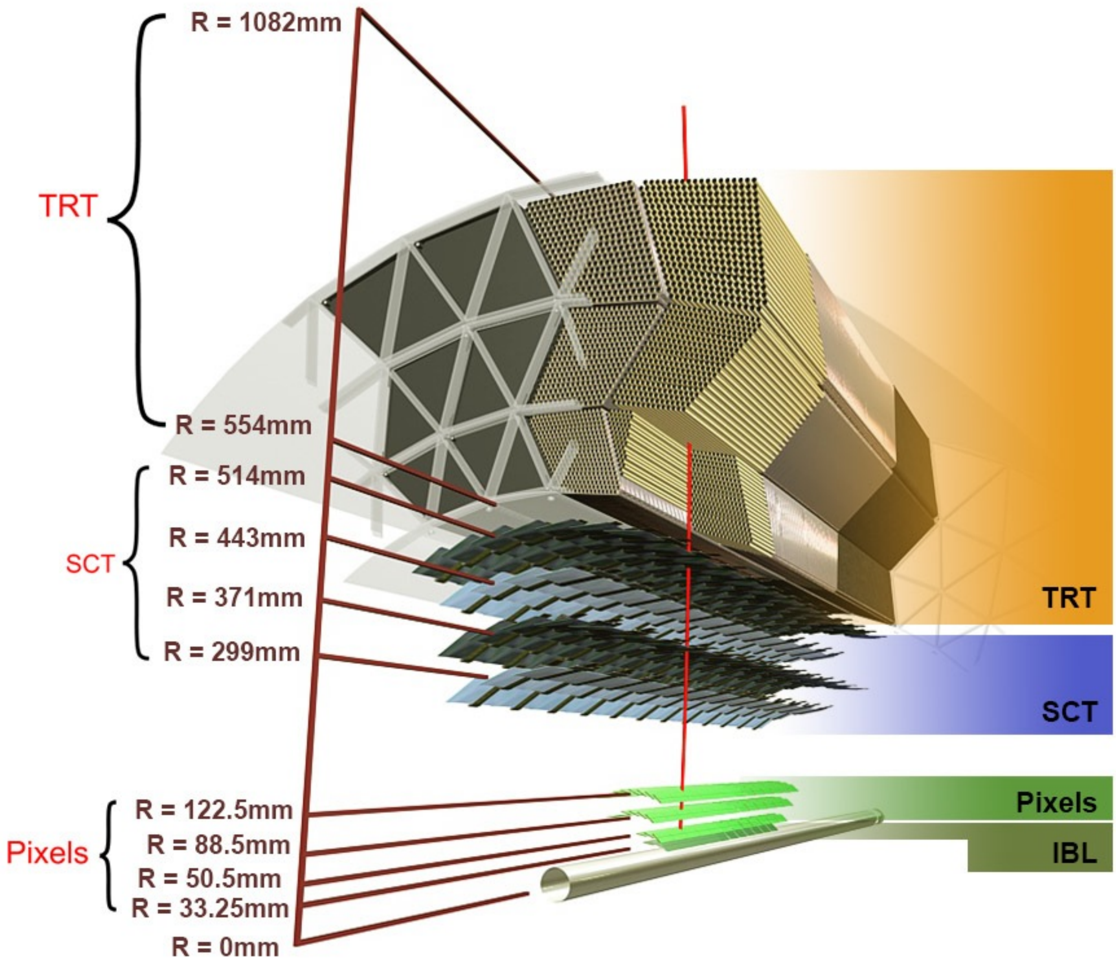

Figure 2.4: Design layout image of the ATLAS ID, highlighting each sub-detector. The red line corresponds to the trajectory of a charged particle with p_T = 10 GeV [85].

The design yields a powerful magnetic field in a large volume with minimal material, contributing to a system of high-precision measurements of muon momenta in the MS.

2.4 Inner detector (ID)

The ATLAS ID, shown in Figure 2.4, is designed to track electrically charged particles by taking high-resolution, non-destructive measurements of their trajectories, momenta, and charge.

When a charged particle travels through a segment, it will result in a detectable electrical signal. These signals are called hits and are used to reconstruct the tracks of the particles. For promptly produced charged particles, the track starts at the collision point and extends, at increasing radii, through the layers of the ID.

The ID is enclosed in the magnetic field of the central solenoid. As a result, the trajectory of a charged particle will be bent in the transverse plane with a curvature radius equal to $r = \frac{p_T}{qB}$ [10], where p_T is the transverse momentum of the particle, q the electric charge in elementary charge units, and B the magnetic field strength. At least three hits are required to measure the bending radius of a track which is then used to calculate the momentum and charge of the particle. One of the most important uses of charged particle tracking is to pinpoint the so-called primary vertex (PV): the hard collision, among many others, that the final state particles of interest emerge from. The ID is able to track particles with $|\eta| < 2.5$ and p_T as low as 400 MeV [85].

2.4.1 Pixel detector

The Pixel detector [86] and the Semiconductor Tracking detector (SCT) are the closest sub-detectors to the IP. Thus, they are required to deliver fine-grained measurements of the large particle flow to aid the reconstruction of track and PV with high resolution; ergo they are constructed as silicon detectors, to deliver position resolution at the scale of tens of microns. The detector sensors of the semiconductor are functioning in reverse-bias mode, resulting in a depletion region, devoid of free electrons, in the centre of the sensor [10]. Charged particles, when passing through the depletion region, will excite a large number of electron-hole pairs which then drift to opposite electrodes under the reverse bias electric field. As a consequence, a signal current is generated that is read out as a hit. In this manner, semiconductor detectors behave as solid-state ionisation chambers.

The ATLAS Pixel detector was designed originally with three layers in the barrel region, with a radius ranging from 50.5 mm to 122.5 mm, and three end-cap disks able to cover $|\eta| < 2.5$ [76]. Following that, the insertable B-layer (IBL) was installed in 2014 to increase the resolution closest to the IP; it has a radius of 33 mm from the beam axis [81]. To reduce energy loss in the ID, Pixels are roughly 250 μm thick. In the barrel region, the nominal pitch is $50 \times 400\,\mu\text{m}^2$ in $\phi \times z$, with a similar Pixel size in $\phi \times R$ in each of the end-caps. This results in an intrinsic accuracy of $10 \times 115\,\mu\text{m}^2$ in $(R — \phi) \times z$ and $(\phi — z) \times R$, respectively.

As a result of the axial magnetic field produced by the central solenoid, the hits in the transverse plane are more useful for the momentum calculation than along the longitudinal axis. This is the reason for the 1 : 8 choice in sensor dimensions.

2.4.2 Semi-conductor tracker

The SCT, positioned just outside the ATLAS Pixel detector, delivers accurate tracking via the use of semiconductors [76]. Four cylindrical layers, each with an axial length of 150 cm, positioned between radii of 29.9 cm and 55.4 cm make up the barrel SCT. The SCT end-cap consists of 9 disks between $|z|$ = 8.53 m and 27.2 m, on both sides of the barrel and is able to cover values of $|\eta| < 2.5$. The SCT has a greater active area than the Pixel detector, therefore it is constructed using a cost-effective strip design. The sensors have silicon strips with 80 μm pitch, a thickness of approx. 285 μm, and a strip length of approx. 6 cm that are grouped together in a back-to-back fashion to form the modules. Modules are rotated at a stereo angle of 40 mrad from each other. The axial strips are parallel to the beam axis in the barrel and perpendicular in the end-caps. The off-axis strips are at a stereo angle with the detector layers.

Charged particles passing through an SCT module will usually hit two overlapping strips, providing accurate location measurement even in the longitudinal direction. Therefore, SCT modules have an intrinsic accuracy of $17 \times 580\,\mu\text{m}^2$ in $(R — \phi) \times z$ in the barrel and $(\phi — z) \times R$ in the end-caps. The resolution in the bending direction of the central solenoid is prioritised for the SCT, as is the case with the Pixel detector.

Hits in the Pixel detector and SCT modules are being described as "space points" resulting from their exceptional spatial resolution and high-granularity basis for tracking and vertex-finding.

2.4.3 Transition radiation tracker

The TRT [76, 87] comprises from drift tubes, known as straws, with a diameter of 4 mm, and consist of a barrel and two end-cap components. In the barrel region, the straws are 144 cm long and are parallel to the beam-axis out to $|z|$ =712 mm. The end-cap straws have a length of 37 cm and are placed in wheels perpendicular to the beam, between radii 64.4 cm $< r <$ 100.4 cm, granting a combined TRT acceptance of $|\eta| < 2.0$. TRT, as a drift tube detector, places 2D position constraints in the plane perpendicular to the straws. This is different to the silicon detectors that deliver 3D space points.

Straws have a 31 μm diameter gold-plated tungsten anode wire at their core, which extends up to the ends of the straw and is kept grounded. The thickness of the drift tube walls is 70 μm and they can function at ~1530 V potential. The initial composition of the straws was a gas mixture of 70% Xe, 27% CO_2, and 3% O_2. Due to leakages, a gas mixture primarily made up of less expensive argon is used in parts of the subdetector without a big impact on performance [88].

Electron-ion pairs are created when the gas is ionised by charged particles passing through the drift tube. The negatively charged electrons are accelerated by the electrical field and move towards the anode wire, starting an ionisation cascade. Similarly, the positively charged ions move towards the cathode, though more slowly. The electrical pulse from the ionisation particles is then read out as signal.

Drift-time is the difference between the 40 MHz LHC clock and the leading edge of the signal pulse; it can be used to calculate the impact parameter of the original charged particle's trajectory from the anode wire. The drift-time precision in the plane transverse to the straw is 130 µm. Charged particles that have $p_T > 500$ MeV and $|\eta| < 2.0$ travel over 36 straws, while in the barrel–end-cap transition region at $0.8 < |\eta| < 1.0$, at least 22 straws [76].

The TRT has a unique feature for particle identification, using polypropylene fibers embedded in the barrel straws and end-cap foils. When high-energy charged particles, particularly electrons with large Lorentz factors, pass through the fibers, they emit transition radiation photons. The TRT can distinguish electrons from charged pions by setting separate low and high thresholds for hits, enabling efficient electron identification in the presence of background particles.

2.4.4 Performance

The installation of IBL was the primary Phase-0 improvement made to the ATLAS ID with respect to the original design (i.e., before Run 2) [81]. It was installed to improve parameter resolution, especially for low-p_T tracks, decrease the rate of fake tracks at high luminosities, minimise deterioration over time of the original ATLAS Pixel detector, such as due to high radiation doses, and mitigate fake track rates.

Aside from this, the Run 2 performance of the ATLAS ID was consistent with its design objectives [76]. For instance, a 2015 performance study with low-pile-up Run 2 data showed that the measured resolution was in agreement with the projected resolution of the transverse impact parameter d_0 for central tracks, which was expected to be $\sigma(d_0) \approx 20\mu$m at $p_T = 10$ GeV [85]. Because the resolution of the track hit measurements in the Pixel detector, for example, is determined by the resolution of the transverse impact parameter, the ATLAS ID has had a stable performance. Since the detector elements themselves

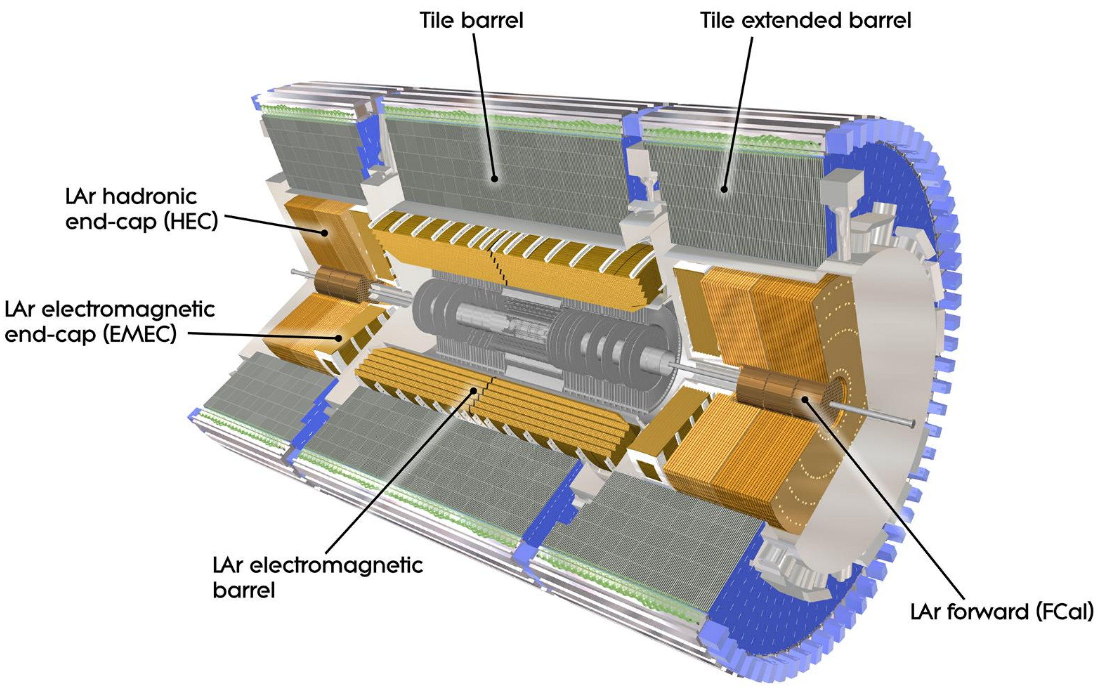

Figure 2.5: Design layout of the ATLAS calorimeter system, comprised of the electromagnetic calorimeter (ECAL) and hadronic calorimeter (HCAL) [89]

determine this spatial resolution, subsequent offline reconstruction and calibration cannot improve it.

2.5 Calorimetry

Particles enter the ATLAS calorimeter system after transversing the ID, as shown in Figure 2.5. Contrary to the ID, which accomplishes exact spatial measurements with hardly any interference on the energy and trajectory of electrically charged particles, calorimeters are designed to measure the total energy of electromagnetically and hadronically interacting particles. This is accomplished by measuring the position of the particles in η — ϕ space via full absorption, and therefore destruction of the particles.

Electromagnetically interacting particles (such as electrons and photons) generally start a cascade when they come into contact with a dense material: for example, an incident electron emits a Bremsstrahlung photon, which further decays to a pair of e^+e^-, and so on. As a result, an electromagnetic shower is produced. It is characterised by the radiation length X_0, over which the high-energy electron ($E_e \gg 1$ GeV) will have lost all but $1/e$ of its initial energy due to bremsstrahlung radiation [90]. The mean free path for high-energy photons to decay into an e^+e^- pair, which is determined by $9X_0/7$, is correlated to the radiation length. Since the radiation length depends on the material, passive materials with short radiation lengths can be used in compact calorimeters to contain electromagnetic showers.

Hadronic showers are initiated when energetic hadrons, such as protons or neutrons, interact with passive material. These are typically characterised by the nuclear interaction length, or λ_{int}, which refers to the average distance a high-energy hadron will travel before interacting with a nucleus [90]. For a given material, the nuclear interaction length is typically much longer than the radiation length. Hadronic showers consequently tend to be significantly larger in the longitudinal and lateral dimensions, requiring the utilisation of larger calorimeters for efficient containment. The longitudinal position of the position where the shower activity is at its peak scales with the logarithm of the energy of the incident particles for both electromagnetic and hadronic showers [90]. This suggests that particles with energy ranging several orders of magnitude, from O(GeV) to O(TeV), can be measured using the same calorimeter device.

To distinguish between QED and QCD processes, specialized calorimeter systems are constructed: ECALs are generally installed closest to the beam and are designed to contain nearly all electromagnetic showers. HCALs are constructed to absorb hadronic showers and are commonly placed outside of the ECAL because of the large values of λ_{int} in most absorber materials. However, it is not always straightforward to distinguish between hadronic and electromagnetic showers, and consequently, between ECALs and HCALs: Hadronic showers could be initiated in the ECAL and contain electromagnetic components, such as photons produced by neutral pion decays.

The various components of the ATLAS calorimeter system give coverage for $|\eta|$ <4.9. Similarly, the depth of the combined calorimeter corresponds to about 10 λ_{int} in both the barrel and end-cap areas. This reduces the possibility of a lateral loss of hadronic showers, commonly known as punch-through, and accomplishes near-hermetic confinement. Given that the initial net transverse momentum in each collision event is essentially zero, this hermeticity allows for the computation of any event's net missing transverse energy (${E_T}^{miss}$). Large ${E_T}^{\mathrm{miss}}$ values might be an indicator of a final-state neutrino, which is the only SM particle that does not interact with the detector.

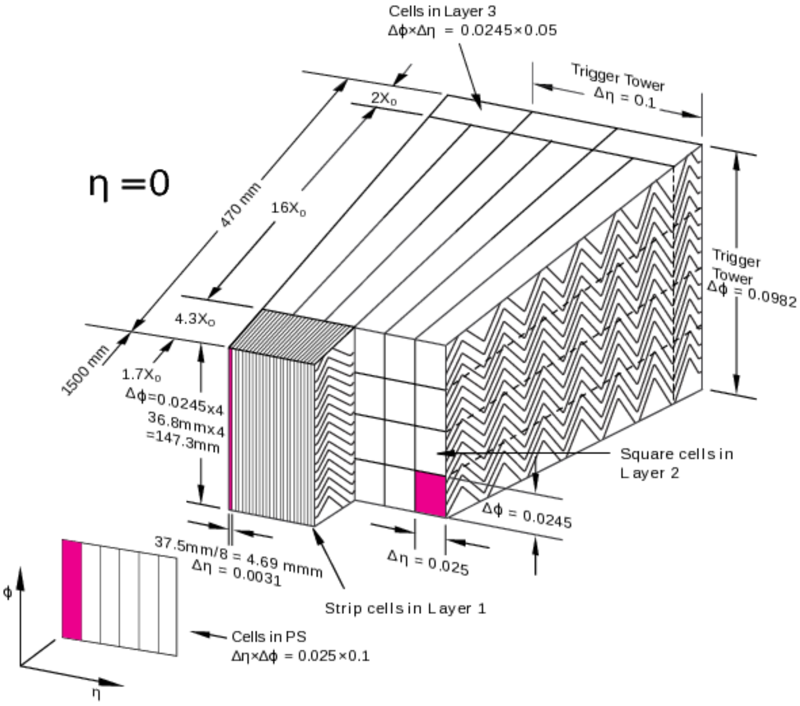

Figure 2.6: Schematic representation of a section of the ATLAS electromagnetic calorimeter (ECAL) at $\eta = 0$ [91].

2.5.1 Electromagnetic calorimeter

The liquid argon (LAr) barrel and electromagnetic end-cap (EMEC) detectors constitute the ECAL, as shown in Figure 2.5. Both of them are accordion-shaped lead-liquid-argon (Pb-LAr) sampling calorimeters, as shown in Figure 2.6 [91]. Due to the lack of possible azimuthal gaps in this design, no particles can escape undetected from the calorimeter. Lead is employed as an absorber material with a $X_0 = 5.6$ mm radiation length [90]. The radiation length of LAr, in comparison, is $X_0 =$ 140 mm [90]. A number of secondary particles are produced in the lead, which causes the incident particles to shower. The LAr active material is then ionised as a consequence of this, and a large number of low-energy electrons drift to the electrodes where they are recorded as a signal. Only a small fraction of the energy of the incident particle is converted into ionisation in sampling calorimeters like the ATLAS ECAL. This is because the particle's remaining energy gets deposited in the absorber material, where it is not visible.

The EMEC, which is built as two coaxial wheels dividing the detector in r with the same extent in z (referred to as the inner and outer wheels), expands coverage to $1.375 < |\eta| < 3.2$ whereas the LAr barrel covers $|\eta| < 1.475$ [91]. The LAr barrel and outer EMEC wheel are composed of the ECAL in the $|\eta| < 2.5$ range, which also includes three depth layers of varying granularity. Precision physics is the focus of this area, which is also covered by ID. The inner EMEC wheel, encompassing $2.5 < |\eta| < 3.2$, contains two depth layers in contrast (at smaller radii r). The first layer, known as the strip layer, is accurately segmented in η, as shown in Figure 2.6 [91], allowing for precision separation of single-photon showers as well as two overlapping showers from neutral pion decays [92]. The three ECAL layers help to determine the lateral and longitudinal shape of electromagnetic showers and to measure their overall energy. Finally, to estimate energy losses in passive material prior to the calorimeter, a presampler detector consisting of a thin active LAr layer is employed. It covers the range $|\eta| < 1.8$. The depth of the ECAL is equivalent to $> 22X_0$ in the LAr barrel and $> 24X_0$ in the EMEC when taken in its entirety. However, the quantity of passive material before the ECAL is up to twice as large as the more central and forward regions in the transition region $1.37 < |\eta| < 1.52$ between the LAr barrel and the EMEC, commonly known as the "crack" zone. Therefore, physics studies rarely employ ECAL measurements in this region. The ECAL alone does not have sufficient capacity to contain hadronic showers since its depth only amounts to about $2\lambda_{int}$.

2.5.2 Hadronic calorimeter

The ATLAS HCAL is developed to absorb hadronic showers that commence or extend past the ECAL. As shown in Figure 2.5, the HCAL is composed of the scintillating-tile calorimeter (TileCal), the LAr hadronic end-cap, and the forward calorimeter (FCal).

The TileCal is a three-layer sampling barrel calorimeter with a range of $|\eta| < 1.7$ [91]. The absorber is a steel bulk that has λ_{int} =16.8 cm [10], and the active medium is scintillating tiles that are interleaved throughout the bulk. The scintillating tiles are comprised of polystyrene that has been doped with approximately 1.5% fluorescent material. The fluorescent molecules get excited by ionising secondary particles produced in the steel absorber and subsequently emit ultraviolet scintillation light. Using photomultiplier tubes (PMTs), wavelength-shifting fibres in contact with the tiles are utilised to read out the scintillation light as signal. The radial depth of the TileCal is approx. $7.4\lambda_{int}$.

In contrast to the accordion shape of ECAL, the HEC copper-liquid-argon (Cu-LAr) sample calorimeter has a flatplate design. The HEC extends the HCAL coverage in the $1.5 < |\eta| < 3.2$ region and is positioned after the EMEC along the beam axis.

Lastly, the FCal provides electromagnetic and hadronic calorimetry in the $3.1 < |\eta| < 4.9$ region. The first FCal layer is made of copper rods, arranged in hexagonal patterns, and is designed for electromagnetic showers. The rods are positioned parallel to the beam and offer quick readings in the area of high forward flux. The remaining two FCal layers, which employ the same layout as the first layer but use tungsten as the primary absorber material surrounding the copper rods, are designed for hadronic showers.

2.5.3 Performance

The reconstruction of electromagnetically interacting particles like photons (γ) and electrons (e) is made possible by the ATLAS ECAL. At $E_T \approx 200$ GeV, it was shown that the relative e/γ energy resolution was approximately 1‰, which is very close to the ATLAS design targets [76].

The information from the ECAL and HCAL detectors is combined to make it possible to reconstruct hadronic jets for ATLAS events. Small-radius (small-R) jets, with a radius parameter of $R = 0.4$, and large-R jets, with a radius parameter of $R = 1$, are the two main types. There are no specific targets for hadronic jets; instead, single charged pion ATLAS calorimeter resolution design targets are provided based on test-beam experiments.

2.6 Muon spectrometer

The calorimeter system absorbs the majority of particles that interact with the ATLAS detector. Muons, with a lifetime of $c\tau \approx 660$ m, are significant exceptions as they do not generally deposit all of their energy in an electromagnetic shower. Energy loss by ionisation will be more significant than radiative processes for particles with energies below a certain critical energy. Muon interactions with matter will be largely ionisation-dominated, even at high energies, since the critical energy for muons is around 40,000 times more than it is for electrons [90]. To measure muons leaving the ATLAS calorimeters, four specialised sub-detectors embedded in and on each side of the toroidal magnet system are used (see Figure 2.7).

The MDTs are using the same detector technology as the TRT to cover the $|\eta| < 2.7$ region. They are built from a barrel component that includes a number of distinct chambers, and two end-cap components. Typically, muons will go through three to four of these chambers, each of which has between three and eight layers of drift tubes with a diameter of 30 mm. The drift tubes in the barrel and end-caps are oriented along ϕ, i.e. parallel to circles about the beam axis, as a result of the field in the toroidal magnet. The MDTs only offer position measurements in two dimensions (r —z), similar to the TRT.

The first end-cap MDT layer is replaced by CSCs due to the high particle occupancy in

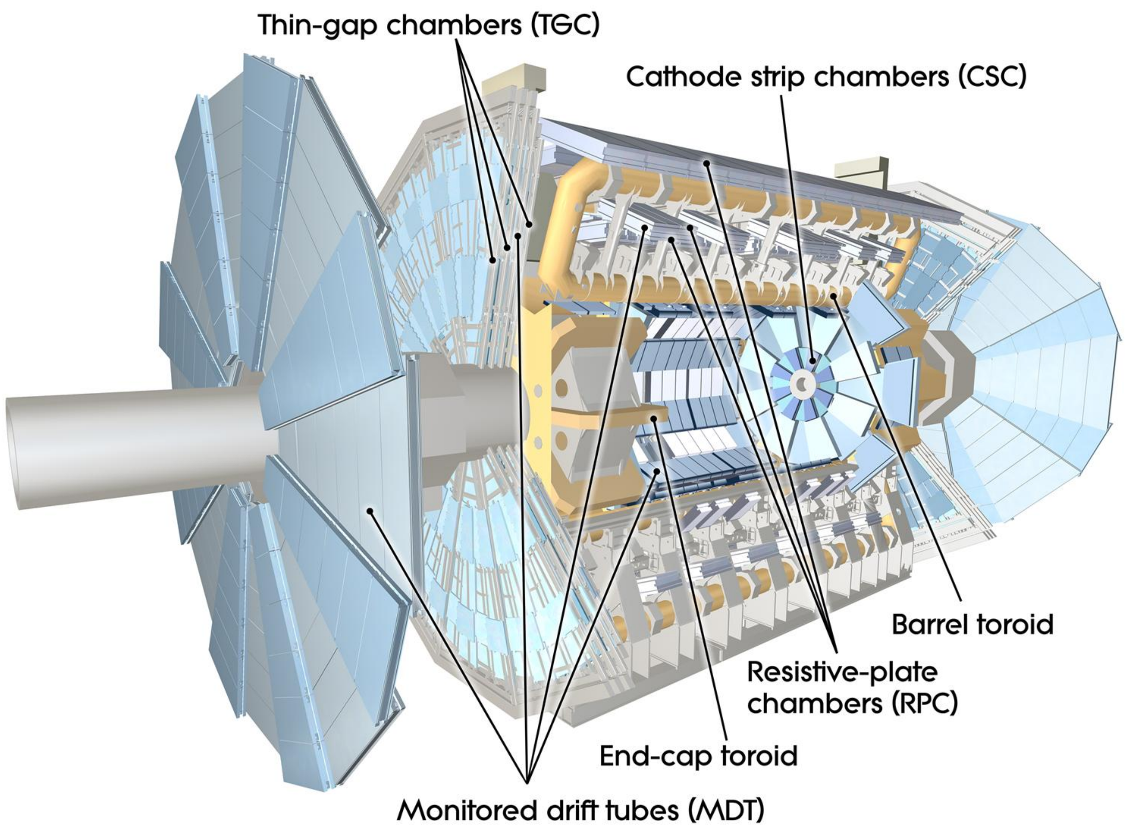

Figure 2.7: Design layout of the ATLAS muon spectrometer (MS), comprised of the monitored drift tube chambers (MDTs), cathode strip chambers (CSCs), resistive-plate chambers (RPCs), and thin-gap chambers (TGCs) [93].

the forward region. Four layers of multiwire proportional chambers make up the CSC in each end cap. The cathode strips are mutually orthogonal and one is placed parallel to the anode wires on each side, while the anode wires are oriented radially. In a multiwire proportional chamber, a charged particle travelling through the gas produces ions, which are read out from both cathode strip planes. As a result, the CSCs allow measurements in both beam-transverse dimensions. The CSCs can operate in high particle fluxes since they cover the forward region $2.0 < |\eta| < 2.7$ and have a drift time of around 40 ns as opposed to the MDTs' drift time of 700 ns [76].

The MDT and CSC sub-detectors offer highly accurate muon measurements across a wide range of pseudo-rapidity, although both have drift durations that are longer than the standard 25 ns LHC bunch spacing. They are, therefore, reinforced by the TGC and RPCs, which offer quick trigger capability for $|\eta| < 2.4$. The RPCs are designed as three concentric layers, each with two active detector layers, in the barrel region ($|\eta| < 1.05$). The RPCs have a temporal resolution of around 5 ns and are built from parallel plate layers with a 2 mm spacing. Each layer is equipped with parallel readout strips that are positioned such that they are orthogonal to one another. The TGCs then cover the forward areas ($1.05 < |\eta| < 2.4$). These are multiwire proportional chambers, with an anode-to-cathode distance that is nearly half that of the CSC. The first and second MDT end-cap layers are encircled by a total of 9 layers that make up the TGCs. In addition to the MDT data, the triggering detectors also offer measurements of the muon ϕ coordinate.

2.6.1 Performance

A relative p_T resolution of 10% for muon tracks with p_T = 1 TeV was the performance requirement that guided the design of the ATLAS MS. The track sagitta, which is approximately 500 µm at 1 TeV and corresponds to a requirement on MS chamber alignment precision to be better than 40 µm, restricts the efficiency of the MS p_T reconstruction [94]. Very limited statistics are available above p_T =200 GeV, although the muon momentum resolution in early Run 2 data has been measured to be better than 4%. Additionally, studies with Run 2 MC simulated data have indicated that it is possible to obtain a muon p_T resolution as low as 7-8 % across η at p_T = 1 TeV by including in situ-deterimined alignment effects in the muon track fitting procedure [94].

2.7 Upgrades

Since its initial installation in 2008 and the subsequent start of data collection in 2010, the ATLAS detector has been undergoing a variety of detector hardware upgrades. Between LHC Runs 1 and 2, during Long Shutdown 1 (LS1), the so-called Phase-0 upgrades were completed. There were a few notable hardware upgrades made during this period, the most distinct ones being the IBL and the reduction in the diameter of the beam pipe near the ATLAS IP [81].

With the completion of Run 2 in 2018, and until July 2022 when Run 3 began at the LHC, the Long Shutdown 2 (LS2) took place, where the majority of the planned Phase-I upgrades were implemented. Included in these was the installation of the new small wheel (NSW) [95], which replaced the old so-called small end-cap wheels, included the CSCs and the majority of the TGCs in the first end-cap layer. Once fully operational (expected in early 2023), the NSW is designed to increase the tracking efficiency and momentum resolution, as well as lower L1 trigger rates in the forward region, $1.3 < |\eta| < 2.7$. The improvements to the ATLAS L1 trigger [96] (detailed in chapter 3) are also important Phase-I additions. The LAr calorimeter system upgrades [97], replacing the existing trigger towers with more finely segmented cell information for each ECAL layer, and the new topological trigger processor (L1Topo), that combines data from the calorimeter and muon systems, enabling the computation of angular separations and invariant masses of physics objects at the L1-level were added. A number of these Phase-I upgrades are being completed in parallel with Run3.

The Phase-II upgrade will be carried out after Run 3, in preparation for the high-luminosity LHC (HL-LHC), with commissioning anticipated during 2026. The Phase-II hardware upgrades consist of the Inner Tracker (ITk), which will substitute out the Phase-I ATLAS ID with an all-silicon Pixel and strip detector covering $|\eta| < 4.0$ [98, 99], and the optional high-granularity timing detector (HGTD), which is expected to improve pile-up mitigation and minimum bias triggering in the forward regions. The ATLAS experiment will be able to maintain low trigger thresholds even at instantaneous luminosities of $L = 5\times 10^{34}\,\mathrm{cm}^{-2}\,\mathrm{s}^{-1}$, as expected at the HL-LHC [100], thanks to the upgrade of the trigger system, which will include a single-layer hardware trigger (L0) with a maximum accept rate of 1 MHz followed by a software-based event filter (EF) with a maximum output rate of 10 kHz.

Part II

ATLAS Trigger Operations

Chapter 3

The ATLAS Trigger

> “*Adventure is out there.*”
>
> Up movie by Pixar

3.1 Overview

The ATLAS trigger system [76] is built to accept scientifically interesting events — those with significant physics or calibration value — for reconstruction and storage, while rejecting others. This is necessary for two reasons. Firstly, it is very expensive to store all events and the maximum rate at which data can be written from the detector to disc (1 kHz) is lower than the maximum rate of collision events (or bunch crossings) (40 MHz) [101]. Secondly, interesting physics processes are not common, therefore, we are interested in a small fraction of the produced events. This selection is carried out by the ATLAS trigger system, which determines whether to record events during data taking in real-time. After data has been collected, as it is described in section 3.1, it is reconstructed into physics objects that are then used for further offline analysis.

There are two main components to the ATLAS trigger system: the custom hardware-based Level 1 (L1) [102] and the software-based High Level Trigger (HLT) [103]. At L1, fast decisions are taken over whether to accept an event and advance it to the HLT for additional processing, resulting in an L1 output rate of 100 kHz. At the HLT level, with an output rate of 1kHz, events go through a series of algorithms where a decision is made whether to keep or discard them. HLT algorithms either use data from the entire detector or, depending

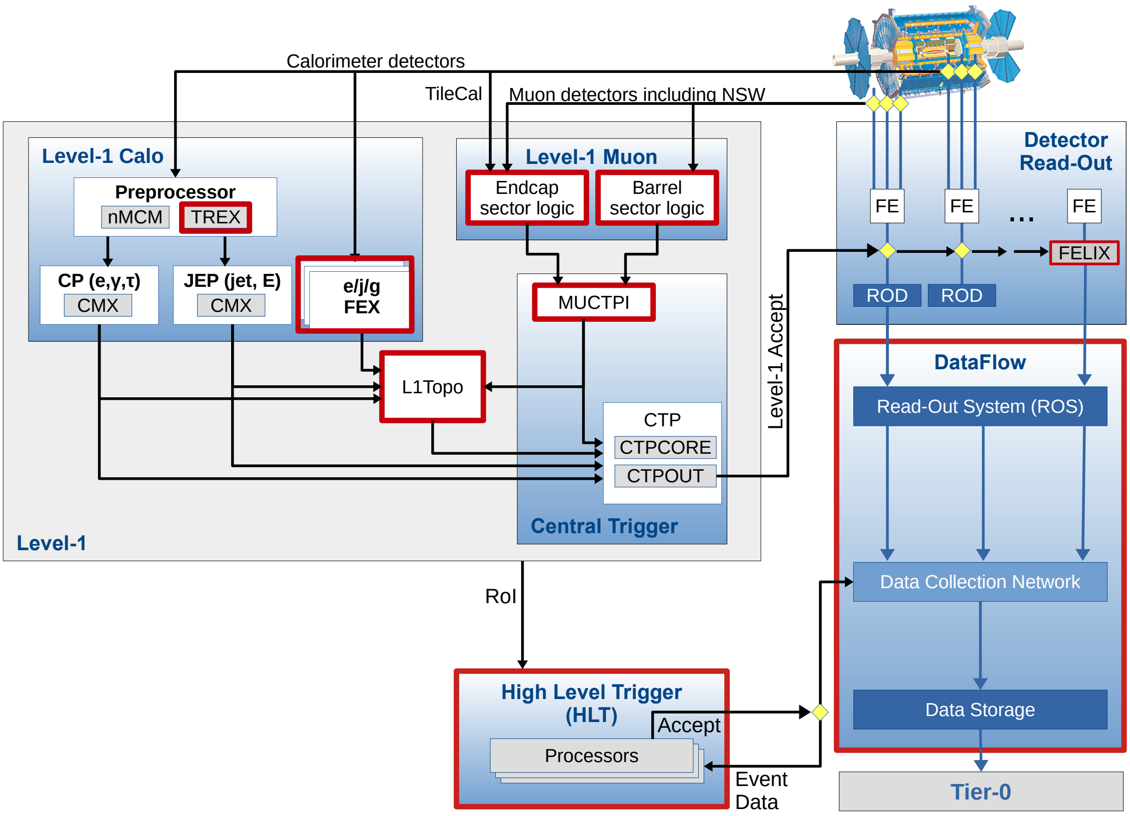

Figure 3.1: Schematic of the ATLAS Trigger and Data Acquisition system with specific focus given to the components of the L1 Trigger system. Run 3 updates (as described in section 2.7 are highlighted in red.

on the algorithm, from a Region of Interest (RoI) inside the detector. A RoI is a region (in η vs. ϕ) of the detector where a physics object candidate has been found using the L1 algorithms. Figure 3.1 illustrates a schematic of the trigger and data acquisition systems.

The L1 trigger is a specialised, synchronous custom hardware-based trigger that employs coarse data from the calorimeter system and the MS, particularly the RPCs and the TGCs. It highlights regions of interest (ROIs) that are typically characterised by high-p_T charged leptons, hadronic activity, or ${E_T}^{miss}$ together with their approximate trajectory direction in η — ϕ with a latency of less than 2.5 µs. Interesting events are accepted by the L1 trigger up to a rate of 100 kHz, and are then forwarded to the HLT for additional filtering.

The HLT is an asynchronous software-based commercial, off-the-shelf hardware, trigger that processes all available detector information, utilising the L1 RoI seeds. It is able to execute more advanced selection algorithms such as charged particle tracking, particle identification and isolation, and jet building to make more sophisticated selections. At a rate of around 1 kHz, events selected by the HLT are stored and can then be used in offline physics studies.

3.2 The Trigger menu

HLT algorithms reconstruct physics objects and apply kinematic selections on the output. Trigger chains composed of an L1 trigger item and a series of HLT algorithms are used to select events. Every chain has a specific physics signature it searches for, such as the presence of leptons, photons, jets, missing transverse momentum, or total energy. For an event to be permanently stored for offline analysis, it must satisfy at least one trigger chain selection.

A prescale value is used to regulate high-rate processes by scaling down approved events. An event has a $1/n$ probability of being kept for a prescale value of n. Each chain can be given a different prescale factor at either L1 or the HLT, and the prescale factor can have any value larger than or equal to one. Prescales may adjust (often in steps) to maintain a constant rate of accepted events in a period of declining collision rates when the amount of protons in each bunch cycling through the LHC gets decreased over time.

The trigger menu [104], which also contains prescales for each trigger chain, consists of the trigger chains are used to collect data [105, 106]. The full set of trigger selections must adhere to all trigger restrictions and exploit the L1 and HLT resources to their fullest potential (e.g., maximum detector read-out rate, available processing resources of the HLT farm, and maximum sustainable rate of permanent storage). The physics priorities of the experiment, which take into account the use cases that a specific trigger chain serves, determine the configuration. The principal triggers (used for physics analyses and which tend to be unprescaled) cover a wide range of signatures relevant to the ATLAS physics programme, which is then utilised for both SM precision measurements and searches for physics beyond the SM.

In reality, each year has a specified pre-designed set of trigger menus. Instead of continuously changing the menu, switches between trigger menus occur when the luminosity increases or decreases above predetermined levels. There are hundreds of trigger chains in a typical trigger menu. A *Super Master Key* (SMK) represents a full distinct online trigger configuration (including the trigger menu and other online software-related characteristics). The *trigger database*, a SQL (Structured Query Language) database that stores trigger-related data, contains the online trigger configuration sets. Every data-taking run has an SMK that accompanies it. One SMK is often used for a number of runs since the trigger menu and online software tend to remain stable over large periods of data-taking.

Additional trigger menus were designed for unique data-taking configurations in addition to the trigger menu used to collect nominal pp collisions. Heavy-ion (HI) collisions are the most notable of them; because they are very different from pp collisions, a special trigger menu is needed to collect the data in HI runs [106].

3.3 Trigger Operations

A shift crew in the ATLAS control room (ACR) is responsible for running and monitoring the ATLAS detector while the LHC is in operation [105]. The crew is supported by a pool of remote experts who are available for on-call assistance. Efficient and high-quality data-taking is the responsibility of shifters and experts.

Two operation coordinators are in charge of the trigger system operation and data quality monitoring [105]. Their primary responsibility is to ensure that data collection is smooth and efficient. They are in charge of a group of experts who are available on-call weekly and rotate among different roles. At a daily trigger operation meeting, operation coordinators and on-call experts maintain contact to plan the day's operations.

The main roles are as follows:

- ACR Trigger Desk Shifter: The person in charge of selecting the appropriate trigger configuration, during their ACR shift. They are in close contact with other ACR shifters to monitor the trigger system operation.

- Trigger Online Expert: Provides primary support for the ACR trigger shifter and is in charge of the smooth operation of the ATLAS trigger.
- Trigger Menu Expert: the person in charge of preparing the trigger menu (configuration of active triggers) and associated prescale factors. (See section 3.2)
- Level-1 Experts: each L1 trigger system (L1Calo, L1Muon barrel, L1Muon endcap, and CTP) has an on-call expert who helps to ensure the optimal operation of the L1 trigger and monitors the data quality for their individual systems.

Other roles involve online release, reprocessing and data quality shifters that are responsible for keeping the online software releases up to date and assessing the data quality of recorded data.

3.4 The Trigger Rate Presenter (TRP)

The ATLAS data acquisition (DAQ) ecosystem, consists of a large number of software packages, from low-level information-sharing applications to middle-ware infrastructure and very high-level frameworks. The guiding principles of the DAQ ecosystem design are the modularity of the various applications and their scalability. It consists of dedicated software applications performing rate summation, computation and publication to the ATLAS Information Service (IS). The IS is the main application responsible for information-sharing between different monitoring software and is considered the backbone of the Online Monitoring Framework.

The TRP [105–107], is the main software used to monitor critical operational features of the ATLAS trigger and data acquisition system during online running. It computes, visualises, keeps track of, and stores the trigger rates and run information. Its goal is to alert shifters and experts to various problems that could seriously impact the quality of data-taking. For example, a sudden drop in a trigger rate can be a result of a malfunction in a detector component and should be treated urgently.

TRP is one of the main software packages of the DAQ ecosystem. It comprises two main components: The so-called adaptors, through the IS, are responsible for computing and keeping track of the trigger rates and publishing them to the trigger database for storage. The second part of TRP is a dedicated GUI client that displays those rates in the control room. The TRP turned out to be one of the most central trigger diagnostic tools during the initial commissioning, in 2009, with the first proton-proton collision data, and it is as relevant now as it was then. Figure 3.2 is a simplistic illustration of the TRP functionality.

Then, the graphical user interface, reads that information from the IS and illustrates it in plots and tables.

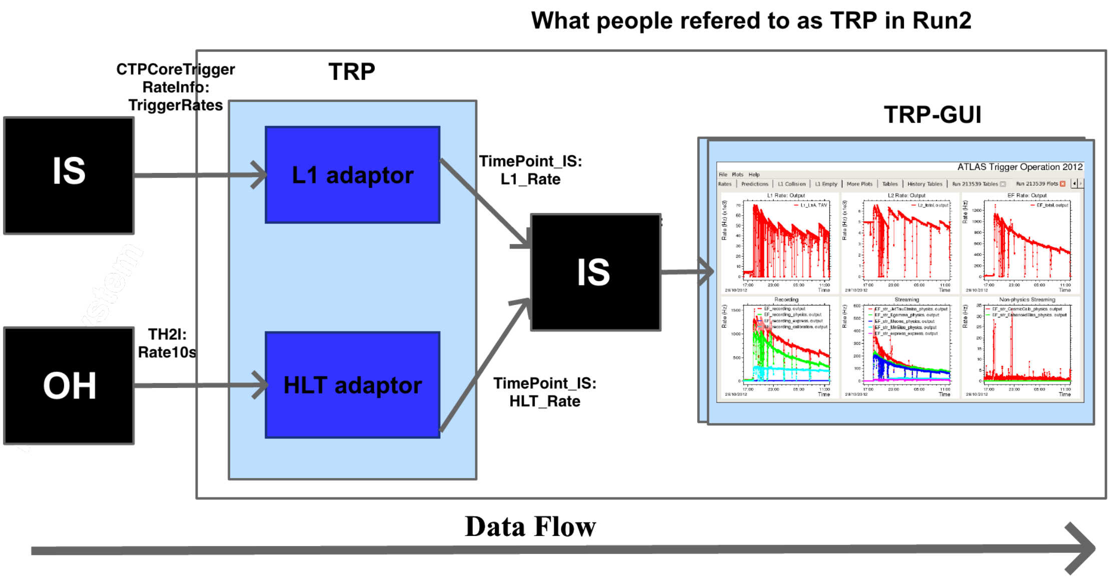

Figure 3.2: A simplistic illustration of the TRP functionality. The TRP adaptors detect changes in the values of trigger rates and histograms - from the IS and Online Histogramming Service (OH) -. They then read the information, restructure it and publish it in a dedicated data format. Then, the graphical user interface, reads that information and illustrates it in plots and tables.

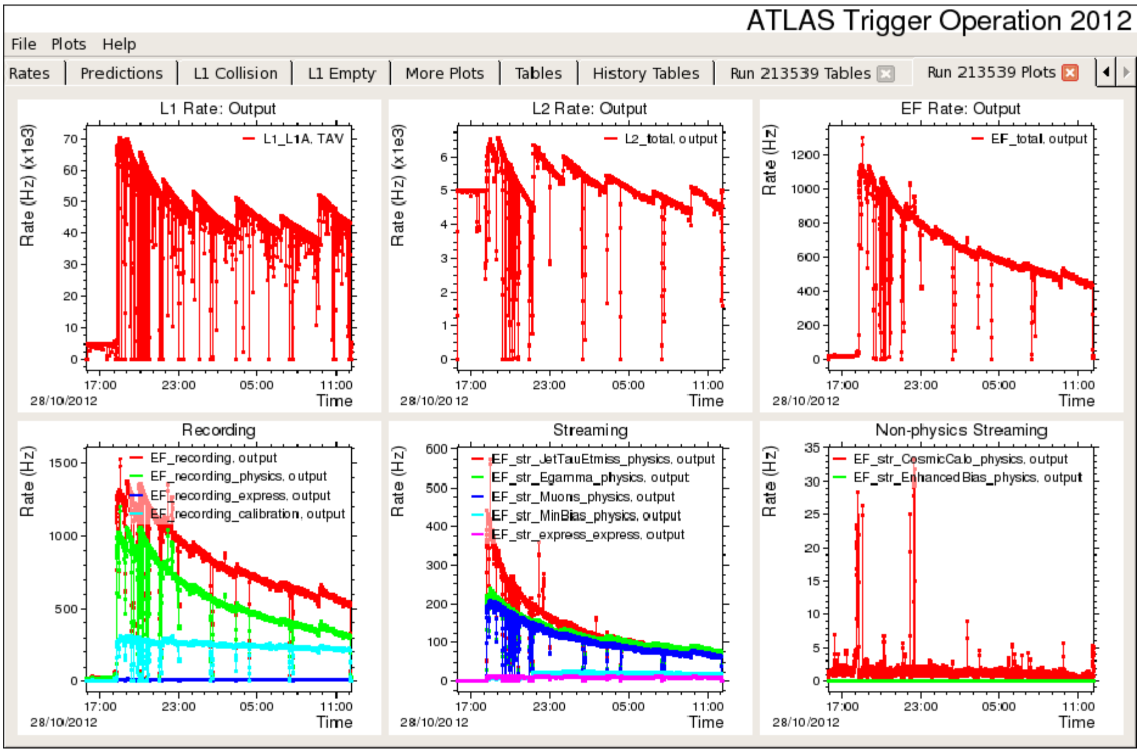

Figure 3.3: A screenshot of the Run2 TRP. **Top:** output rates of the three levels of the trigger system. **Bottom:** Trigger rates for the main physics, calibration, cosmic and express streams

Chapter 4

Involvement in ATLAS Trigger Operations

> “*If a picture is worth a thousand words, then what is worth a thousand pictures? A dashboard.*”
>
> the internet

4.1 Developing the new TRP for Run3

The ATLAS Trigger Rate Presenter (TRP), introduced in section 3.4 is a very powerful monitoring tool and has served the ATLAS experiment greatly during runs 1 and 2 of data taking. Through those years of experience, there is now a much better understanding of the monitoring needs of the experiment and desired features.

During the LS2 it was decided that it was necessary to invest some resources in developing a new TRP that will be used during data taking in Run3 and beyond. The main drawbacks of the Run2 TRP were that historic and live data were treated separately, off-site access (outside of ACR) was cumbersome and slow, and, throughout the years, a lot of redundant code has been piling-up, making maintenance harder. It was also time to give a fresh, easier-to-use, design to TRP!

After evaluating different possibilities, it was decided to replace the graphical interface part of TRP with Grafana [108], an open-source monitoring suite, and extend the adaptor part of the TRP software package to work with that. This had just recently become possible via the newly developed PBEAST, a back-end for the IS, collecting and archiving all information published by various applications.

During my PhD, initially as part of my qualification task, and then out of interest, I was responsible for all aspects of TRP. Those generally fall into three categories. The first one involved the maintenance of the - now - legacy Run2 TRP until formal commissioning of the new tool, and to give adequate time for different subcomponents to adjust. Day-to-day work concerned releasing patches to keep the software package up-to-date with the updates taking place during the LS2. The second category was about extending the existing adaptor part of TRP so that it would broadcast information in a suitable format to be visualised by Grafana dashboards. This drove the implementation decisions, regarding how to best upgrade each adaptor but also to keep the framework as lightweight as possible. It is also the most programming-heavy part. The third category of tasks covered the new Grafana Dashboard UI, being the front-end of TRP . It was initially constructed to be as close as possible, visually, to the Run2 TRP GUI, and then taking under consideration the feedback and comments of the Trigger experts and shifters, it evolved even further.

Below, I include a small representative selection of the tasks I worked on.

4.1.1 Updating the TRP adaptors to a new format

Once starting work on TRP, it soon became clear that the current structure (called TimePoint_IS) used for communication between the adaptor and Graphical User interface part of the TRP was not suitable to be used between the adaptors and Grafana PBeast dashboards. As can be seen in figure 4.2, the issue arose from the fact that a single instance of the TimePoint_IS class was being published containing all the information about every chain; essentially in large lists. This meant that to request a specific rate, the user would have to know its index in this list of rates. This, on top of being non-intuitive, is prone to errors, since trigger rates change between runs.

Instead, following consultation with many experiment experts, two new IS structures were created, separately for L1 and HLT rates. Each instance of those classes would carry information about a single trigger rate, and the name of the instance is also the name of the trigger item. Then as many instances as there are trigger items are being published (compared to one instance containing everything). An example of this class can be seen in figure 4.3.

The L1 and HLT adaptors were updated to also broadcast in the new classes format, by the

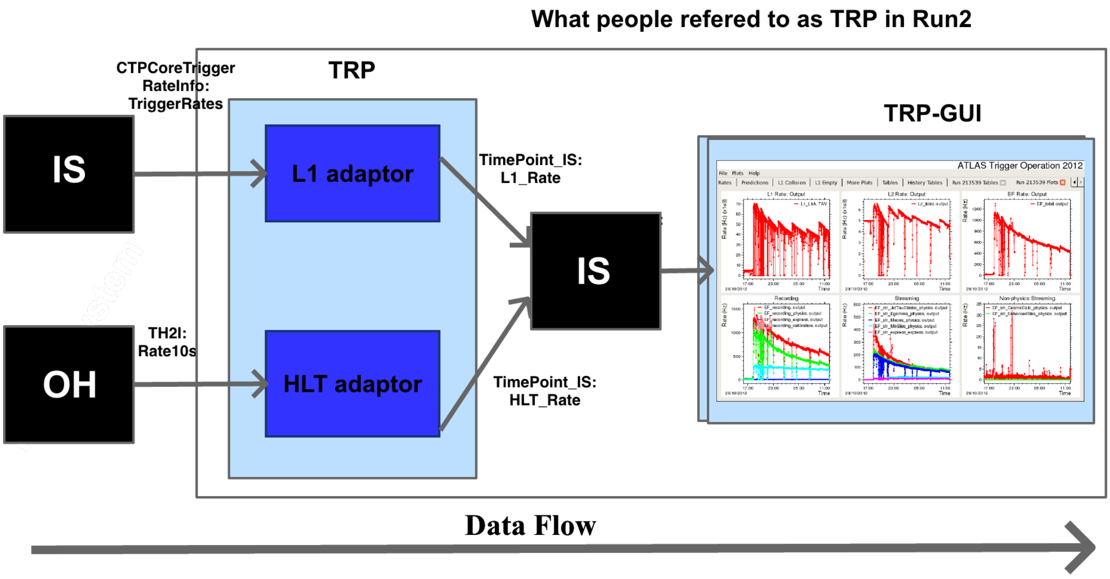

(a) The design of Run 2 TRP. Each adaptor reads information from the IS or OH and publishes a single class containing all the trigger rates. The TRP gui then reads and displays the information.

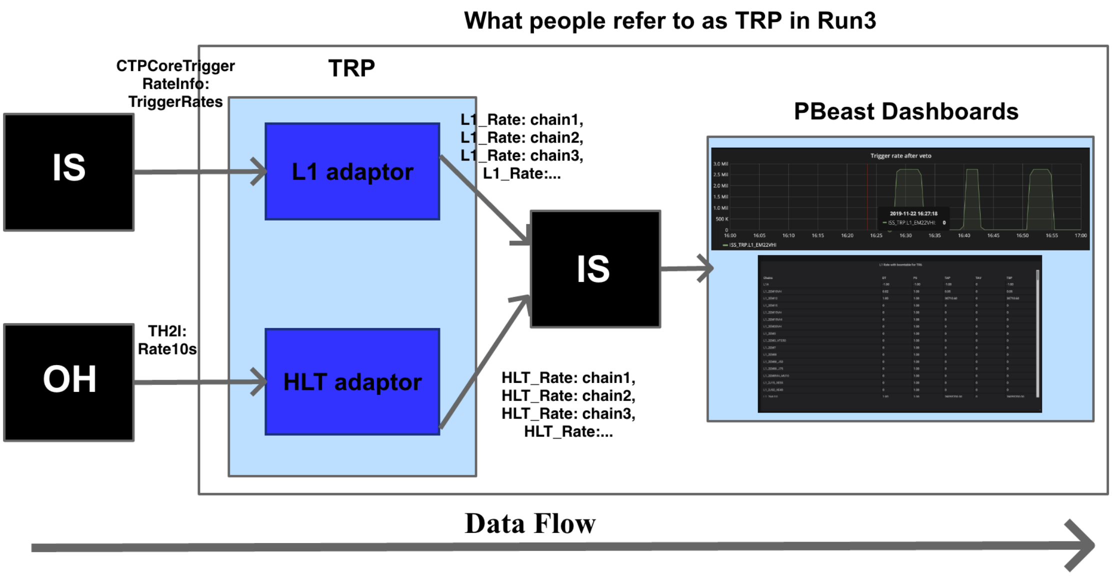

(b) The design of Run 3 TRP. Each adaptor reads information from the IS or OH, and publishes a single class per trigger chain. A Grafana dashboard then reads and displays the information.

Figure 4.1: Simplistic comparison between the structure of Run2 and Run3 TRP implementations

addition of a new mode. This worked well, and the first working prototype of the Run3 TRP was in place! Since then a lot more TRP adaptors have been updated to the new format without issues.

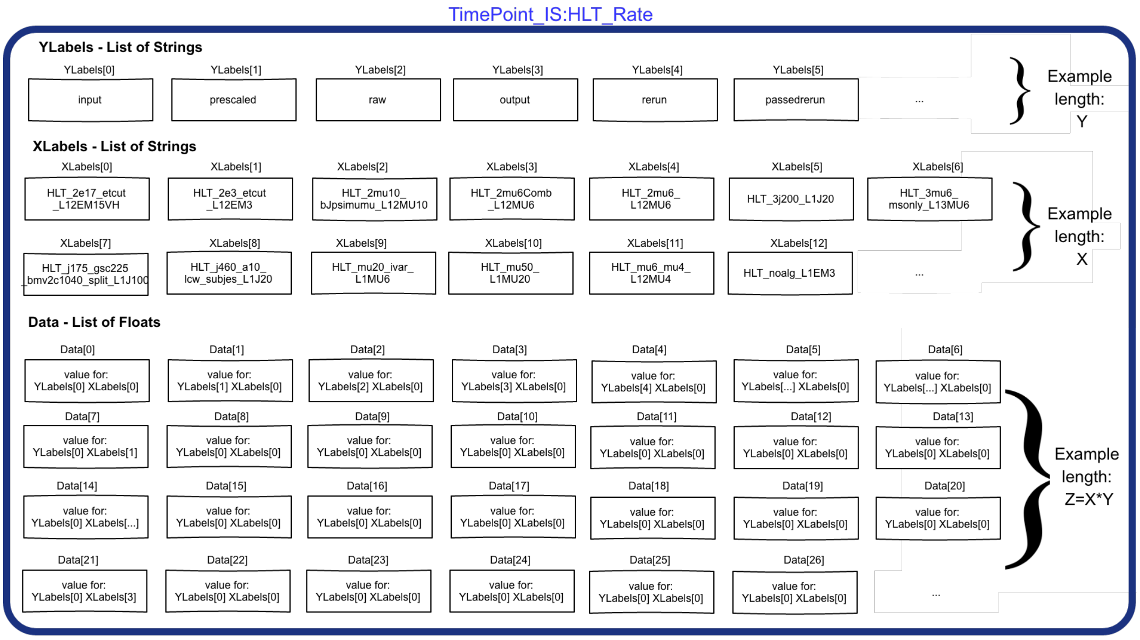

Figure 4.2: Illustration of the class used by TRP to broadcast monitoring information during Run 2. It essentially comprises of three lists. Y: labels of the HLT rate features, X: labels of the trigger chains, Data: a list with length X*Y containing the numerical values of the rates.

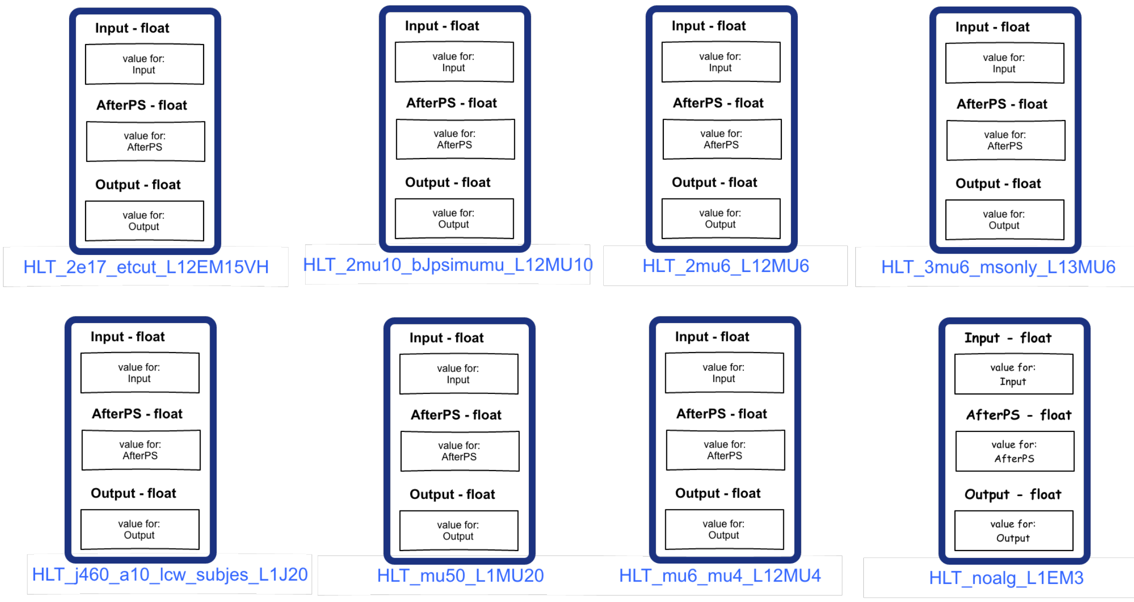

Figure 4.3: Illustration of the class used by TRP to broadcast monitoring information during Run 3. Each instance of the class contains the values for a single trigger rate. Multiple instances of the class are being published (one for each trigger rate). Using this approach, the trigger rates can be selected by name in the new Grafana dashboard.

4.1.2 Developing the Front Page of the new TRP

Once the first working prototype of Run3 TRP was in place, it had to evolve into a tool that would be useful for Trigger shifters and experts to use. It was initially created to be visually close to the Run2 TRP since this was already a good starting point.

Third-party extension plugins were used to provide functionality for correlation plots and sortable tables. Grafana dashboard-level variables were implemented to make the dashboard more dynamic, for example, the choice of partition, or to provide rate filtering by regular expressions. A new section was added as well, providing an overview of the run. Many other implementation decisions were made, for example, user read/write access permissions.

The result can be seen in figure 4.4. For the past three years, the new TRP has been extensively used by Trigger shifters and experts during commissioning successfully. ATLAS has collected a great amount of feedback and continues to improve the dashboard further.

For the past few months, since the start of Run3, the new TRP has been used during data taking successfully.

4.1.3 Auxiliary work

This section very briefly mentions a number of TRP features that I was involved with.

A few of the existing TRP adaptors were developed using older, more resource-demanding structures, posing the danger to saturate the IS (used to share information between applications in a distributed environment) network traffic and affect the full Trigger and Data Acquisition (TDAQ) ecosystem. Though it was not necessary to update those adaptors to a different Run3 format, I worked on investigating the issues and making them computationally lighter.

I have also worked on investigating ways to make historic Run1 and Run2 data available from the Grafana dashboards and also ways to store trigger rates for offline analysis at a later time. Those topics are still open, while early Run 3 data are being analysed by the community.

Since September 2021, PhD student Julia Allen has taken over the TRP development from me, and I have shifted to training and providing expertise when needed. Through this new role, I have helped with a number of tasks, such as further improving the labels and structure of the dashboard, investigating edge cases that were causing the adaptors to crash or missing time periods, and adding functionality to display only enabled or only disabled (ie not part of the current trigger menu) rates.

4.2 Trigger Operations

My involvement with TRP required knowledge of a few different ATLAS components (IS, TDAQ, Trigger menu, etc). Thus, I became familiar with Trigger Operations and Trigger in general. I had the opportunity to take part in quite a few Technical runs and Milestone weeks (almost all of them) during the LS2 and early Run3. Throughout the first years, when the updates to the TDAQ software packages were frequent, I contributed mostly by releasing patches for the different software packages to keep them working and in harmony with each other. More recently, while ATLAS was getting ready for Run3, I have undertaken shifts as Trigger Expert at the ACR. During data-taking periods, those shifts are typically on-call, but during the commissioning stage, they mostly involved physically being at the ACR, running Trigger tests, aiding the different subcomponents with their tests, and providing the correct trigger rates. In the case of errors, I was also there to help the different sub-component teams understand and solve issues that arose, as fast as possible.

My work outlined in this chapter is described in the publication: *Operation of the ATLAS trigger system in Run 2* [1]. I also represented the ATLAS experiment during ICHEP 2022, giving a talk on the ATLAS Trigger System for Run3.

Figure 4.4: A snapshot of the TRP monitoring display as seen by a shifter in the ATLAS control room.

Part III

A search for Heavy Neutrinos

Chapter 5

Introduction

In section 1.2 - 1.5, a few selected issues with the standard model were discussed along with the Seesaw mechanism and the LRSM as possible extensions. In section 1.6 the KS process was introduced as a way to experimentally test these exotic models, and section 1.6.1 presented the latest experimental exclusion limits for the KS process so far.

We present a search for heavy right-handed Majorana or Dirac neutrinos (N_R) and heavy right-handed W gauge bosons (W_R) participating in the KS process that has been performed in events with a pair of energetic electrons or muons and two energetic jets. Events were selected from pp collision data with an integrated luminosity of 139 fb^{-1} collected by the ATLAS detector at $\sqrt{s}$ = 13TeV.

The analysis has two main channels: resolved - reconstructing all four final state particles separately - and boosted - collimated particles are reconstructed as a single object -, depending on the mass difference between W_R and N_R. As a rule of thumb, the boosted channel is more sensitive when m(W_R) > 10 m(N_R), while the rest of the m(W_R) vs m(N_R) phase-space is covered by the resolved channel. Fig. 6.2 shows the complete phase-space covered by the two channels.

Furthermore, the resolved channel is analysed separately in Opposite-sign and Same-sign channels, referring to the relative charge sign of the two final state leptons. Under the LRSM, if the N_R is a Dirac particle the two final state leptons will always have opposite sign charges. If the N_R is a Majorana particle (i.e. its own antiparticle), the dileptons will appear as 50-50 admixture of opposite sign (OS) same sign (SS) charges. This means that the OS channel is sensitive to both Majorana and Dirac neutrinos while pairing it with the SS channel increases the overall sensitivity to a Majorana neutrino. The OS channel has more statistics than the SS, but the latter has a much cleaner background.

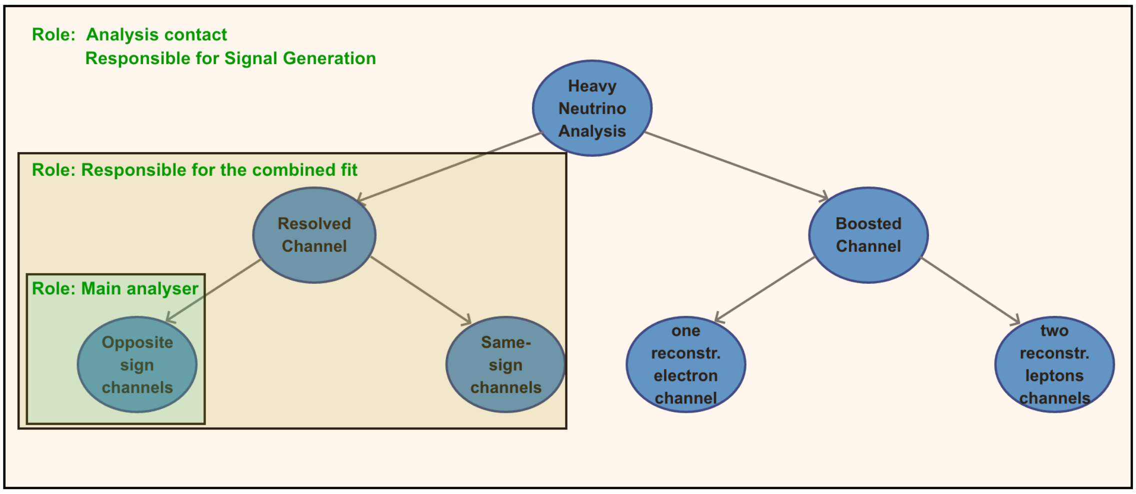

Figure 5.1: Diagram illustrating a channel-breakdown of the Heavy Neutrino analysis and my involvement in them. I was one of the two analysis contacts, mainly responsible for the resolved channel. I was responsible for generating signal samples for all analysis channels. I was the main analyser for the resolved Opposite-sign channel. I was responsible for the combined resolved OS & SS fit.

My overall involvement in the analysis is as follows. I was one of the two analysis contacts, mainly responsible for the resolved channel. I was responsible for generating and deriving signal samples for all analysis channels. I was the main analyser for the resolved Opposite-sign channel. I was involved in the decision-making and occasionally lent a hand to the resolved Same-sign channel, due to the limited manpower of their team. I was responsible for the combined resolved OS & SS fit. Though I was not involved in the work of the boosted channel team (aside from preparing the signal samples and presenting the combined analysis), the resolved and boosted teams were in constant communication and cooperation.

To best reflect my contribution to the analysis, the breakdown of this part is as follows: Chapter 6 presents the datasets used in the analysis split into experimental data, simulated background and simulated signal. Chapter 7 discusses the definition and selection of the events and main physics objects of the analysis: electrons, muons, and jets. Chapter 8 shows the methodology for estimating the Standard Model background for the resolved OS channel, while chapter 9 the statistical analysis and search results for both the OS & SS channels. Finally, chapter 11 is a discussion of the combined results for both the resolved and boosted channels.

Chapter 6

Datasets

This analysis performs a search for the hypothesised KS process (the "signal") in a dataset collected by the ATLAS experiment. Simulated datasets are produced for the dominant SM processes contributing to the targeted experimental final state (the "backgrounds"), as well as for the benchmark signal process, using Monte Carlo (MC) event generators. Using these simulated datasets, the analysis will assess the compatibility of the experimentally recorded data yields with the rates from known SM processes, as well as from potential BSM processes involving heavy right-handed Majorana or Dirac neutrinos (N_R) and heavy right-handed W gauge bosons (W_R). The following sections describe the experimentally recorded, and MC-simulated, datasets used in the analysis.

6.1 Experimental data

The data used in this analysis were collected during 2015, 2016, 2017 and 2018. The average number of pp interactions per bunch crossing (pile-up) in the dataset is 33.7. The combined 2015 – 2018 integrated luminosity amounts to $L_{int} \approx 139$ fb^{-1} with the uncertainty of 1.7% [109], obtained using the LUCID-2 detector [110] for the primary luminosity measurements. The absolute luminosity scale was determined using van der Meer scans during dedicated running periods in each year and extrapolated to the physics data-taking regime using complementary measurements from several luminosity-sensitive detectors.

All of the data collected by the ATLAS detector is divided into Luminosity Blocks (LB) and all of the data in one luminosity block has approximately constant instantaneous luminosity

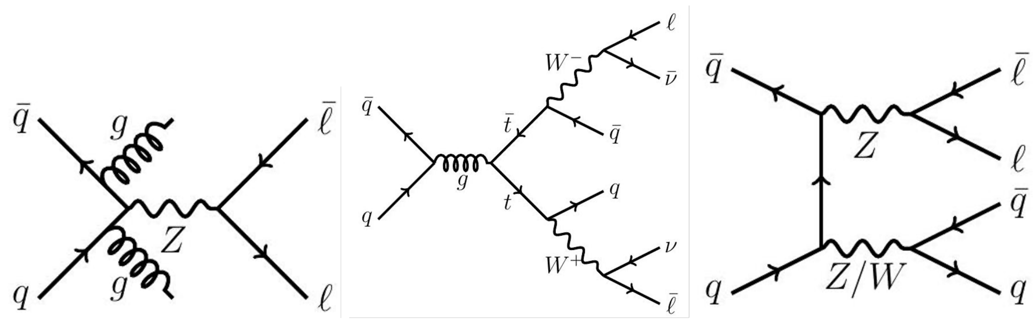

(a) Z + jets (b) $t\bar{t}$ (c) Diboson

Figure 6.1: Example Feynman diagrams for the main SM backgrounds to the KS process.

and the same data-taking conditions. Luminosity blocks are usually about a minute long. Among all of the luminosity blocks, only the ones where the LHC has declared stable beams and all of the sub-detectors reported to be operating well are used. This information is collected into the so-called good run lists (GRL). Four GRLs are used in this analysis corresponding to data collected in 2015, amounting to $L_{int} \approx 3.2$ fb^{-1} , in 2016 amounting to $L_{int} \approx 33.0$ fb^{-1} , in 2017 amounting to $L_{int} \approx 44.3$ fb^{-1}, and in 2018 amounting to $L_{int} \approx 58.4$ fb^{-1}, named

```
data15_13TeV.periodAllYear_DetStatusv89pro2102_Unknown_PHYS_StandardGRL_All_Good_25ns,
data16_13TeV.periodAllYear_DetStatusv89pro2101_DQDefects000204_PHYS_StandardGRL_All_Good_25ns,
data17_13TeV.periodAllYear_DetStatusv99pro2201_Unknown_PHYS_StandardGRL_All_Good_25ns_Triggerno17e33prim,
data18_13TeV.periodAllYear_DetStatusv102pro2204_Unknown_PHYS_StandardGRL_All_Good_25ns_Triggerno17e33prim
```

6.2 Simulated background

The term “background processes" is used to describe a number of SM processes that might result in a $\ell\ell jj$ ($\ell = e, \mu$) final state with opposite-sign or same-sign leptons. The following background processes are dominant:

- Z + jets: $Z/\gamma^*(\rightarrow l^+l^-) + jj$, see figure 6.1a
- $t\bar{t}$: $t\bar{t} \rightarrow l^+l^-jj$, see figure 6.1b
- diboson: $ZZ/WZ \rightarrow l^+l^-jj$, see figure 6.1c

The SM Drell-Yan process ($Z \rightarrow ee, Z \rightarrow \mu\mu$), from figure 6.1a, is simulated using the Sherpa 2.2.11 event generator [111]. Matrix elements are calculated for up to 2 partons at NLO and 4 partons at LO using Comix [112] and OpenLoops [113] and merged with the Sherpa parton shower [114] according to the `ME+PS@NLO` prescription [115]. The NNPDF3.0NNLO [116] PDF set is used.

Diboson processes with 4 charged leptons, 3 charged leptons + 1 neutrino or 2 charged leptons and 2 neutrinos are simulated with the Sherpa 2.2.2 event generator [111]. Matrix elements contain all diagrams with four electroweak vertices. They are calculated for up to 1 (4l, 2l+2v) or 0 partons (3l+1v) at NLO and up to 3 partons at LO using Comix and OpenLoops, and merged with the Sherpa parton shower according to the ME+PS@NLO prescription. The NNPDF3.0NNLO PDF set is used in conjunction with dedicated parton shower tuning. The event generator cross sections are used in this case (already at NLO).

The $t\bar{t}$ process is predicted by the NLO QCD generator Powheg-Box v2 [117–119] which is interfaced to Pythia 8.230 [120] for parton showering. The A14 parameter set [121] is used for tuning the shower. The NNPDF3.0NNLO PDF set enters in the matrix element calculation while it is NNPDF2.3NLO [122] in the parton shower. Additionally, top-quark spin correlations are preserved through the use of MadSpin [123]. The predicted $t\bar{t}$ production cross-section is $831.8^{+19.8}_{-29.2}$ (scale) $\pm$ 35.0 (PDF + α_S) pb as calculated with Top++2.0 [124] to NNLO in perturbative QCD, including soft-gluon resummation to next-to-next-to-leading-log order. The top-quark mass is assumed to be 172.5 GeV. The scale uncertainty results from an independent variation of the factorisation and renormalisation scales, while the second uncertainty is associated with variations of the PDF set and α_S, following the PDF4LHC [125] prescription using MSTW2008 68 % CL NNLO [126], CT10 NNLO [127], and NNPDF2.3 PDF.

Physics process	Event generator	ME PDF set	Cross-section norm.	Parton shower	Parton shower tune
Signal	MadGraph5_aMC@NLO	NNPDF3.1NLO	LO	Pythia 8.230	A14
Drell-Yan					
$Z/\gamma\star \rightarrow e^+e^-/\mu^+\mu^-/\tau^+\tau^-$	Sherpa 2.2.11	NNPDF3.0NNLO	NLO	Sherpa	Sherpa default
Top physics					
tt^-	Powheg-Box v2	NNPDF3.0NNLO	NNLO	Pythia 8.230	A14
Single t	Powheg-Box v2	NNPDF3.0NNLO	NNLO	Pythia 8.230	A14
Diboson					
ZZ, W Z	Sherpa 2.2.1 & 2.2.2	NNPDF3.0NNLO	NLO	Sherpa	Sherpa default
Multiboson					
WWW, WW Z, W ZZ, ZZZ	Sherpa 2.2.1 & 2.2.2	NNPDF3.0NNLO	NNLO	Sherpa	Sherpa default

Table 6.1: Simulated signal and background event samples: the corresponding event generator, parton shower, cross-section normalisation, PDF set used for the matrix element and set of tuned parameters are shown for each sample. The generator cross-section of the generator used to generate the sample is used where not specifically stated otherwise.

Other minor backgrounds in the analysis are multiboson, single top and raretop processes.

DSID	Sample	Comments
363355	Sherpa_221_NNPDF30NNLO_ZqqZvv	
363356	Sherpa_221_NNPDF30NNLO_ZqqZll	
363357	Sherpa_221_NNPDF30NNLO_WqqZvv	
363358	Sherpa_221_NNPDF30NNLO_WqqZll	
363359	Sherpa_221_NNPDF30NNLO_WpqqWmlv	
363460	Sherpa_221_NNPDF30NNLO_WplvWmqq	
363489	Sherpa_221_NNPDF30NNLO_WlvZqq	
364250	Sherpa_222_NNPDF30NNLO_llll	
364288	Sherpa_222_NNPDF30NNLO_llll_lowMllPtComplement	
364253	Sherpa_222_NNPDF30NNLO_lllv	
364289	Sherpa_222_NNPDF30NNLO_lllv_lowMllPtComplement	
364254	Sherpa_222_NNPDF30NNLO_llvv	
364290	Sherpa_222_NNPDF30NNLO_llvv_lowMllPtComplement	
364255	Sherpa_222_NNPDF30NNLO_lvvv	
363494	Sherpa_221_NNPDF30NNLO_vvvv	
364283	Sherpa_222_NNPDF30NNLO_lllljj_EW6	
364284	Sherpa_222_NNPDF30NNLO_lllvjj_EW6	
364285	Sherpa_222_NNPDF30NNLO_llvvjj_EW6	
364286	Sherpa_222_NNPDF30NNLO_llvvjj_ss_EW4	
364287	Sherpa_222_NNPDF30NNLO_llvvjj_ss_EW6	
345705–345706	Sherpa_222_NNPDF30NNLO_ggllll_*	
345715	Sherpa_222_NNPDF30NNLO_ggllvvInt	
345718	Sherpa_222_NNPDF30NNLO_ggllvvWW	
345723	Sherpa_222_NNPDF30NNLO_ggllvvZZ	
364302	Sherpa_222_NNPDF30NNLO_ggZllZqq	
364303	Sherpa_222_NNPDF30NNLO_ggZvvZqq	
364304	Sherpa_222_NNPDF30NNLO_ggWmlvWpqq	
364305	Sherpa_222_NNPDF30NNLO_ggWplvWmqq	
364242–364249	Sherpa_222_NNPDF30NNLO_WZ*_*_EW6	
407311–407315	Sherpa_221_NNPDF30NNLO_*_EW6	
364100–364113	Sherpa_221_NNPDF30NNLO_Zmumu_*	
364198–364203	Sherpa_221_NNPDF30NNLO_Zmm_Mll10_40_*	
354281	Sherpa_221_NNPDF30NNLO_Zmumu_Mll2Ml_MAXHTPTV280_E_CMS	
364114–364127	Sherpa_221_NNPDF30NNLO_Zee_*	
364204–364209	Sherpa_221_NNPDF30NNLO_Zee_Mll10_40_*	
354280	Sherpa_221_NNPDF30NNLO_Zee_Mll2Ml_MAXHTPTV280_E_CMS	
364128–364141	Sherpa_221_NNPDF30NNLO_Ztautau_*	
364210–364215	Sherpa_221_NNPDF30NNLO_Ztt_Mll10_40_*	
354282	Sherpa_221_NNPDF30NNLO_Ztautau_Mll2Ml_MAXHTPTV280_E_CMS	
364156–364169	Sherpa_221_NNPDF30NNLO_Wmunu_*	Fake estimation only
364170–364183	Sherpa_221_NNPDF30NNLO_Wenu_*	Fake estimation only
364184–364197	Sherpa_221_NNPDF30NNLO_Wtaunu_*	Fake estimation only
410470	PhPy8EG_A14_ttbar_hdamp258p75_nonallhad	Fake estimation only
410471	PhPy8EG_A14_ttbar_hdamp258p75_allhad	Fake estimation only
410472	PhPy8EG_A14_ttbar_hdamp258p75_dil	Analysis regions only
410644–410645	PowhegPythia8EvtGen_A14_singletop_schan_lept_*	
410646–410647	PowhegPythia8EvtGen_A14_Wt_DR_inclusive_*	Fake estimation only
410648–410649	PowhegPythia8EvtGen_A14_Wt_DR_dilepton_*	Analysis regions only
410658–410659	PhPy8EG_A14_tchan_BW50_lept_*	
410155–410157	aMcAtNloPythia8EvtGen_MEN30NLO_A14N23LO_tt*	
410218–410220	aMcAtNloPythia8EvtGen_MEN30NLO_A14N23LO_tt*	
410081	MadGraphPythia8EvtGen_A14NNPDF23_ttbarWW	
304014	MadGraphPythia8EvtGen_A14NNPDF23_3top_SM	
410080	MadGraphPythia8EvtGen_A14NNPDF23_4topSM	

Table 6.2: Background samples used in the analysis with their corresponding Dataset IDs (DSID).

6.3 Simulated signal

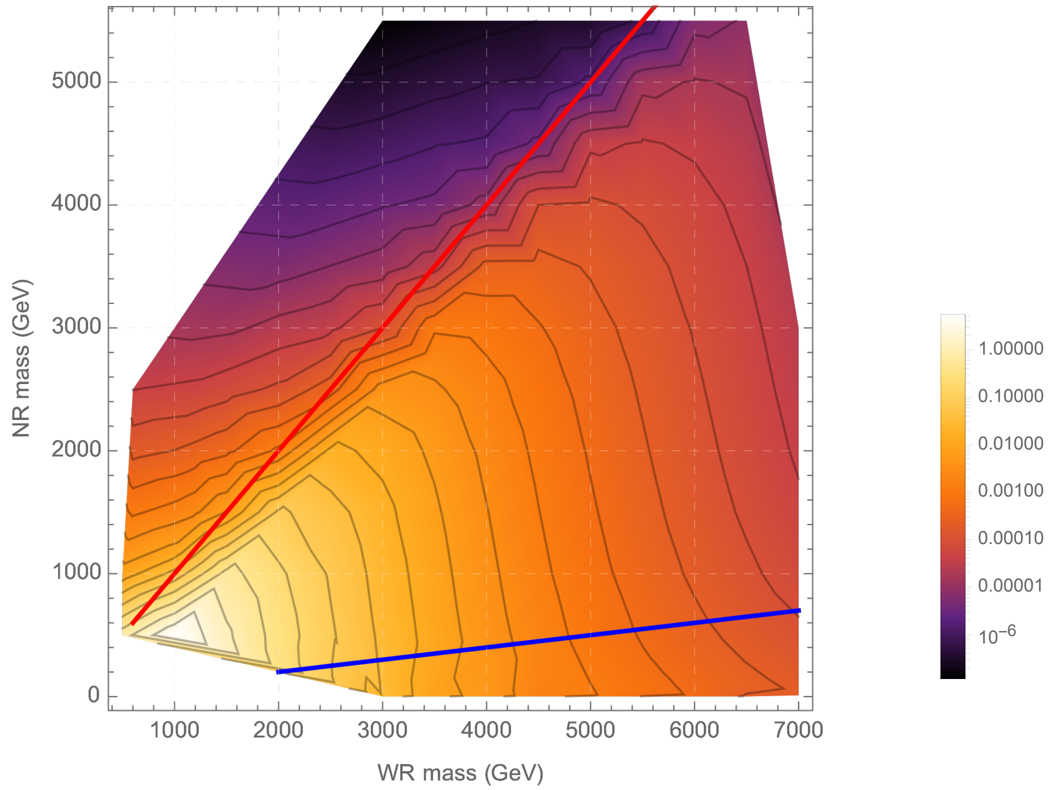

Figure 6.2: Cross section (in pb) of the KS process across the m(W_R) vs m(N_R) phase-space. The red line corresponds to the two BSM particles' masses being equal, while the blue line roughly to where the sensitivity of the resolved channel rapidly drops.

The model used to simulate the KS process is based on the Type-I Left-Right Symmetric Model [128]. It was produced with the Mathematica package FeynRules [129], and further modified for use initially in [61] by Fabrizio Nesti (IRB, Zagreb), Miha Nemevsek (JSI, Ljubljana), and Xanthe Hoad [130]. For the current analysis, the same model parameter values as [61] were set. More details of the model parameters can be found in [128, 130], while below a summary is provided:

- g_R, the right-handed weak coupling strength, was set equal to g_L, the SM weak coupling strength. The left- and right-handed coupling strengths are required to be equal to ensure that the model is invariant under parity transformations.
- κ', the parameter that controls mixing between the SM W and the LRSM W_R, was set to zero, for simplicity.
- The mixing between heavy and light neutrinos was also set to zero, again for

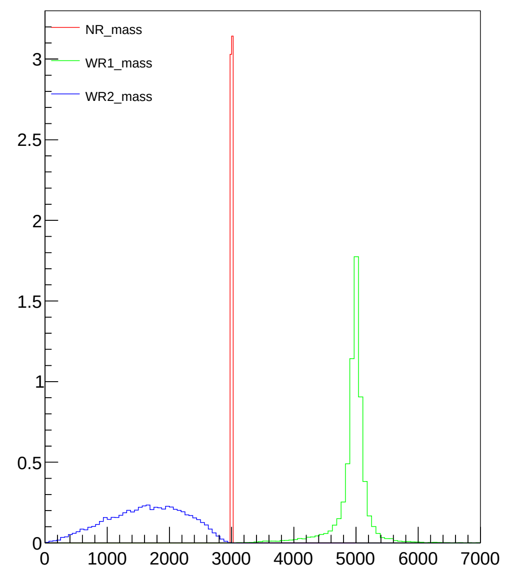

(a) W_R mass = 5 TeV, N_R mass = 3 TeV

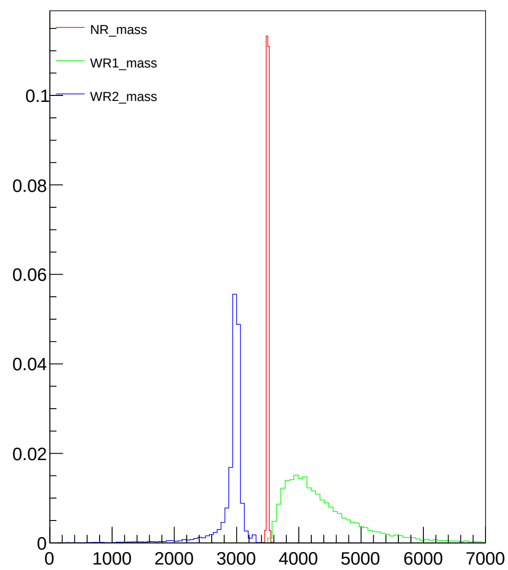

(b) W_R mass = 3 TeV, N_R mass = 3.5 TeV

Figure 6.3: Example signal distributions for 6.3a the nominal case where $m_{W_R} > m_{N_R}$: the on-shell W_R mass can be reconstructed from the invariant mass of the $\ell\ell jj$ system, and 6.3b the inverse hierarchy, where the $m_{W_R} < m_{N_R}$: the second W_R in the decay chain is now on-shell and can be reconstructed from the invariant mass of the jj system. WR1 denotes the first W_R in the decay chain, while WR2, the second.

simplicity.

- The mixing between N_e, N_μ and N_τ was set to zero so that only final states with the same flavour leptons were generated.

- v_R, the VEV of the Higgs triplet ΔR, κ , the non-zero VEV of ϕ, and the couplings between the Higgs fields and the leptons and quarks, were set based on the values chosen for m(W_R) and m(N_R) and the known masses of the other particles.

- The right- and left-handed Cabibbo–Kobayashi–Maskawa (CKM) matrices [131, 132] that determine the mixing between right- and left-handed quarks, were set to be equal to the SM CKM matrix, again to ensure the invariance of the model under parity transformations.

The KS process considered in the thesis was generated using MadGraph5_aMC@NLO [133] generator at leading-order (LO). Showering was then performed with Pythia 8.230 [134] and the A14 parameter set is used for tuning the shower. The NNPDF3.1NLO [116] parton distribution function (PDF) set enters in the matrix element calculation and the NNPDF2.3LO [135] is used in the parton shower. AF2 is used for the detector simulation.

An existing MadGraph5 aMC@NLO Signal generation configuration existed from [61]. I updated the steering code and parameters, following suggestions from theorists, and performed the validation necessary to generate the samples within the ATLAS central production system.

Signal samples were generated for a number of different W_R–N_R mass hypotheses, in both the resolved and boosted channels, covering a range in m(W_R) from 500 GeV to 7 TeV and for m(N_R) values from 1 GeV to 5.5 TeV. The range of mass points and cross-section can be seen in figure 6.2. The generated samples with their cross-sections are listed in Table 6.3. Examples distributions for the invariant masses of the two W_R bosons and the N_R are shown in figure 6.3 for a couple of signal samples.

The simulated events contain a Majorana N_R, resulting in a 50% admixture of same-sign and opposite-sign lepton pairs. This enables studies in both the opposite-sign and same-sign channels. In the case of a Dirac N_R, only opposite-sign leptons would be produced, and so the measured cross-section could be double of that simulated. Assuming that the cross section for N_R production would be unchanged between the Majorana/Dirac cases, no other changes are expected. The signal samples do not include lepton flavour-mixing, although this is a free parameter of the model and could be studied in future.

DSID	Name	Total x-sec [pb]
508433	MGPy8EG_lrsm_WR1000_NR1200	0.00832
508434	MGPy8EG_lrsm_WR1000_NR1600	0.0011436
508435	MGPy8EG_lrsm_WR1000_NR2000	0.00023473
508436	MGPy8EG_lrsm_WR1200_NR1500	0.0024964
508437	MGPy8EG_lrsm_WR1200_NR2000	0.00029389
508438	MGPy8EG_lrsm_WR1200_NR2500	5.1253e-05
508439	MGPy8EG_lrsm_WR1500_NR1500	0.0071021
508440	MGPy8EG_lrsm_WR1500_NR2000	0.00043209
508441	MGPy8EG_lrsm_WR1500_NR2500	6.8282e-05
508442	MGPy8EG_lrsm_WR2000_NR1500	0.096704
508443	MGPy8EG_lrsm_WR2000_NR2000	0.0014617
508444	MGPy8EG_lrsm_WR2000_NR2500	0.00011756
508445	MGPy8EG_lrsm_WR2000_NR3500	5.3332e-06
508446	MGPy8EG_lrsm_WR2400_NR1900	0.026065
508447	MGPy8EG_lrsm_WR2500_NR2500	0.00036035
508448	MGPy8EG_lrsm_WR2500_NR3000	3.5083e-05
508449	MGPy8EG_lrsm_WR2500_NR3500	8.0393e-06
508450	MGPy8EG_lrsm_WR2600_NR1000	0.060615
508451	MGPy8EG_lrsm_WR3000_NR1000	0.025605
508452	MGPy8EG_lrsm_WR3000_NR2500	0.0043409
508453	MGPy8EG_lrsm_WR3000_NR3000	9.9581e-05
508454	MGPy8EG_lrsm_WR3000_NR3500	1.149e-05
508455	MGPy8EG_lrsm_WR3000_NR4000	3.2136e-06
508456	MGPy8EG_lrsm_WR3000_NR4500	9.9566e-07
508457	MGPy8EG_lrsm_WR3000_NR50	0.034273
508458	MGPy8EG_lrsm_WR3500_NR1500	0.0075085
508459	MGPy8EG_lrsm_WR3500_NR2500	0.0032685
508460	MGPy8EG_lrsm_WR3500_NR3000	0.0010979
508461	MGPy8EG_lrsm_WR3500_NR3500	3.0631e-05
508462	MGPy8EG_lrsm_WR3500_NR4000	4.155e-06
508463	MGPy8EG_lrsm_WR3500_NR4500	1.381e-06
508464	MGPy8EG_lrsm_WR4000_NR1000	0.0035236
508465	MGPy8EG_lrsm_WR4000_NR2500	0.0016763
508466	MGPy8EG_lrsm_WR4000_NR3500	0.00031022
508467	MGPy8EG_lrsm_WR4000_NR4000	1.0623e-05
508468	MGPy8EG_lrsm_WR4000_NR400	0.0043755
508469	MGPy8EG_lrsm_WR4000_NR4500	1.6436e-06
508470	MGPy8EG_lrsm_WR4000_NR50	0.0052091
508471	MGPy8EG_lrsm_WR4500_NR1500	0.001256
508472	MGPy8EG_lrsm_WR4500_NR2500	0.00080833
508473	MGPy8EG_lrsm_WR4500_NR3500	0.00031248
508474	MGPy8EG_lrsm_WR4500_NR4000	9.9299e-05
508475	MGPy8EG_lrsm_WR4500_NR4500	4.1077e-06
508476	MGPy8EG_lrsm_WR4500_NR450	0.0018933
508477	MGPy8EG_lrsm_WR5000_NR1000	0.00070661
508478	MGPy8EG_lrsm_WR5000_NR2000	0.00049145
508479	MGPy8EG_lrsm_WR5000_NR3000	0.00030824
508480	MGPy8EG_lrsm_WR5000_NR3500	0.00021049
508481	MGPy8EG_lrsm_WR5000_NR4000	0.00011437
508482	MGPy8EG_lrsm_WR5000_NR500	0.00090979
508483	MGPy8EG_lrsm_WR5000_NR50	0.0012903
508484	MGPy8EG_lrsm_WR5500_NR1000	0.00036513
508485	MGPy8EG_lrsm_WR5500_NR2000	0.0002486
508486	MGPy8EG_lrsm_WR5500_NR3000	0.00016952
508487	MGPy8EG_lrsm_WR5500_NR3500	0.00012884
508488	MGPy8EG_lrsm_WR5500_NR4000	8.6548e-05
508489	MGPy8EG_lrsm_WR5500_NR550	0.00047701
508490	MGPy8EG_lrsm_WR6000_NR1000	0.00020109
508491	MGPy8EG_lrsm_WR6000_NR2000	0.00013144
508492	MGPy8EG_lrsm_WR6000_NR3000	9.3475e-05
508493	MGPy8EG_lrsm_WR6000_NR3500	7.5521e-05
508494	MGPy8EG_lrsm_WR6000_NR4000	5.6639e-05
508495	MGPy8EG_lrsm_WR6000_NR600	0.00026502
508496	MGPy8EG_lrsm_WR600_NR1500	0.0010707
508497	MGPy8EG_lrsm_WR600_NR2000	0.00017743
508498	MGPy8EG_lrsm_WR600_NR2500	4.2049e-05
508499	MGPy8EG_lrsm_WR6500_NR1000	0.00011537
508500	MGPy8EG_lrsm_WR6500_NR2000	7.0698e-05
508501	MGPy8EG_lrsm_WR6500_NR3000	5.1083e-05
508502	MGPy8EG_lrsm_WR6500_NR650	0.00015285
508991	MGPy8EG_lrsm_WR3000_NR10	0.034606
508992	MGPy8EG_lrsm_WR3000_NR1	0.023205
508993	MGPy8EG_lrsm_WR3000_NR300	0.031982
508994	MGPy8EG_lrsm_WR3500_NR1	0.0085612
508995	MGPy8EG_lrsm_WR4000_NR100	0.0050664
508996	MGPy8EG_lrsm_WR4000_NR10	0.0053042
508997	MGPy8EG_lrsm_WR4500_NR1	0.0016778
508998	MGPy8EG_lrsm_WR5000_NR100	0.0012377
508999	MGPy8EG_lrsm_WR5000_NR10	0.0013276

(continues)

509000	MGPy8EG_lrsm_WR5000_NR400	0.00097048
509001	MGPy8EG_lrsm_WR5500_NR1	0.00052208
509002	MGPy8EG_lrsm_WR5500_NR200	0.00064363
509003	MGPy8EG_lrsm_WR5500_NR300	0.00058405
509004	MGPy8EG_lrsm_WR5500_NR400	0.00053517
509005	MGPy8EG_lrsm_WR5500_NR50	0.00075114
509006	MGPy8EG_lrsm_WR6000_NR100	0.00044106
509007	MGPy8EG_lrsm_WR6000_NR10	0.00048477
509008	MGPy8EG_lrsm_WR6000_NR200	0.00039189
509009	MGPy8EG_lrsm_WR6000_NR400	0.00031648
509010	MGPy8EG_lrsm_WR6000_NR50	0.00046681
509011	MGPy8EG_lrsm_WR6500_NR100	0.00028672
509012	MGPy8EG_lrsm_WR6500_NR1	0.00021417
509013	MGPy8EG_lrsm_WR6500_NR300	0.00022125
509014	MGPy8EG_lrsm_WR6500_NR500	0.00017689
509015	MGPy8EG_lrsm_WR7000_NR100	0.00019409
509016	MGPy8EG_lrsm_WR7000_NR10	0.00021783
509017	MGPy8EG_lrsm_WR7000_NR200	0.00016809
509018	MGPy8EG_lrsm_WR7000_NR400	0.00012787
509019	MGPy8EG_lrsm_WR7000_NR50	0.00020863
509148	MGPy8EG_lrsm_WR1000_NR1000	0.047607
509149	MGPy8EG_lrsm_WR1000_NR1500	0.0017864
509150	MGPy8EG_lrsm_WR1000_NR500	5.584
509151	MGPy8EG_lrsm_WR1500_NR1000	0.60608
509152	MGPy8EG_lrsm_WR1500_NR500	1.2146
509153	MGPy8EG_lrsm_WR2000_NR1000	0.22784
509154	MGPy8EG_lrsm_WR2000_NR500	0.31496
509155	MGPy8EG_lrsm_WR2500_NR1000	0.075512
509156	MGPy8EG_lrsm_WR2500_NR1500	0.050156
509157	MGPy8EG_lrsm_WR2500_NR2000	0.019103
509158	MGPy8EG_lrsm_WR2500_NR500	0.093115
509159	MGPy8EG_lrsm_WR3000_NR1500	0.019742
509160	MGPy8EG_lrsm_WR3000_NR2000	0.012249
509161	MGPy8EG_lrsm_WR3000_NR5000	3.3544e-07
509162	MGPy8EG_lrsm_WR3000_NR500	0.030228
509163	MGPy8EG_lrsm_WR3000_NR5500	1.1736e-07
509164	MGPy8EG_lrsm_WR3500_NR1000	0.009156
509165	MGPy8EG_lrsm_WR3500_NR2000	0.0055281
509166	MGPy8EG_lrsm_WR3500_NR5000	4.6169e-07
509167	MGPy8EG_lrsm_WR3500_NR500	0.010734
509168	MGPy8EG_lrsm_WR3500_NR5500	1.5799e-07
509169	MGPy8EG_lrsm_WR4000_NR1500	0.0029543
509170	MGPy8EG_lrsm_WR4000_NR2000	0.002355
509171	MGPy8EG_lrsm_WR4000_NR3000	0.00095487
509172	MGPy8EG_lrsm_WR4000_NR5000	6.156e-07
509173	MGPy8EG_lrsm_WR4000_NR500	0.0042019
509174	MGPy8EG_lrsm_WR4000_NR5500	2.1346e-07
509175	MGPy8EG_lrsm_WR4500_NR1000	0.0014963
509176	MGPy8EG_lrsm_WR4500_NR2000	0.001038
509177	MGPy8EG_lrsm_WR4500_NR3000	0.00056266
509178	MGPy8EG_lrsm_WR4500_NR5000	6.8975e-07
509179	MGPy8EG_lrsm_WR4500_NR500	0.0018465
509180	MGPy8EG_lrsm_WR4500_NR5500	2.7486e-07
509181	MGPy8EG_lrsm_WR5000_NR1500	0.00058556
509182	MGPy8EG_lrsm_WR5000_NR2500	0.0004013
509183	MGPy8EG_lrsm_WR5000_NR4500	3.58e-05
509184	MGPy8EG_lrsm_WR5000_NR5000	1.7414e-06
509185	MGPy8EG_lrsm_WR5000_NR5500	2.9875e-07
509186	MGPy8EG_lrsm_WR500_NR1000	0.0094901
509187	MGPy8EG_lrsm_WR500_NR500	0.71778
509188	MGPy8EG_lrsm_WR5500_NR1500	0.00029573
509189	MGPy8EG_lrsm_WR5500_NR2500	0.00020881
509190	MGPy8EG_lrsm_WR5500_NR4500	4.613e-05
509191	MGPy8EG_lrsm_WR5500_NR5000	1.428e-05
509192	MGPy8EG_lrsm_WR5500_NR5500	7.7184e-07
509193	MGPy8EG_lrsm_WR6000_NR1500	0.00015783
509194	MGPy8EG_lrsm_WR6000_NR2500	0.00011146
509195	MGPy8EG_lrsm_WR6000_NR4500	3.7509e-05
509196	MGPy8EG_lrsm_WR6000_NR5000	1.9627e-05
509197	MGPy8EG_lrsm_WR6000_NR5500	6.0153e-06
509198	MGPy8EG_lrsm_WR6500_NR1500	8.6656e-05
509199	MGPy8EG_lrsm_WR6500_NR2500	5.9866e-05
509200	MGPy8EG_lrsm_WR6500_NR3500	4.2652e-05
509201	MGPy8EG_lrsm_WR6500_NR4000	3.4067e-05
509202	MGPy8EG_lrsm_WR6500_NR4500	2.5246e-05
509203	MGPy8EG_lrsm_WR6500_NR5000	1.643e-05
509204	MGPy8EG_lrsm_WR6500_NR5500	8.4719e-06

Table 6.3: Signal samples used in the analysis with their corresponding Dataset IDs (DSIDs) and cross-section.

Chapter 7

Physics objects & Event selection

7.1 Physics objects

The reconstructed, experimental proxies for the particles created in the pp collisions within the ATLAS detector are called physics object candidates. Reconstructing them from detector-level information is a necessary ingredient to search for new physics, like the experimental proof of the KS process that this thesis deals with. The physics objects of interest in this analysis are electrons, muons, and jets. The reconstruction, calibration, and identification of these objects in the ATLAS experiment are covered in this chapter.

7.1.1 Vertex and Track Reconstruction

Tracks: The Inner Detector has the ability to identify tracks, the experimental signature for paths followed by charged particles, by extrapolating from a minimum number of hits either inwards from the TRT or outwards in the Pixel and SCT detectors. If hits in multiple layers of the ID are sufficiently consistent with the projected track, they are incorporated as part of the extrapolation, in an iterative fitting method. The number of tracks originating from instrumental effects is decreased by rejecting a track if an anticipated hit in a layer is absent and by requiring hits in the innermost layers, closer to the beampipe. More information may be found in [136, 137].

Vertices: Vertex are locations where points where multiple particles originate, suggesting an interaction. They are determined by iteratively fitting to tracks with coincident origins within a certain tolerance. A candidate vertex is rebuilt after tracks from the fit that are incompatible with it are discarded; the discarded tracks then become seeds for additional vertices. The significant p_{T} of their associated tracks helps to determine primary vertices, the locations of the hard scatter interactions. Secondary vertices can be produced by particles with non-zero lifetimes that propagate from the primary vertex, the underlying event, pile-up, and other causes. In [136, 138], further details on vertex-finding in ATLAS may be found.

Per the recommendations of the ATLAS ID Group [139], each event considered in the analysis must have a primary vertex. The vertex with the largest $\sum {P_T}^2$ of assigned tracks is identified as the primary vertex.

7.1.2 Electrons

The basic definitions of electrons in different "working points" are provided centrally by the ATLAS EGamma group [140] and are common to all ATLAS analyses. These basic definitions are based on three categories: electron reconstruction, identification, and isolation. Different analyses choose one of these working points to use and complement it with further suitable kinematic selections.

An electron can lose a considerable amount of energy while traversing through the detector due to bremsstrahlung. The photon that was radiated may be converted into an electron-positron pair that also interacts with the detector material. The electromagnetic showers detected in the calorimeter are the main result of these processes. Secondary particles generated are often highly collimated with the initial particle track and are reconstructed as part of the same electromagnetic cluster. But similar interactions may also take place in the inner detector or the beam pipe, leading to several tracks coming from the same electron [141, 142].

The total energy in each calorimeter tower, beginning from the beampipe, is added to determine the energy deposits in each tower. Using towers with large energy deposits as a starting point, the towers are classified into clusters that seem to have originated from the same meteor shower. A cluster is regarded as an electron candidate if it can be linked to a high-quality track; otherwise, it is regarded as a photon candidate.

The energy and position of the electron are determined by the cluster and track characteristics. To account for energy loss as the electron travels through the detector, the energy should be adjusted. This is accomplished by comparing the electron and cluster energies in simulations and at a particular location in the data and MC.

To improve the efficacy of the chosen electron objects, additional criteria known as "identification selections" are employed. Prompt isolated electrons can be distinguished based on a likelihood discriminant that can distinguish between prompt isolated electrons and energy deposits from hadronic jets, converted photons, and actual electrons created in the decays of heavy-flavour hadrons. These inputs to the discriminant include the primary electron track's parameters, the lateral and longitudinal evolution of the electromagnetic shower in the EM calorimeter, and the primary electron track's spatial compatibility with the reconstructed cluster. There are three distinct identification levels, called `Loose`, `Medium`, and `Tight`, from higher to lower signal efficiency, and lower to lower background rejection, respectively.

In some cases, it may not be possible to distinguish pure electrons using only identification criteria. In datasets with a significant pile-up, additional isolation criteria may be used to more effectively choose prompt leptons. Different working points are defined based on different upper bounds on the calorimeter-based and track-based isolation requirements. The `Tight` working point has the strictest isolation requirements, requiring a smaller isolation cone and a higher track and calorimeter isolation threshold. A stricter requirement for shower shape is also applied. The `Loose` working point, on the other hand, typically has less stringent isolation requirements, allowing for a wider isolation cone and a lower track and calorimeter isolation threshold, resulting in increased electron identification efficiency but also a higher background rejection.

7.1.3 Muons

Information from multiple subdetectors, such as the ID, MS, and the calorimeters at $\eta = 0$ (where the coverage of the MS is limited), is utilised to reconstruct muon candidates. Data from the drift circles in the MDTs (Drift Tubes) and energy deposits in the CSCs (Cathode Strip Chambers) are employed to reconstruct the tracks in the MS. Following the extrapolation of these tracks to the ID and vice versa, a new track is fitted to create "combined" muon candidates. In addition, tracks in the MS that can be extrapolated to the primary vertex but do not have a well-reconstructed Inner Detector track or originate from beyond the acceptance of the ID are tagged as "extrapolated" muon candidates. Muon candidates exhibiting "segment-tagged" tracks have good tracks in certain sections of the MS and an energy deposit suggesting that the muon did not escape the subdetector, which may be extrapolated to an ID track. Finally, if an ID track of a muon candidate matches a calorimeter cluster that denotes a minimally ionising particle, they are classified as "calorimeter-tagged".

Muons may be classified as `Loose`, `Medium`, or `Tight`. The various types of muons outlined in the previous paragraph fall under distinct identification categories. Additional criteria include a minimum required hit count across subdetectors and requirements on the compatibility of track segments [143]. "`FixedCutTightTrackOnly`" is a specific isolation requirement based on the track isolation variable, where the isolation is calculated by summing the transverse momentum of all tracks in a cone around the muon candidate, excluding the muon candidate's track. The cut applied is a fixed one, and it is typically very tight. This working point is designed to identify muons with high p_{T} and low background, but the isolation efficiency may be lower than other working points.

Muon momentum calibration factors are determined through comparisons of data and simulated events to account for differences in muon momentum and reconstructed efficiency differences between data and simulation [143].

7.1.4 Jets

The "particle flow" algorithm, a technique used to identify individual particles and to reconstruct the properties of hadronic jets produced in high-energy collisions has been employed [144]. It combines information from different types of particle detectors to distinguish between different types of particles and to determine their energy and direction.

The process starts by choosing well-reconstructed tracks and creating calorimeter topo-clusters, groups of energy deposits that are likely to have been produced by a single particle. The energy deposited in the calorimeter is then determined using the cluster location and track momentum, after each track is matched to a single topo-cluster, if that is feasible. In instances where a particle can deposit energy in several topo-clusters, a probability is assigned to each track-cluster pair that the particle's energy estimate is incomplete. Approximately 10% of the time a particle is matched to numerous clusters with comparable probabilities. The expected energy that the particle associated with the track should have deposited in the calorimeter is then subtracted cell by cell from the topo-clusters that are within a $\Delta R = 0.2$ radius of the track point. The remaining clusters should be compatible with the anticipated shower fluctuations of a single particle's signal, as predicted from a single pion sample, and are removed.

The jet-forming anti-k_t algorithm [145], a clustering method used to identify jets produced in high-energy collisions based on their proximity in the detector, with a radius value of

0.4 and the FASTJET [146] software package were used to reconstruct the particle flow jets. Only positive energy topo-clusters that survived the energy subtraction phase are used as input. The jets are then calibrated based on an exact process described in reference [147]. In short, to reduce pile-up contamination, an area-based correction is employed, and a correction based on the primary vertices is applied to the jet p_T. To match the simulated particle-level energy scale, the jet energy scale is likewise adjusted. Finally, using precisely measured reference objects (such as photons and Z bosons), an extra calibration is performed to adjust the energy of the jets.

B-tagging [148] is a technique that allows jets to be classified as either b-jets, c-jets, or light-flavour jets depending on the type of hadrons they comprise. The identification of b-jets relies on the properties of the b-hadrons, which have large mass, long lifetime and high decay multiplicity. ATLAS has developed many b-tagging techniques to do this [149]. To identify (and veto) b-jets in particle jets, this analysis makes use of the machine learning based DL1r b-tagging algorithm. The method determines whether or not the jet is a b-jet based on a probability analysis of its features, including tracks and secondary vertex information. The technique outputs a continuous value called the b-tagging score; higher values indicate a greater probability that the jet is a b-jet.

7.2 Event selection

In section 7.1, the approach for reconstructing and calibrating the physics objects, essential to this analysis, was presented. This section describes the analysis-specific conditions that are employed, to create a signal-enhanced search region. The combination of these criteria, for example on the kinematics of the physics objects, is referred to as "event selection"; It applies to both recorded and MC simulated datasets, and determines to a very large degree the sensitivity of the analysis.

7.2.1 Electrons

Electron candidates are required to have $|\eta| < 2.47$ [150]. The ones in the crack region of the EM calorimeter ($1.37 < |\eta| < 1.52$) are discarded. In addition, electrons must have $p_T > 25$ GeV because low energy electrons are not of interest in this analysis, as the search targets high mass W_R and N_R. They should satisfy the Tight identification since it allows us to identify electrons with good efficiency and a low rate of misidentification. Finally, they should satisfy the Loose isolation criteria.

7.2.2 Muons

Muon candidates are required to have $|\eta| < 2.5$ to ensure that they are within the acceptance of the ID and MS. They must also have $p_{\mathrm{T}} > 25$ GeV because (as with electrons) low-energy muons are not of interest in this analysis. In addition, they should satisfy the `Medium` identification working point. For muons with $p_{\mathrm{T}} > 300$ GeV, the `High-`p_{T} working point requirements must be met. Finally, muons should satisfy the `FixedCutTightTrackOnly` working point, which requires the sum of the transverse momenta of all tracks within the specified cone to be below a certain threshold, determined by the fixed cut value.

Apart from the baseline leptons described above, leptons with modified requirements are defined for control samples for the estimation of the misidentified fake lepton backgrounds. For example, the isolation requirement is inverted and the `Loose` identification is employed.

		Baseline	**Fake estimation**
Electrons	p_{T} (GeV)	> 25	
	$\|\eta\|$	(0, 1.37] or [1.52, 2.47]	
	Quality	Tight	Loose
	Isolation	Loose	Fail Loose or Tight
Muons	p_{T} (GeV)	> 25	
	$\|\eta\|$	< 2.5	
	Quality	High-p_{T} if $p_{\mathrm{T}} > 300$ GeV else Medium	
	Isolation	FixedCutTightTrackOnly	fail FixedCutTightTrackOnly
Jets	p_{T} (GeV)	> 20	
	$\|\eta\|$	< 2.5	

Table 7.1: Definitions of the electrons, muons and jets used in the analysis.

7.2.3 Jets

Jets with $p_{\mathrm{T}} > 20$ GeV and $|\eta| < 2.5$ are selected in this analysis since they have been found to have the best search sensitivity for large regions of the phase space of interest. Jets that have $p_{\mathrm{T}} < 60$ GeV and $|\eta| < 2.4$ from pile-up interactions are suppressed using a jet-vertex tagging (JVT) discriminant [151].

Furthermore, events are rejected if they contain jets that are identified as b-jets with the `DL1r` algorithm [149, 152]. A working point to achieve 77% efficiency for b-jets is employed.

7.2.4 Overlap removal

To avoid cases where the detector response to a single physical object is reconstructed as two different final-state physics objects, e.g. an electron reconstructed as both an electron and a jet, several steps are followed, as summarised in Table 7.2.

Order	Object discarded	Object kept	Matching condition
1.	Electron	Electron	If two electrons share a track, discard the softer electron
2.	Muon	Electron	If they share a track and the muon leaves a sufficiently high energy deposit in the calorimeter
3.	Electron	Muon	If they share a track with the remaining muon
4.	Jet	Electron	$\Delta R < 0.2$, jet is not b-tagged and $p_{\mathrm{T}}(e) > 100$ GeV
5.	Electron	Small-R jet	$\Delta R < 0.4$
6.	Jet	Muon	$\Delta R < 0.2$, # of tracks associated to the jet < 3, $p_{\mathrm{T}}(\mu)/p_{\mathrm{T}}(j) > 0.5$ and $p_{\mathrm{T}}(\mu)/\sum p_{\mathrm{T}}(trk) > 0.7$
7.	Muon	Small-R jet	$\Delta R < 0.4$

Table 7.2: The order of overlap removal used in this analysis. ΔR is defined as $\Delta R^2 = \Delta y^2 + \Delta\phi^2$, where Δy and $\Delta\phi$ are the rapidity and azimuthal-angle differences between two objects. The variables $p_{\mathrm{T}}(e)$, $p_{\mathrm{T}}(\mu)$, $p_{\mathrm{T}}(j)$ and $p_{\mathrm{T}}(trk)$ are the transverse momenta of the corresponding electron, muon, jets, and all tracks associated with the jet.

Chapter 8

Background estimation

The background processes considered in this analysis are modelled with MC, as discussed in Section 6.2. Signal-free Control regions are defined with the aim of verifying the modelling of background processes, and deriving data-driven normalisation factors to correct for any differences between data and MC. Normalisation factors are extracted from the control regions by comparing the number of expected background events to the observed number of events in the data. The selection strategy of the analysis regions can be seen in section 8.1. Table 8.2 shows the cut-flow for a selection of signal samples. Figure 8.1 shows the acceptance times efficiency for different Signal Regions.

While comparing the background MC to the data distributions in these CR, we encountered the following problem: The Sherpa 2.2.11 generator [111] - used to simulate the Z+jets background, does not correctly model the $m(jj)$ spectrum although most other observables are well-described. Therefore, we employ a data-driven re-weighting procedure, based on a dedicated Z+jets Reweighting Region (RR), which is applied on the inclusive Z process Sherpa samples to correct for this effect. Section 8.2 provides further details and describes the re-weighting procedure that corrects this mis-modelling.

The event selections used in the control, reweighting and validation (to verify the output of the fit) regions are summarised and compared to those used in the signal region in Table 8.1.

	Control Regions		Validation Regions	Signal Regions
Region	RR($\ell^{\pm}\ell^{\mp}$)	CR($\ell^{\pm}\ell'^{\mp}$)	VR($\ell^{\pm}\ell^{\mp}$)	SR($\ell^{\pm}\ell^{\mp}$)
$m_{\ell\ell}$ [GeV]	[60, 110]	> 400	[110, 400]	> 400
H_T [GeV]	> 400	> 400	> 400	> 400
m_{jj} [GeV]	> 110	> 110	> 110	> 110
Jet p_T [GeV]	>100	>100	>100	> 100
b-jet veto	✓	✓	✓	✓

Table 8.1: Summary of all regions defined in the analysis, indicating the event selection criteria used for a given region. The flavour combinations are summarised as follows: $\ell^{\pm}\ell^{\mp} = \{e^{\pm}e^{\mp}, \mu 6 \pm \mu^{\mp}\}, \ell^{\pm}\ell'^{\mp} = \{e^{\pm}\mu^{\mp}\}$. Pairs of values [X, Y] indicate the allowed region the quantity in question may take in the analysis.

8.1 Opposite-sign channel: Analysis Regions

The decision to use data to derive normalisation factors requires that only a negligible amount of signal is allowed to enter into the control regions. The background predictions for the background process are scaled according to the relevant derived normalisation factor, in all of the analysis regions.

The extraction and application of the normalisation factors occurs in a simultaneous fit of the signal and background MC to the data, which is the topic of Section 9 . Validation regions (VR) are also defined so that the effect of the normalisation factors could be verified before the signal region was unblinded.

The selections for the control, reweighting and validation regions are based on identical selections to those in the signal region, with the exception of a particular variable that is used to define orthogonal phase space regions. The variable used to ensure the orthogonality between the regions is $m_{\ell\ell}$, except for in the $e\mu$ CR which has the same kinematic selection as the signal regions, but requires different-flavour charged leptons. Distributions of key variables in the Control, Validation and Signal regions can be seen in Figures 9.4–9.17.

The Control, Reweighting, and Validation Regions are defined as follows:

- **Z+jets RR:** Leptonic Z-boson decays are excluded from the SR with a dilepton mass cut $m_{\ell^+\ell^-} > 400$ GeV. Consequently, the Z+jets RR is defined by 60 GeV< $m_{\ell^+\ell^-} <$ 110 GeVand is > 95% pure in Z+jets events. This RR does **not** enter the fit and is merely used to reweight and match the Z+jets background to data as described in Section 8.2. There is a single combined sample for this procedure, for both flavours.
- **Mixed flavour ($t\bar{t}$) CR:** A mixed flavour CR requiring an electron and a muon. The

composition of this CR is mostly top events, with a small admixture of diboson events. This CR is used to normalise the top background.

- **VR:** A complementary region, to test the analysis performance before unblinding in the range $110 < m_{\ell^+\ell^-} < 400$ GeV. The purity of Z in the validation region is around 50 % for both electron and muon channels. The remaining contributions are from diboson and top processes.

The main SM backgrounds in the signal regions are from top-quark events (mainly $t\bar{t}$) and Z+jets production, with contributions of $\sim$ 49% and $\sim$ 35% respectively in the ee SR and $\sim$ 55% and $\sim$ 37% in the $\mu\mu$ SR. Minor contributions arise from diboson (mainly $ZZ \to lljj$), with a contribution of $\sim$ 16% in the ee SR and $\sim$ 8% in the $\mu\mu$ SR. As these are the major backgrounds to the KS process, a normalisation factor is derived for the top-quark background and a reweighting factor is derived for the Z+jets background.

The $e\mu$ CR is dominated by top-quark events (80.2%), and thus a normalisation factor for top-quark processes is extracted from this region. The maximum amount of signal contamination is 6.7% in the $e\mu$ CR, though, as before, this is in a previously- excluded region and, for most signal hypotheses the control region is signal free.

Top-quark decays usually give rise to b-quarks, as already discussed, so an alternative control region, defined by requiring b-jet candidates, was considered. This control region would be $\approx$ 99% pure top-quark events but was rejected as the signal contamination was unacceptably high in comparison to the predicted background events, with signal events reaching a maximum of 74.2% of the total predicted events for m(W_R) – m(N_R) combinations with high cross sections.

8.2 Opposite-sign channel: Z+jets reweighting

The generator used to simulate the Z+jets background does not correctly model the m_{jj} spectrum, as shown in Figures 8.3 (a) and 8.4 (a), an effect that was also observed in the previous iteration of this analysis [61]. A reweighting factor is derived using events from the ee and $\mu\mu$ RR (combined) and applied to the simulated Z + jets events in all the analysis regions.

The reweighting factor for the Z+jets process is extracted from data in the combined ee + $\mu\mu$ Reweighting region, where the $60 \leq m_{\ell\ell} \leq 110$ GeV selection is defined to filter events with $m_{\ell\ell}$ around the Z boson mass, to enhance the proportion of Z + jets events in the

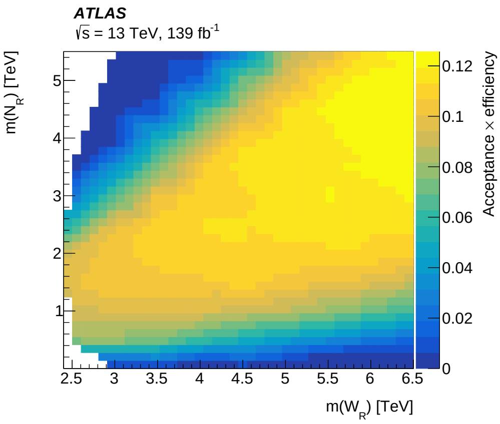

(a)

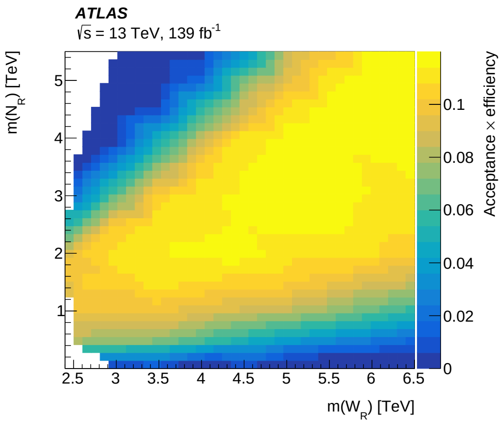

(b)

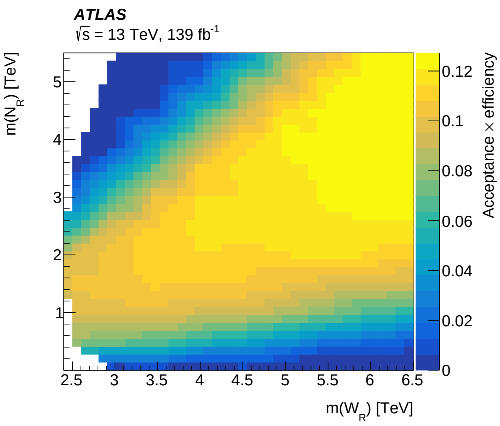

(c)

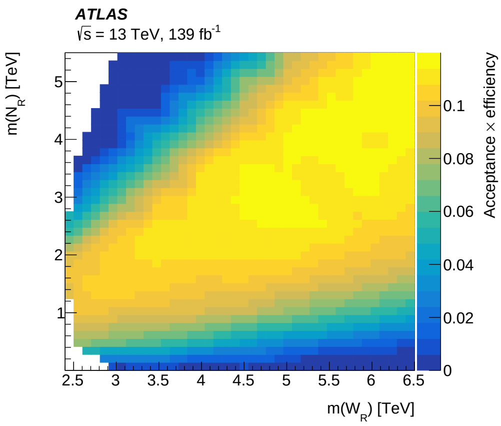

(d)

Figure 8.1: The acceptance times efficiency for electron OS SR (a), muon OS SR(b), electron SS SR (c) and muon SS SR.

	(5.5 TeV, 1.5 TeV)		(5.0 TeV, 3.0 TeV)		(4.0 TeV, 500 GeV)	
Generated	70000		70000		70000	
Derivation + tau veto	35356		36346		29807	
Number of jets >= 2	29696		33833		14928	
Number of leptons == 2	25837		32180		12148	
Triggers	25430		31643		12004	
Lepton identification == Tight	23908		29948		11161	
	ee	$\mu\mu$	ee	$\mu\mu$	ee	$\mu\mu$
Lepton flavour	11572	11897	14334	15197	5185	5524
Lepton charge	5877	5971	7167	7531	2607	2746
Dijet mass m_{jj} > 110 GeV	4352	4479	5575	5840	2062	2179
Jet p_{T} > 100 GeV	4296	4430	5531	5791	2023	2147
Number of b-tagged jets == 0	3639	3683	4308	4514	1876	1971
Dilepton mass $m_{\ell\ell}$ > 400 GeV	3603	3632	4212	4384	1867	1964

Table 8.2: Cut-flow table for a selection of Signal Region signal samples.

region.

The fraction of Z+jets events is above 95%. The maximum amount of signal contamination, namely the predicted signal events as a fraction of the total number of predicted events, is 4.2%. Most of the signal hypotheses considered do not enter either Control Region.

To correct the mismodelling, a Novosibirsk function (designed for this very purpose) is fitted to the data-to-MC ratio as a function of m_{jj}, after subtracting the simulated non-Z+jets background contributions from both. The Novosibirsk function [153] is defined as:

$$y = \exp\left[-\frac{0.5}{k_3^2}\, k_1^2 - 0.5\, k_3^2 \right] \tag{8.1a}$$

where

$$k_1 = \log\left[1.0 - \frac{(x - \mathrm{peak}) \cdot \mathrm{tail}}{width} \right], \tag{8.1b}$$

$$k_2 = 2\sqrt{\log 4}, \tag{8.1c}$$

and

$$k_3 = \frac{2.0}{k_2}\, \sinh^{-1}(0.5\, k_2 \cdot \mathrm{tail}) \tag{8.1d}$$

where the three free parameters width, peak and tail (typically found in literature as σ, x_0 and λ) control the shape of the distribution. The resulting ratio with the best fit reweighting function is shown in Figure 8.2. The reweighting factor ranges from 1.1 in the low-m_{jj} region to 0.8 in the high-m_{jj} region above 3 TeV.

The data-driven method followed to correct the mismodelling is:

1. Combine the m_{jj} histograms of the di-electron and di-muon channels created separately for data and each background sample in the Z+jets Reweighting Region. This is done since the mismodelling appears to be similar in the two channels.

2. Rebin the histograms ensuring that the distribution is populated with enough statistics for the expected integrated luminosity.

3. Subtract all background contributions from the data, except for Z+jets.

4. Normalise both data and Z+jets histograms.

5. Take the ratio of data over Z+jets. Normalise it.

6. Perform a χ^2 fit of the ratio with the Novosibirsk function with three parameters: peak, width, and tail. An additional normalisation factor is calculated from the normalisations of the previous steps.

7. Adjust the weight of each individual Z+jets event by the fitted function and the normalisation factor.

The reweighted m_{jj} distributions in the ee and $\mu\mu$ CRs are shown in Figures 8.3 and 8.4.

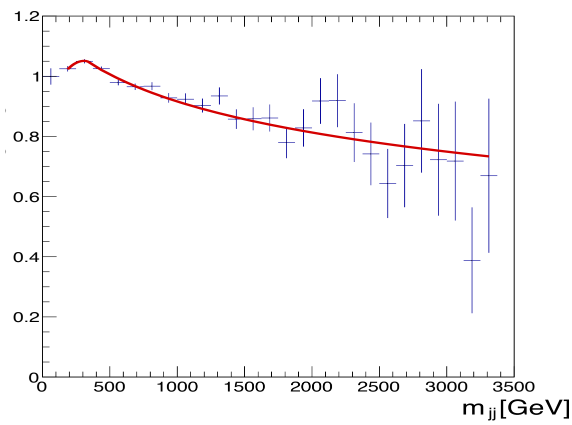

Figure 8.2: Ratio between data and simulation for Z + jet(s) events collected in RR($e \pm e \mp$) and RR($\mu \pm \mu \mp$) as a function of the dijet invariant mass, with the result of the Novosibirsk fit superimposed. The binning is adjusted to reduce statistical fluctuations.

Parameter	best fit value
peak	247.188 ± 14 TeV
width	5043 ± 33 TeV
tail	−36.6 ± 4.1

Table 8.3: The fitted values for the peak, width and tail for the modelling of the Z CR data-to-MC ratio with a Novosibirsk function. See text for details.

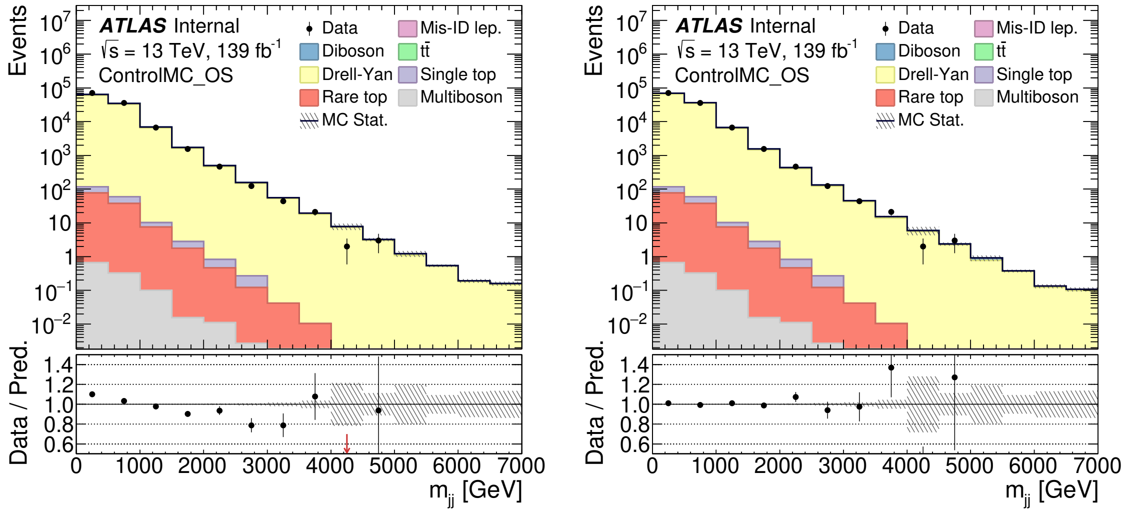

(a) (b)

Figure 8.3: m_{jj} distributions for the combined ee + $\mu\mu$ RR, (a) before and (b) after reweighting.

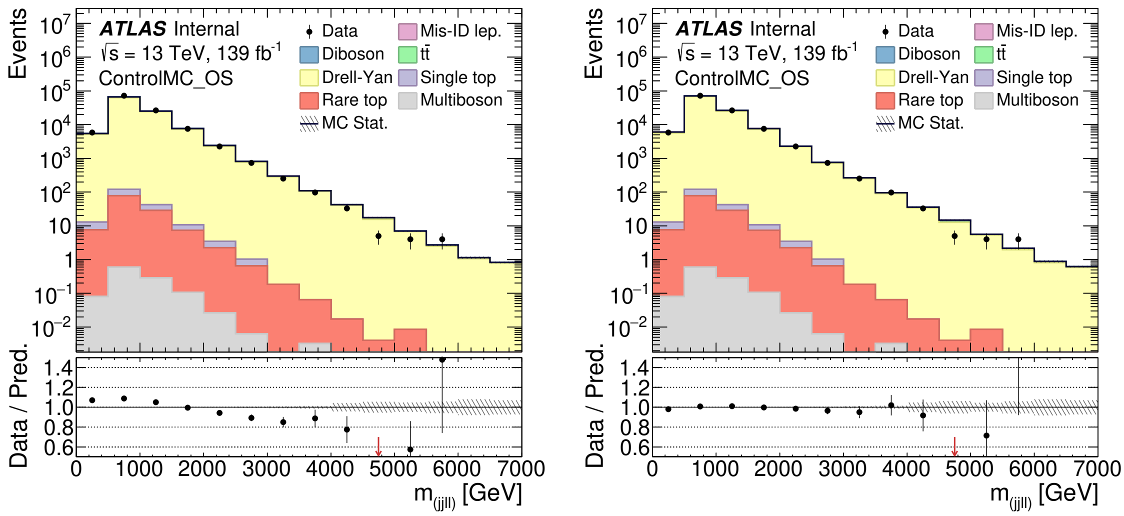

(a) (a) (b) (b)

Figure 8.4: m_{lljj} distributions for the combined ee + $\mu\mu$ RR, (a) before and (b) after reweighting.

8.3 Same-Sign channel: Overview

At this point, it is worth briefly discussing the resolved Same-Sign (SS) channel of the Heavy Neutrino analysis, before the combined OS and SS channels fit is presented in chapter 9.

I was not personally involved in the SS channel background estimation: my contribution was limited to deriving the ntuples and providing support on the use of the common analysis framework. Other parts of the analysis, for example, fakes and charge-flip estimation, were performed and validated by other team members.

The background processes that might result in a $\ell\ell jj$ ($\ell = e, \mu$) final state with same-sign leptons are diboson ($WW/ZZ/WZ \to \ell^{\pm}\ell^{\pm}jj$) and charge-flipped - Z+jets or $t\bar{t}$- events. Charge-flip occurs when the charge sign of one of the leptons is miss-measured; either with high-p_{T} leptons, whose curvature is hard to measure, or if an electron radiates a photon that then converts to an electron-positron pair.

Two CRs were defined, for SS ee and $\mu\mu$ flavours with scale factors for diboson and Z+jets processes. Three VRs were defined for SS ee, $\mu\mu$ and $e\mu$ flavours. Two SRs were defined, for SS ee and $\mu\mu$ flavours.

Unlike the resolved OS channel, the origin of $t\bar{t}$ and Z+jets events in the SS channel is charge-flip. Because of this, even though the channels were fitted simultaneously, those two samples were treated as two independent distributions in the OS and SS channels. In addition, no Z+jets reweighting was performed for the SS Z+jets. Regarding dibosons, the sample was further split into the following processes: WW/ZZ (mainly found in the OS channel) and WZ/ssWW (mainly found in the SS channel). The difference between WW and ssWW - aside from the relative charge of the final state leptons - is that they originate from different processes: WW indicates the process shown in figure 6.1c, while ssWW electroweak diboson processes with a final state of $\ell\ell\nu\nu jj$.

Due to the low statistics in the SS channel, it was found that H_T (the scalar p_{T} sum of the two most energetic jets and leptons) was better modelled in the MC distributions and was used as a discriminant variable.

Chapter 9

Statistical analysis

This chapter describes how the final results in the combined Opposite- and Same-Sign channels analysis were obtained ("OS" and "SS" respectively). The results themselves are presented in Chapter 10.

The statistical analysis package HistFitter [154], which is used extensively throughout the ATLAS collaboration, was used to implement a series of binned maximum-likelihood fits to the data distributions in the Control and Signal Regions, as described in Section 9.1. The procedure followed to obtain exclusion limits on possible W_R –N_R mass combinations, is described in Section 9.2.

I, in consultation with the rest of the small analysis team and their knowledge from the previous iteration of the analysis [61], decided on and implemented the fitting strategy, performed checks for significant deviations, and calculated the exclusion limits for the combined resolved OS and SS channels fit.

A similar fit was performed independently by the members of the boosted channel. The resolved and boosted channels were not combined statistically due to time constraints and the estimate that the sensitivity improvement was expected to be small.

9.1 Likelihood fits

A series of binned maximum-likelihood fits are used in this analysis: maximising the likelihood function to find the best-fit values for the model parameters. These free parameters include normalisation factors for the background processes and the signal normalisation parameter μ_S, which scales the signal prediction.

The fit further considers statistical and systematic uncertainties as nuisance parameters (NPs), which may change the shape and normalisation of both the signal and background predictions. The uncertainties, included in the fit as nuisance parameters, are described in Section 9.1.2. The free parameters in different Control and Signal Regions are fitted simultaneously; As a cross-check of the fitting procedure, the post-fit values of the free parameters were applied in the validation Regions, so that the compatibility between the data and the prediction can be verified.

Even though the OS and SS channels are being fitted together, they have different normalisation factors. For the Opposite-sign channel, there is a normalisation factor for the top-quark processes (the Z+jets samples were calibrated to data during the reweighting process described in section 8.2). For the Same-sign channel, there is a normalisation factor for the combined WZ/ssWW (diboson) processes and for the SS Z+jets. The fitting strategy can also be seen in table 9.1.

SM background yield	CR($e^\pm e^\mp$)	CR($e^\pm \mu^\mp$)	CR($\mu^\pm \mu^\mp$)	CR($e^\pm e^\pm$)	CR($\mu^\pm \mu^\pm$)
OS Z + jet(s) (obt. with re-weighting, not fit)	✓	—	✓	—	—
SS Z + jet(s)	—	—	—	✓	—
OS Top	—	✓	—	—	—
SS Diboson	—	—	—	✓	✓

Table 9.1: Regions used to obtain the background samples scale factors.

The fit inputs passed to HistFitter for the OS channel are histograms of m_{lljj} or m_{jj} distributions in each signal and Control Region, depending on whether we are considering a signal mass point in the m(W_R) > m(N_R) or m(W_R) < m(N_R) phase-space Region. For the SS channel, the fit inputs are histograms of H_T. The pre-fit distributions in Figures 9.4–9.17 are examples of input distributions used in the fit.

9.1.1 Likelihood function definition

The analysis makes use of the likelihood function [154], where boldface denotes a vector:

$$\mathcal{L}\left(\mu_{\mathrm{S}}, \boldsymbol{\mu}_{\mathbf{B}}, \boldsymbol{\theta}\right) =$$

$$\prod_{i}^{\text{bins}} \mathcal{P}\left(n_i \mid S_i\left(\mu_{\text{S}}, \boldsymbol{\theta}\right) + B_i\left(\boldsymbol{\mu}_{\mathbf{B}}, \boldsymbol{\theta}\right)\right) \tag{9.1a}$$

$$\times \prod_{j}^{\text{NPs}} \mathcal{F}_j\left(\tilde{\theta}_j \mid \theta_j\right) \tag{9.1b}$$

The first term (Eq. 9.1a) is a product - across all bins in the analysis Regions - of Poisson distributions $\mathcal{P}$ with the following form:

$$\mathcal{P}(n \mid \lambda) = \frac{e^{-\lambda}\lambda^n}{n!}$$

which, under the assumption of a combined signal and background prediction with an average event count λ, represents the likelihood of observing n events in data. Predicted signal and background yields, $S\left(\mu_{\text{S}}, \boldsymbol{\theta}\right)$ and $B\left(\boldsymbol{\mu}_{\mathbf{B}}, \boldsymbol{\theta}\right)$, are functions of θ, the set of nuisance parameters (NPs), and the signal strength and the set of background normalisation parameters, μ_S and μ_B.

The variable μ_S controls the predicted signal yield normalised to the original prediction:

- $\mu_S = 0$ gives the SM prediction (i.e. absence of new physics).
- $\mu_S = 1$ corresponds to the nominal theretical cross-section prediction and is thus consistent with the Majorana N_R hypothesis.
- $\mu_S = 2$ conforms to the Dirac N_R hypothesis. This is because, under the Dirac N_R hypothesis, the cross section multiplied by the branching fraction of the KS process to opposite sign leptons is twice that in the Majorana N_R scenario. The SS channel would see $\mu_S = 0$ in this case.

The μ_B includes $\mu_{\text{OS-Top}}$, $\mu_{\text{SS-diboson}}$ and $\mu_{\text{SS-Z+jets}}$, the OS top-quark, the SS diboson and the SS Z+jets (charge-flip) background normalisation factors, respectively, which scale individual background predictions. These normalisation factors are set during the fit so that the total background yield matches the observed data yield in the ee, $\mu\mu$ and $e\mu$ CRs.

The second term (Eq. 9.1b) is a product - over NPs - of auxiliary functions denoted by $\mathcal{F}$. These functions limit the value range of the nuisance parameters. Depending on the uncertainty that is taken into account, most NPs have auxiliary functions that follow a Poisson distribution, as described above, or a Gaussian distribution, as shown by:

$$\mathcal{G}(\tilde{\theta} \mid \theta, \sigma) = \frac{1}{\sqrt{2\pi\sigma^2}} e^{-\frac{(\tilde{\theta}-\theta)^2}{2\sigma^2}}$$

Before the fit, $\tilde{\theta}$ - the central value of each NP - is zero, and σ - the standard deviation - is one. This represents an assumption of "no previous knowledge".

The signal and background predictions are dependent on the NPs in the following ways:

$$S_i\left(\mu_{\mathrm{S}}, \boldsymbol{\theta}\right) = \mu_{\mathrm{S}} S_i^{\mathrm{nom}} \left(1 + \sum_j^{\mathrm{NPs}} \Delta_{ij}\left(\theta_j\right)\right)$$
$$B_i\left(\boldsymbol{\mu}_{\mathrm{B}}, \boldsymbol{\theta}\right) = \sum_b^{\mathrm{bkgs}} \mu_{\mathrm{B}_b} B_{bi}^{\mathrm{nom}} \left(1 + \sum_j^{\mathrm{NPs}} \Delta_{bij}\left(\theta_j\right)\right)$$

where S_i^{nom} is the nominal signal prediction in bin i and B_{bi}^{nom} is the nominal background prediction for background b in bin i. The response functions $\Delta_{ij}\left(\theta_j\right)$ and $\Delta_{bij}\left(\theta_j\right)$ describe how the amount of signal and background b in bin i varies due to systematic j, depending on the value of NP.

For each signal and background sample in a particular bin, the nominal and the $\pm 1\sigma$ variation for each systematic uncertainty yields are used in the fitting process. The changes in the yield for any value of θ are determined by using a polynomial interpolation between $\pm 1\sigma$ and exponential extrapolation beyond that range (see [155]).

9.1.2 Treatment of uncertainties

This section summarises the uncertainties considered in this analysis. Experimental systematic uncertainties are discussed in Section 9.1.2.1, whilst systematic uncertainties relating to MC predictions, referred to as theory uncertainties, are discussed in Section 9.1.2.2.

The effect of uncertainties on the m_{lljj}, m_{jj}, and H_T distributions are included in the fit as NPs, with response functions that may vary the overall and/or per-bin normalisation of the signal and backgrounds yields.

For any systematic uncertainties applied to the OS Top, SS diboson and SS Z+jets background processes, any contribution of the uncertainty on the total yield of the process is absorbed into the $\mu_{\mathrm{OS-Top}}$, $\mu_{\mathrm{SS-diboson}}$ and $\mu_{\mathrm{SS-Z+jets}}$ normalisation factors, respectively.

A summary of employed systematic uncertainties is presented in Table 9.2. All systematics are treated both as normalisation and as shape variations for all background samples that are not floating in the fit. For the OS-$t\bar{t}$, SS-Z+jets, SS-diboson backgrounds, and signal samples, the systematic uncertainties are only affecting the shape of the distributions. This is because their normalization is determined through the fitting process, which allows extraction of the signals of interest.

9.1.2.1 Experimental uncertainties

Differences between reconstruction techniques applied on data and simulated events are the primary way of measuring experimental uncertainties. Systematic uncertainties typically come in two forms: calibration and efficiency. Efficiency refers to the ability of a measurement or reconstruction technique to accurately identify or reconstruct an event or particle. To compensate for uncertainties in momentum scale and track reconstruction, calibration uncertainties vary particle momenta. Efficiency uncertainties are estimated by comparing the behaviour of reconstruction, object identification, charge identification, isolation, and trigger selection of leptons between data MC and varying the respective scale-factors. While data is excluded from the application of any sort of experimental uncertainties, they are applied to both background and signal MC predictions.

The uncertainty on the integrated luminosity is 1.7% [109]. It is obtained using the LUCID-2 detector [110] for the primary luminosity measurements. The uncertainty due to the pileup reweighting procedure is estimated by varying the amount of the pileup in the simulation to cover the uncertainty in the ratio of the predicted to measured inelastic cross section [156].

A set of experimental systematic uncertainties arises from the energy and momentum calibrations of leptons and jets, the lepton reconstruction, isolation and trigger efficiencies, and the jet vertex tagger and flavour-tagging efficiencies. The largest uncertainty in the total SM yield arises from the energy calibration and smearing of jets, derived in Ref. [157], and is between 10% and 15% depending on the signal Region under consideration. Uncertainties associated with lepton reconstruction, identification, isolation and trigger efficiencies, as well as energy or momentum calibration [150, 158–160] and b-jet tagging [152, 161], vary between 5% (OS) and 13% (SS) of the total SM yield.

Category	Type
Luminosity	`Lumi`
Pile-up modelling	`PileUp`
m_{jj} reweighting	one-sided
Experimental uncertainties	Electron scale and resolution
	Electron scale and resolution
	Electron reconstruction efficiencies
	Electron identification efficiencies
	Electron charge identification efficiencies
	Electron isolation efficiencies
	Electron trigger efficiencies
	Muon scale and resolution
	Muon reconstruction efficiencies
	Muon isolation efficiencies
	Muon track-to-vertex efficiencies
	Muon trigger efficiencies
	Jet energy scale — calibration
	Jet energy scale — flavour dependence
	Jet energy scale — pile-up dependence
	Jet energy scale — calo punch-through
	Jet energy scale — MC non-closure
	Jet energy resolution
	Jet JVT efficiencies
	Jet flavour tagging efficiencies
	missTuncertainties
Theory uncertainties	Sherpa 2.2.11 QCD scale
	Sherpa 2.2.11 PDF variation
	Sherpa 2.2.11 PDF choice
	$t\bar{t}$ QCD scale
	$t\bar{t}$ PDF variation
	$t\bar{t}$ PDF choice
	$t\bar{t}$ ISR
	$t\bar{t}$ FSR
	$t\bar{t}$ generator choice
	$t\bar{t}$ showering choice
	Sherpa 2.2 QCD scale
	Sherpa 2.2 PDF variation
	Sherpa 2.2 PDF choice
Data-driven background	Electron fake factors
	Muon fake factors

Table 9.2: Summary of the sources of systematic uncertainty considered in the analysis.

In the SS channel, the uncertainty related to the charge misidentification probability of electrons arises from the statistical uncertainty of the data and simulated samples of Z+jets events used in this measurement. The uncertainty is around 6.8% with a mild dependence on the electron E_{T} and η [162]. The uncertainty on the fake estimation arises from the limited knowledge of the composition of fakes, as well as from the statistical uncertainty and prompt lepton subtraction in the fake-enriched Regions. The uncertainty due to the composition of fakes is estimated by varying the nominal criteria defining the selection sample used in the fake-factor measurement [163]. The effect on the SM yields is 3.8% (electrons) and 0.8% (muons).

As described in Section 8.2, a fit has already been performed to give a data-driven correction to the modelling of backgrounds arising from Z boson decays with associated jets (m_{jj} reweighting). During the fit, the uncertainty on this procedure is estimated as the difference between the reweighted nominal Sherpa sample (to match the data in the Z+jets reweighting Region) and the data in the Z+jets validation Region. The uncertainty in the reweighting factor is found to vary between 0.4% and 0.8%, as a function of the dijet invariant mass. The systematic uncertainty can be seen in Fig. 9.1.

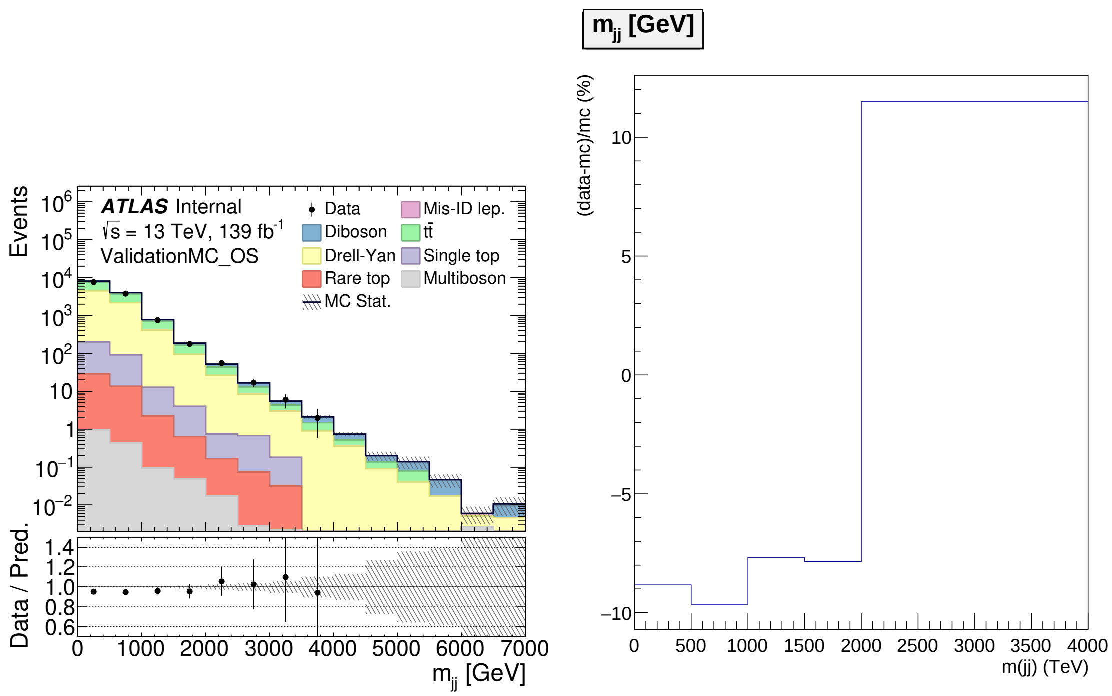

(a) (b)

Figure 9.1: (a): The data and reweighted background m_{jj} distribution in the combined ee and $\mu\mu$ VR, and (b): the difference in shape between data and reweighted background in the combined ee and $\mu\mu$ VR, used as the m_{jj} reweighting uncertainty.

9.1.2.2 Theoretical Uncertainties

Theoretical systematic uncertainties, related to the choice of theory parameters or the software used to generate MC datasets, are calculated by generating datasets with alternative theory parameter values or by employing different generative software and comparing these datasets to the nominal ones. Scale variation, PDF and α_s uncertainties are estimated for the signal samples and the main backgrounds, Z+jets, $t\bar{t}$ and diboson.

The effect of the choice of generator software used for the hard process and for showering is also estimated. Initial and final state variations are also considered for $t\bar{t}$. Additionally, the impact of the generator software choice for the hard process and showering is evaluated.

The theory uncertainties estimated for the Z+jets and diboson background processes include the choice of QCD renormalisation (μ_r) and factorisation (μ_f) scales, choice of the PDF set and α_S. The QCD scale uncertainty is estimated by varying μ_r and μ_f to half and twice their nominal values. The PDF uncertainty is estimated by using the envelope of the `NNPDF3.0` PDF set, as recommended in Ref. [164]. In addition, the `MMHT2014` [165] and `CT14NNLO` [166] PDF sets are used to estimate the uncertainty due to the PDF choice. Moreover, the uncertainty due to α_S is evaluated by varying its nominal value of 0.118 by ±0.001. The largest theory uncertainty generally originates from the QCD scales variations, and is between 10% and 20%, depending on the simulated process and the mass of the target signal.

The theory uncertainties associated with $t\bar{t}$ processes are as follows. The uncertainty from hard scatter generation is evaluated by comparing the `Powheg-Box` and `MG5_aMC@NLO` generators, both interfaced to the `Pythia8.186` parton shower model, as recommended in Ref. [164]. The uncertainty due to the hadronisation and fragmentation model is determined by comparing the nominal `Powheg-Box + Pythia8.186` generated sample with the one generated by `Powheg-Box` interfaced to `Herwig` [167] (version 7.0.1). The uncertainty related to the amount of initial- and final-state radiation is assessed by varying parton shower settings. The largest theory uncertainty generally originates from the amount of initial- and final-state radiation (ISR, FSR) and is between 0.4% – 0.5% and 0.6% of the $t\bar{t}$ process yield.

9.1.3 Fits

9.1.3.1 Background-only

To perform a check for significant data deviations from the expected background prediction, two combined OS and SS background-only fits, with the constraint that $\mu_S = 0$, were performed, one for each case of figure 1.3. For the SS channel, H_T was used as the discriminant variable across the whole phase-space, while for the OS channel one of the m_{lljj} or m_{jj}, depending on the mass hierarchy case. The VRs and SRs were not included in the background-only fits, however, post-fit distributions were produced, using the values of the fit parameters found during the fit. For the SRs this is done so as not to assume the absence of a signal, while for the VRs to cross-check the fit performance.

The resultant yields in the analysis Regions from these background-only fits are shown in Figure 9.2, and a breakdown of the uncertainty sources of the post-fit background yields in each analysis Region can be found in Figure 9.3. Pre- and post-fit distributions in the analysis Regions are shown in Figures 9.4–9.17. The lack of significant deviations in the data from the post-fit background prediction in the SRs indicates that the data is consistent with the background-only hypotheses.

Factor	Value
$\mu_{t\bar{t}}$	1.0 ± 0.1
$\mu_{WZ/ssWW}$	1.02 ± 0.15
$\mu_{DY(SS)}$	0.96 ± 0.3

(a) nominal hierarchy

Factor	Value
$\mu_{t\bar{t}}$	0.98 ± 0.1
$\mu_{WZ/ssWW}$	1.0 ± 0.15
$\mu_{DY(SS)}$	0.97 ± 0.3

(b) inverse hierarchy

Table 9.3: Normalisation factors for (a) the nominal hierarchy and (b) the inverse hierarchy case background-only fit

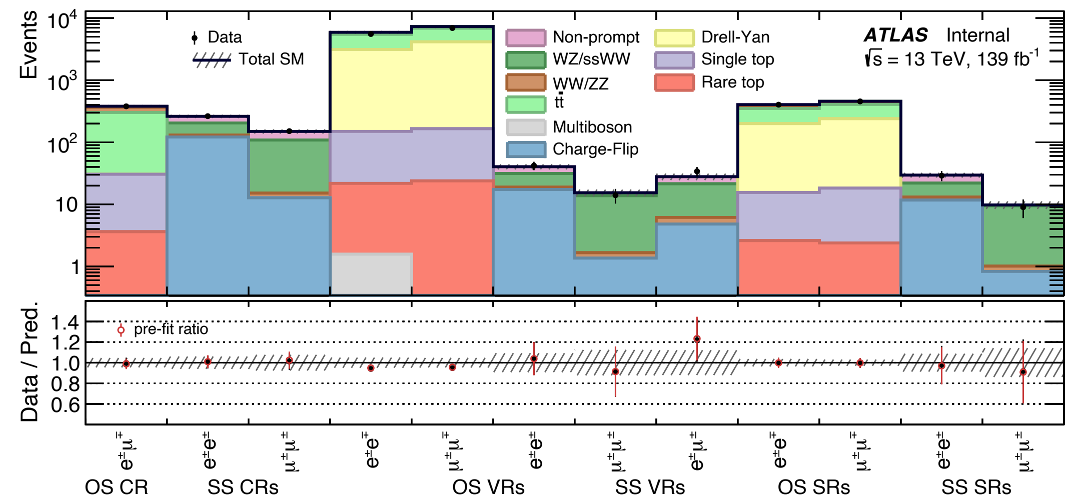

Figure 9.2: Pre- and post-fit background-only fit yields in all analysis Regions.

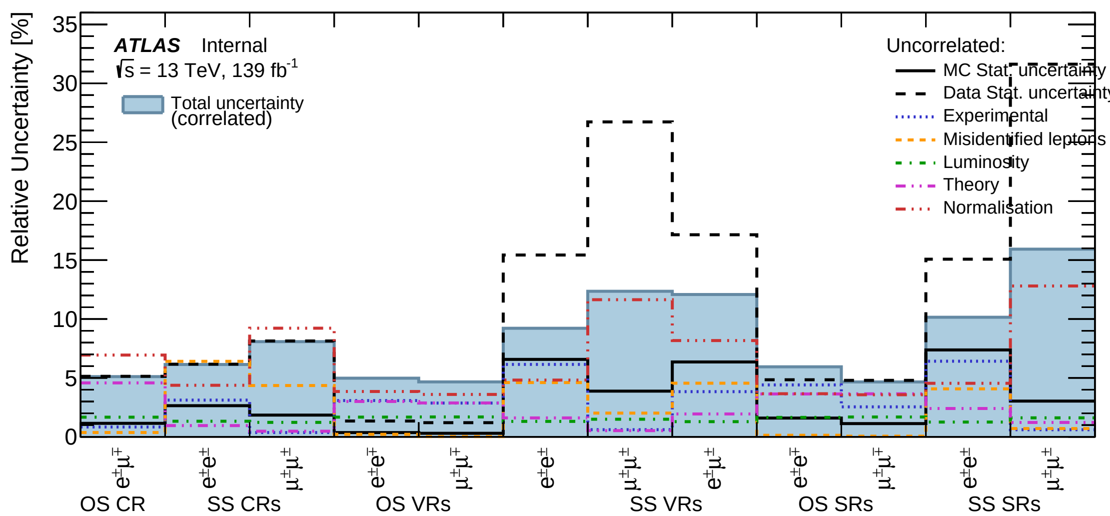

Figure 9.3: Relative uncertainties in the total background yield post-fit estimate. 'Theory' indicates the theoretical uncertainty in the simulated physics processes (e.g. cross-sections). 'Misidentified leptons' is the uncertainty associated with the model of the fake background. 'Normalisation' is the uncertainty on the fit yield of Z+jets, tt^{-} and diboson backgrounds. 'Experimental' corresponds to the combined uncertainty on physics objects efficiencies (such as trigger, identification or isolation) and uncertainties associated with missing E_T and pile-up. Individual uncertainties can be correlated with others, and do not necessarily add in quadrature towards the total background uncertainty.

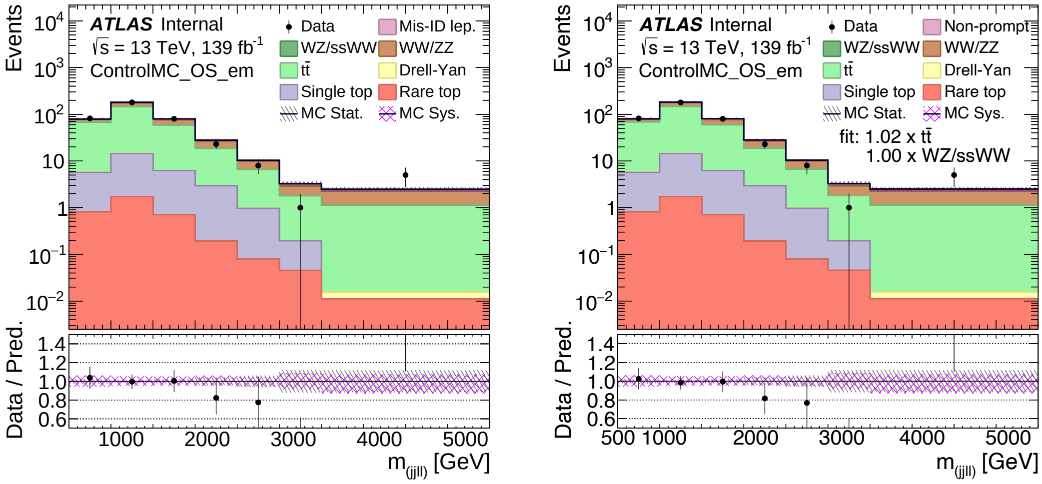

(a) (b)

Figure 9.4: Pre (a) and post (b) fit m_{jjll} distributions for the Top (OS $e\mu$) Control Region.

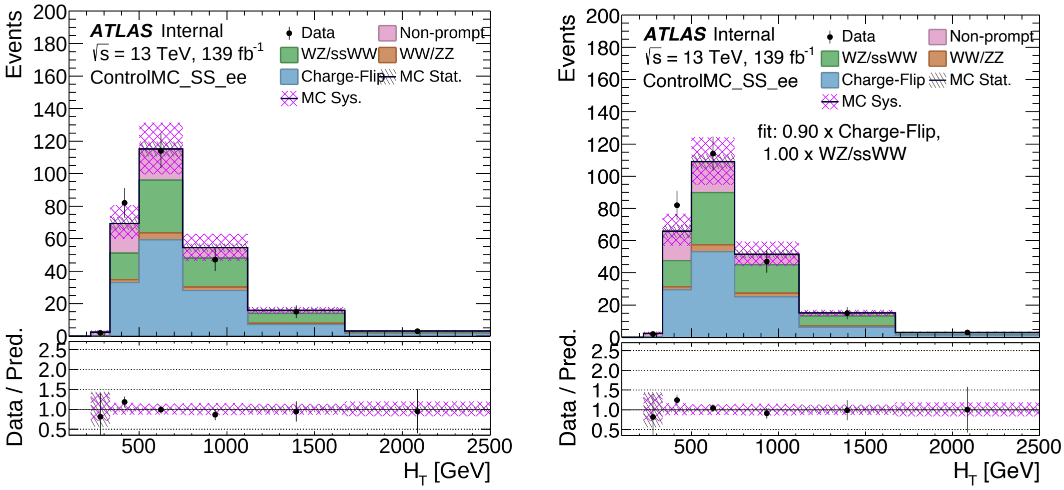

(a) (b)

Figure 9.5: Pre (a) and post (b) fit H_T distributions for the SS ee Control Region.

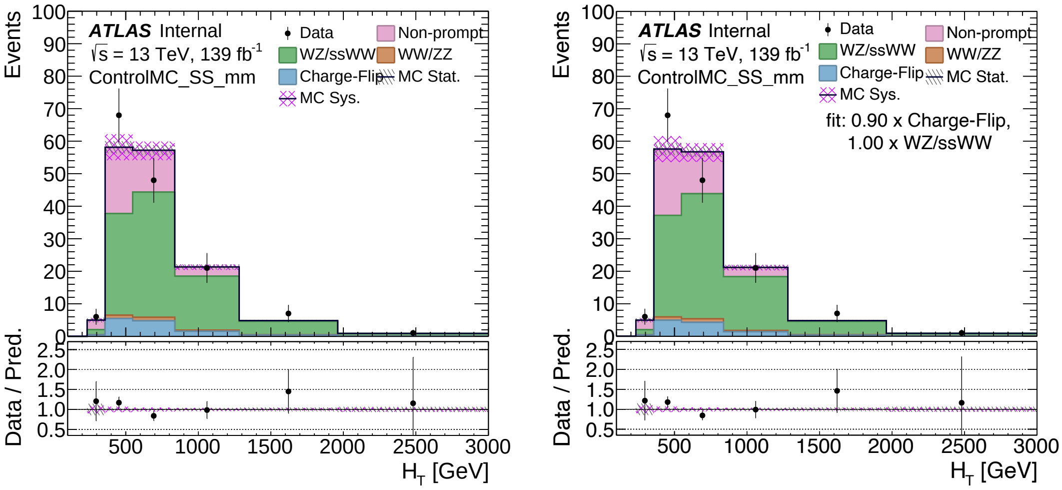

(a) (b)

Figure 9.6: Pre (a) and post (b) fit H_T distributions for the SS $\mu\mu$ Control Region.

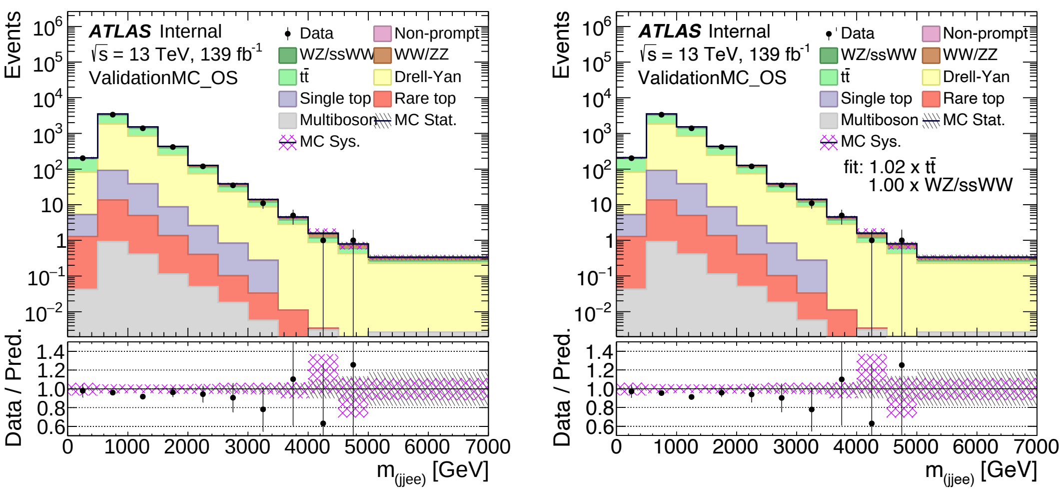

(a) (b)

Figure 9.7: Pre (a) and post (b) fit m_{jjll} distributions for the OS ee Validation Region.

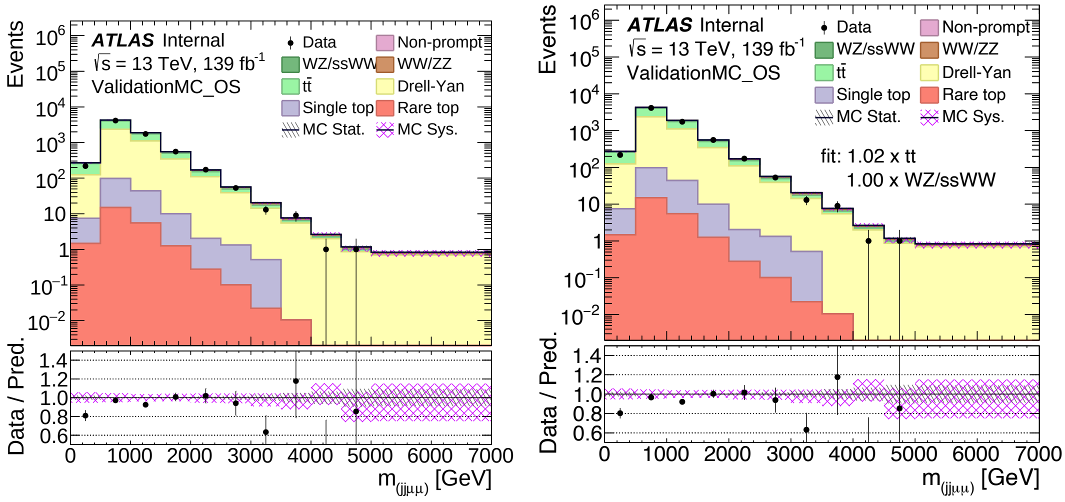

(a) (b)

Figure 9.8: Pre (a) and post (b) fit m_{jjll} distributions for the OS $\mu\mu$ Validation Region.

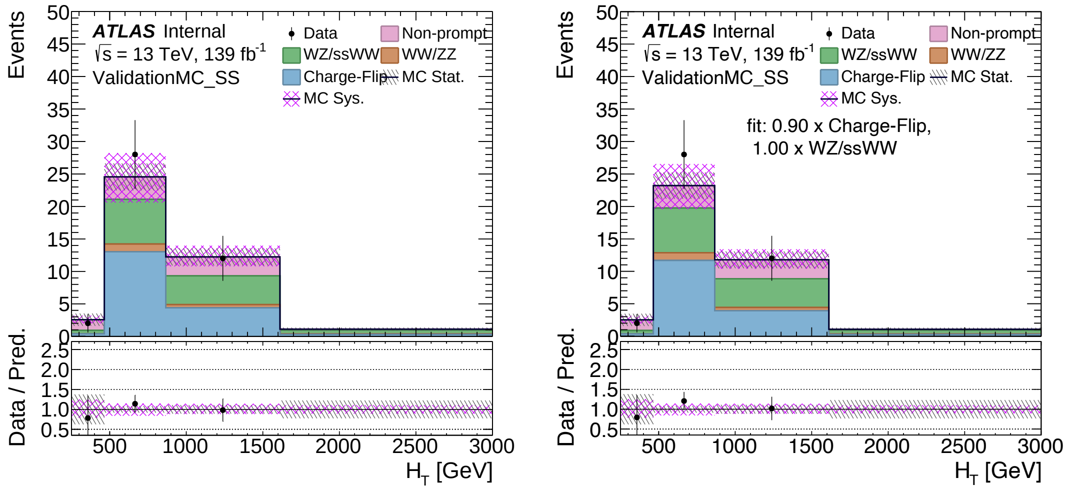

(a) (b)

Figure 9.9: Pre (a) and post (b) fit H_T distributions for the SS ee Validation Region.

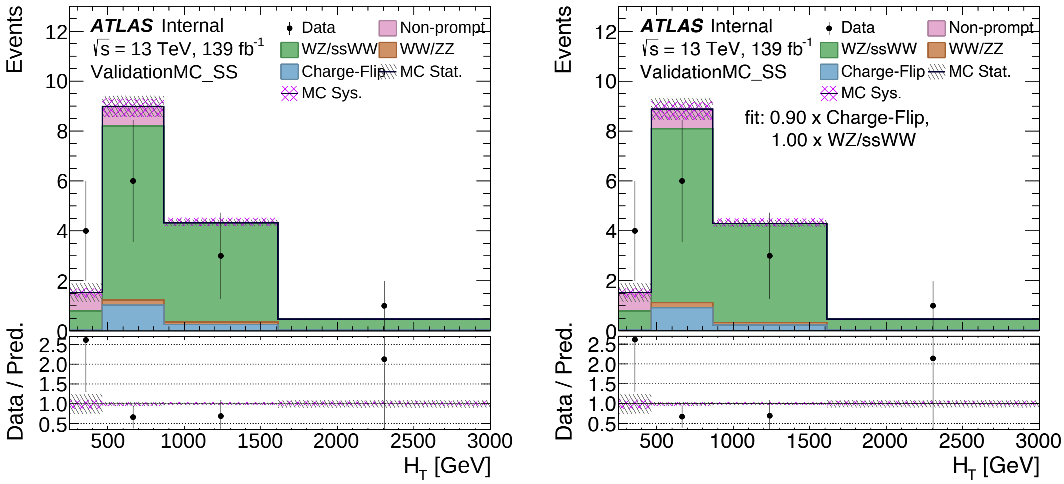

(a) (b)

Figure 9.10: Pre (a) and post (b) fit H_T distributions for the SS $\mu\mu$ Validation Region.

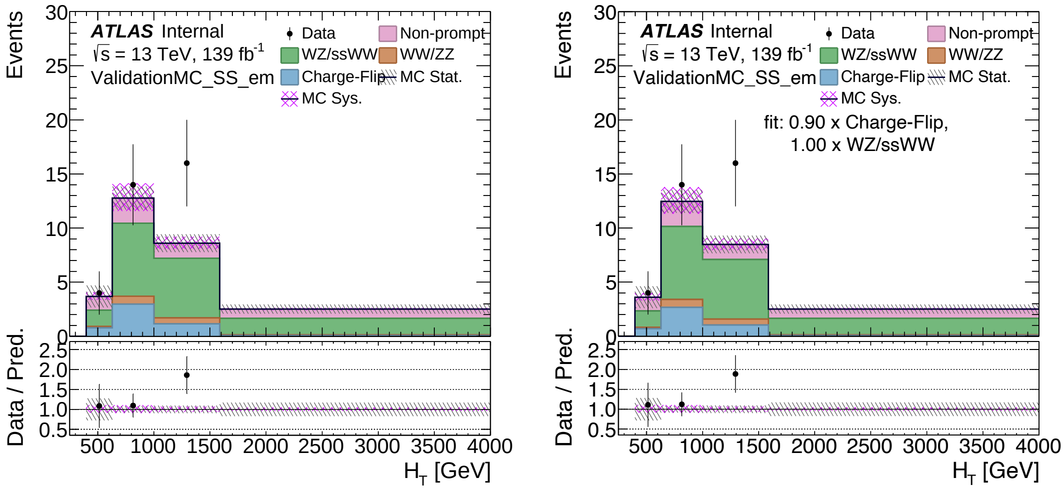

(a) (b)

Figure 9.11: Pre (a) and post (b) fit H_T distributions for the SS em Validation Region.

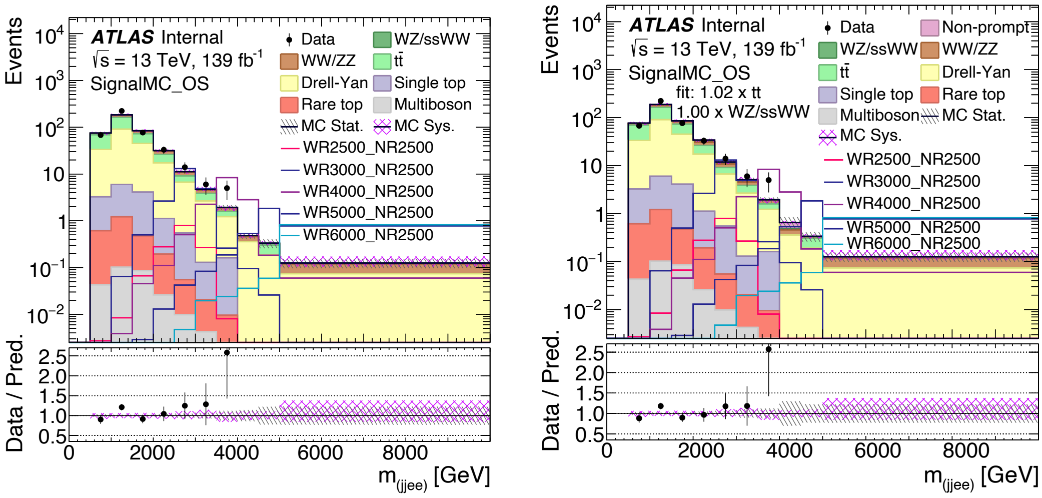

(a) (b)

Figure 9.12: Pre (a) and post (b) fit m_{jjll} distributions for the OS ee Nominal hierarchy Signal Region.

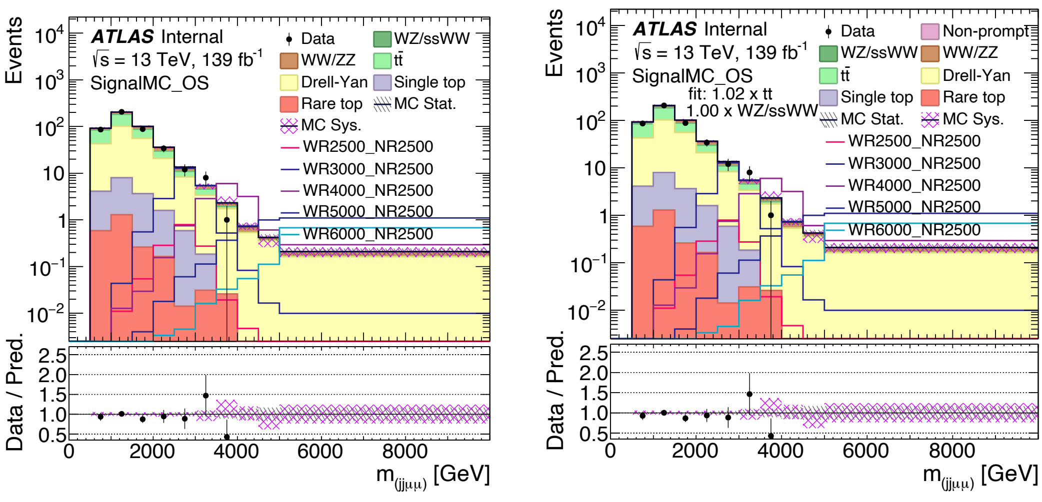

(a) (b)

Figure 9.13: Pre (a) and post (b) fit m_{jjll} distributions for the OS $\mu\mu$ Nominal hierarchy Signal Region.

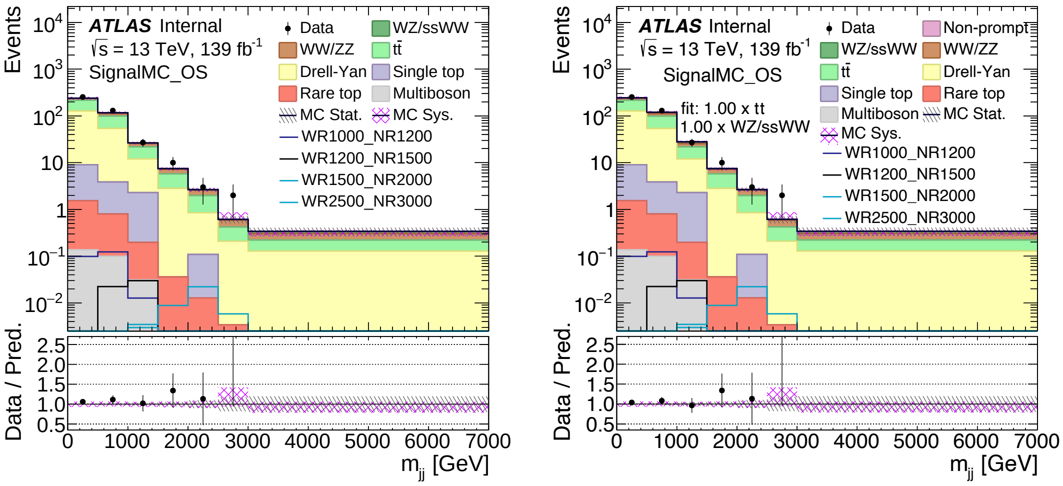

(a) (b)

Figure 9.14: Pre (a) and post (b) fit m_{jj} distributions for the OS ee Inverse hierarchy Signal Region.

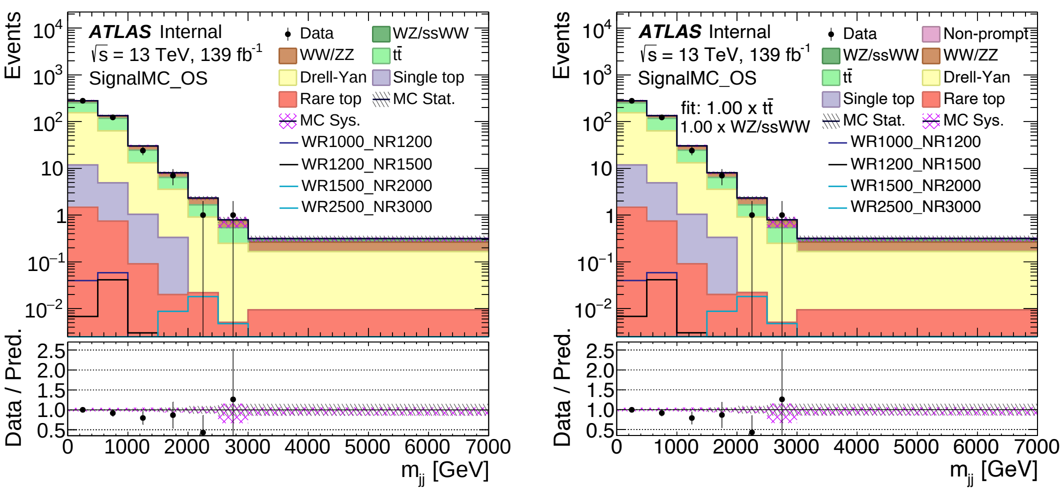

(a) (b)

Figure 9.15: Pre (a) and post (b) fit m_{jj} distributions for the OS $\mu\mu$ Inverse hierarchy Signal Region.

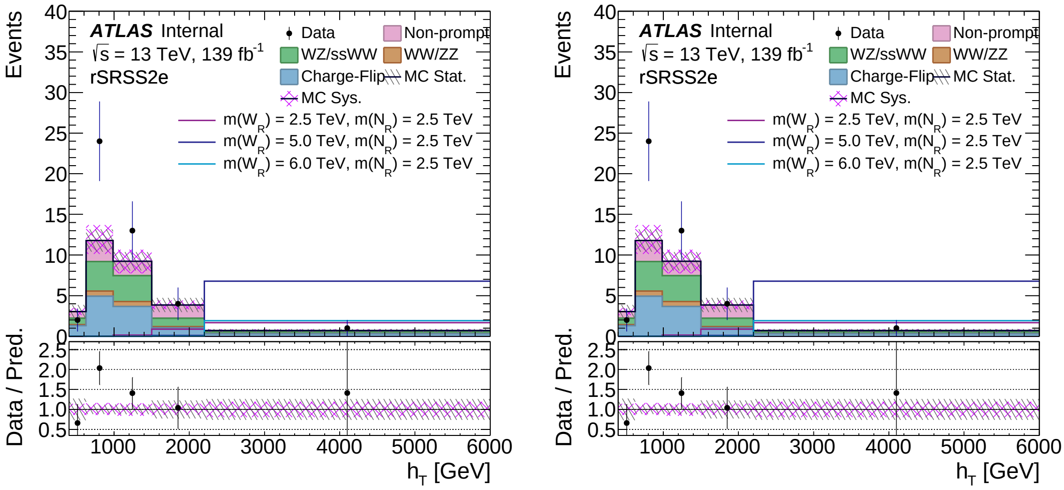

(a) (b)

Figure 9.16: Pre (a) and post (b) fit H_T distributions for the SS ee Signal Region.

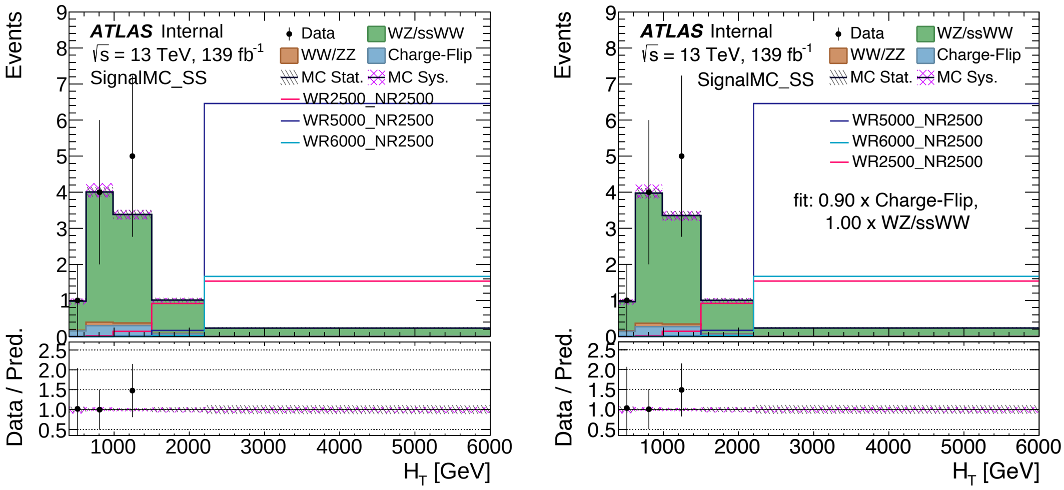

(a) (b)

Figure 9.17: Pre (a) and post (b) fit H_T distributions for the SS $\mu\mu$ Signal Region.

9.1.3.2 Signal + Background

Fits with μ_S unconstrained are utilised in order to test various m(W_R)–m(N_R) hypotheses and set upper limits on the KS process. Two different fit channels, ee and $\mu\mu$ are defined to target N_e and N_μ as their masses are not constrained to be the same. In each channel, all Control Regions are included in the fit, but only the corresponding same-flavour signal Regions are used. Additionally, no signal prediction is included in the Control Region of the opposite flavour channel, as doing this would assume identical masses for N_e and N_μ.

For the Majorana N_R case, both the Opposite- and Same-Sign channels are used in the fit, while for the Dirac N_R case, only the Opposite-Sign channel is used, with twice the cross-section of the Majorana case.

Electron systematic uncertainties are considered only in the ee Control, signal and validation Regions, whilst muon systematic uncertainties are only considered in the $\mu\mu$ Control, signal and validation Regions. Both electron and muon systematic uncertainties are considered in the $e\mu$ Control and Validation Regions.

The VRs are not included in the fits, but the post-fit values of the likelihood function parameters were applied in the VRs to verify the background modelling and verify the fit performance.

Post-fit binned distributions for a few selected mass points are shown in Figures 9.12 - 9.17 for the signal Regions with signal distributions overlaid.

9.2 Limit setting procedure

The profile likelihood ratio test statistic, q_μ, was used to discriminate between signal-like and background-like data distributions, defined as [168]:

$$q_\mu = -2\ln\left(\frac{\mathcal{L}\left(\mu_\mathrm{S}, \hat{\hat{\boldsymbol{\mu}}}_{\mathbf{B}_{\mu_\mathrm{S}}}, \hat{\boldsymbol{\theta}}_{\mu_\mathrm{S}}\right)}{\mathcal{L}\left(\hat{\mu_\mathrm{S}}, \hat{\boldsymbol{\mu}}_\mathbf{B}, \hat{\boldsymbol{\theta}}\right)}\right)$$

where the denominator is the so-called unconditional likelihood, where the likelihood function is maximised with μ_S, μ_B and θ all allowed to vary, and the numerator is the so-called conditional likelihood, where the likelihood is maximised for a fixed value of μ_S. Higher values of q_μ correspond to a larger disagreement between the chosen value of μ_S and the data, whereas lower values of q_μ indicate better compatibility between data and the chosen value of μ_S.

The probability p_{S+B} that a signal plus background (S+B) hypothesis (for example, $\mu_S = 1$ for a Majorana N_R and $\mu_S = 2$ for a Dirac N_R with the nominal KS cross section) gives a test statistic above a reference value $\mathrm{q}_\mu{}^{\mathrm{ref}}$ or the probability p_B that a background-only hypothesis ($\mu_S = 0$) gives a test statistic below $\mathrm{q}_\mu{}^{\mathrm{ref}}$, are defined as [169]:

$$p_{\mathrm{B}} = P\left(q_\mu < q_\mu^{\mathrm{ref}} \mid \mathrm{B}\right) \quad = \int_{-\infty}^{q_\mu^{\mathrm{ref}}} f\left(q_\mu \mid \mathrm{B}\right) dq_\mu \equiv 1 - \mathrm{CL_b}$$
$$p_{\mathrm{S+B}} = P\left(q_\mu > q_\mu^{\mathrm{ref}} \mid \mathrm{S+B}\right) = \int_{q_\mu^{\mathrm{ref}}}^{\infty} f\left(q_\mu \mid \mathrm{S+B}\right) dq_\mu \equiv \mathrm{CL_{s+b}}$$

When calculating the observed limits from the real dataset, ${q_\mu}^{\mathrm{ref}}$ is the value of q_μ extracted from the fit to the observed data. For expected limits, ${q_\mu}^{\mathrm{ref}}$ is taken to be the median, $\pm 1\sigma$ and $\pm 2\sigma$ of q_μ extracted from a fit to a dataset that is generated to match the background prediction [168]. The probability density function (PDF) of the test statistic under a particular signal hypothesis, $\mathrm{f}(\mathrm{q}_\mu|\mathrm{hyp})$, is found using an asymptotic approximation [154, 168]. A value of μ_S is said to be excluded at 95% confidence level (CL) if it fulfils the following requirement [169]:

$$\mathrm{CL_s} \equiv \frac{p_{\mathrm{S+B}}}{1 - p_{\mathrm{B}}} = \frac{\mathrm{CL_{s+b}}}{\mathrm{CL_b}} \leq 5\%$$

The upper limit on the value of μ_S is the highest value of μ_S that cannot be excluded at 95% CL. To determine the upper limit on μ_S for each m(W_R)–m(N_R) hypothesis, CLs values were calculated for a range of μ_S values, to obtain a distribution of μ_S vs. CLs. The 95% CL excluded Region of m(W_R)–m(N_R) phase space is the area in which the upper limit on μ_S is less than 1 (for the Majorana N_R case) or less than 2 (for the Dirac N_R case). Examples of an upper limit scan on the Majorana neutrino case are shown in Figure 9.18, one marginally excluded and one not.

Chapter 10 includes and discusses the results of this analysis.

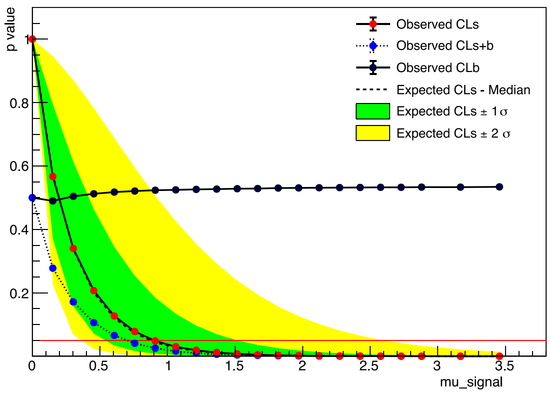

(a) m(W_R) = 5.5 TeV, m(N_R) = 2 TeV

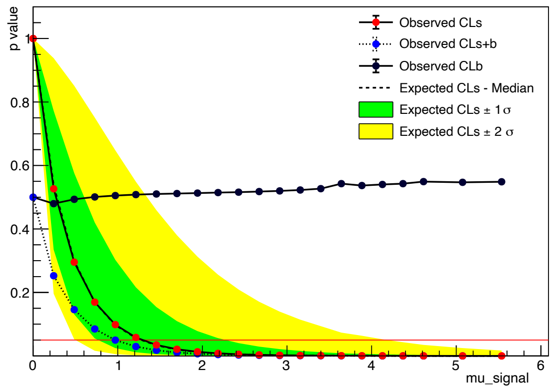

(b) m(W_R) = 5.5 TeV, m(N_R) = 3 TeV

Figure 9.18: Upper limit scan on the signal strength parameter, μ_S, as a function of the p-value for two different mass points. The "expected upper limit" ("observed upper limit") is the μ_S value for which the expected (observed) CLs line crosses over the 0.05 p-value (continuous red line). If it is below $\mu_S = 1$ the mass sample is expected (observed) to be excluded. For the two examples provided, (a) is expected and observed to be excluded since the upper limit is 0.9, while (b) is not, since the upper limit is 1.2.

Chapter 10

Results

In this chapter, the final results obtained in the analysis described in this thesis are presented. Results from the resolved analysis are presented in Section 10.1 and discussed in Section 10.2. An overlay of the results obtained in this thesis from the boosted channel and previous publications is shown in Section 10.3.

10.1 Resolved channel Exclusion limits

Exclusion limits as a function of the W_R and N_R masses are presented in Figure 10.1. Limits are set for both Majorana and Dirac N_R hypotheses.

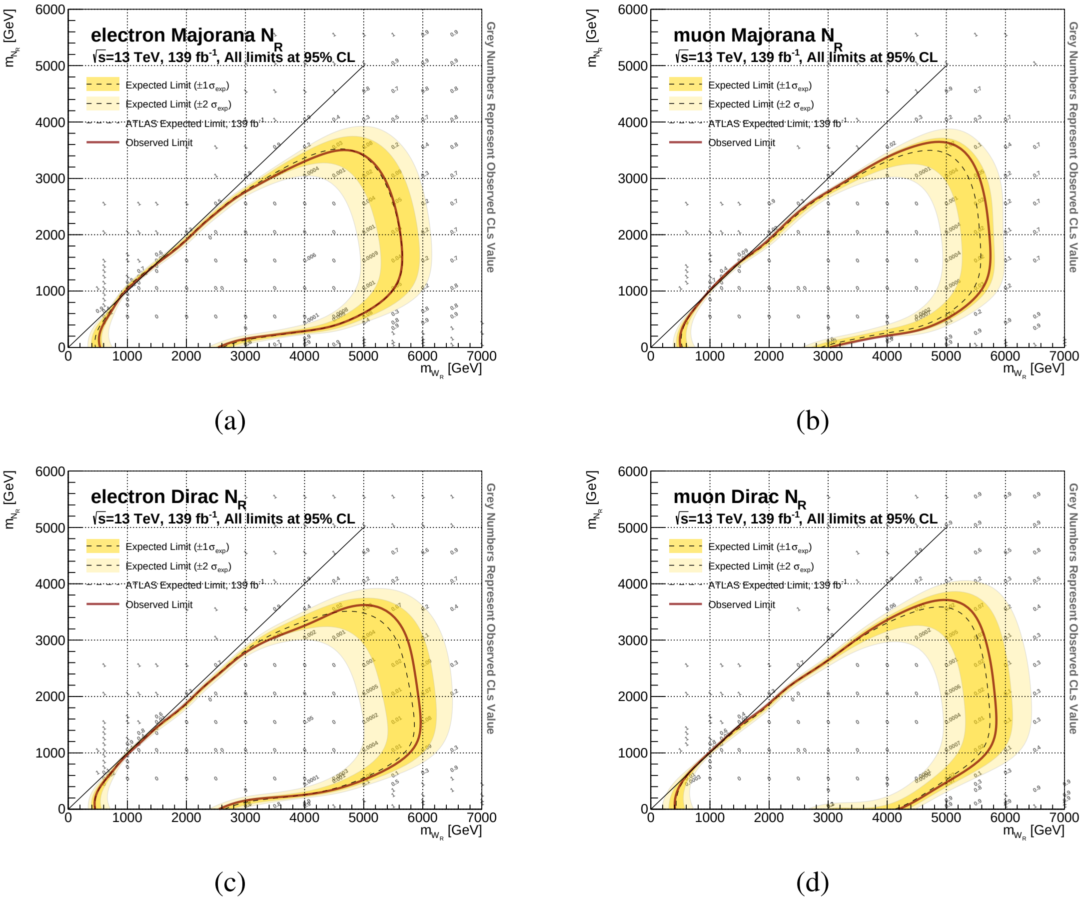

Figure 10.1: Expected and observed 95% CL exclusion contours in the m(W_R) - m(N_R) plane, along with the one- and two-standard-deviation uncertainty bands around the expected exclusion contour in the (a) ee and (b) $\mu\mu$ channels for Majorana N_R neutrinos, and (c) ee and (d) $\mu\mu$ channels for Dirac N_R neutrinos.

Figures 10.2 and 10.3, show upper limits on cross-section for two m(W_R), m(N_R) ratios, for the KS process.

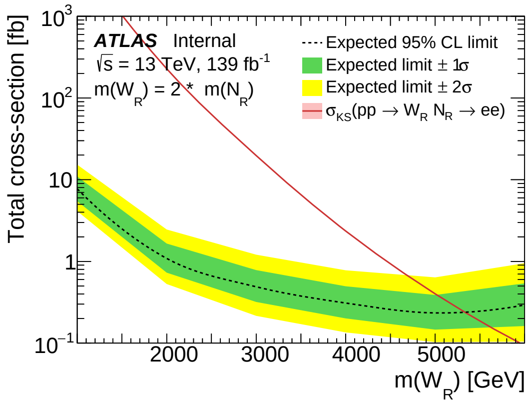

(a) electron Majorana N_R

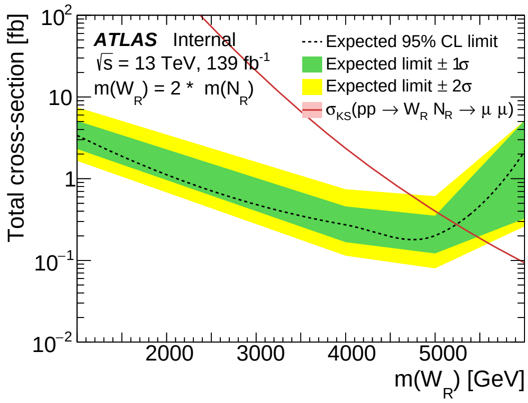

(b) muon Majorana N_R

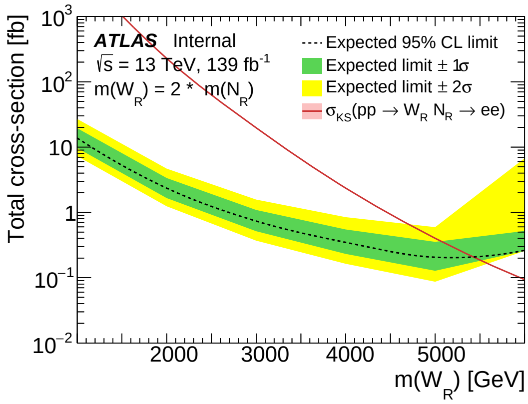

(c) electron Dirac N_R

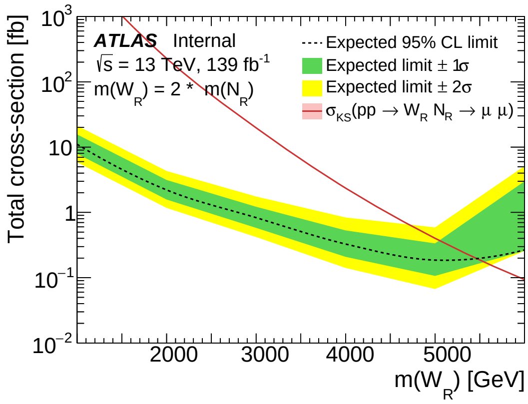

(d) muon Dirac N_R

Figure 10.2: Upper limits on cross-section for the case when the W_R mass is twice the N_R mass (slices of figure 10.1).

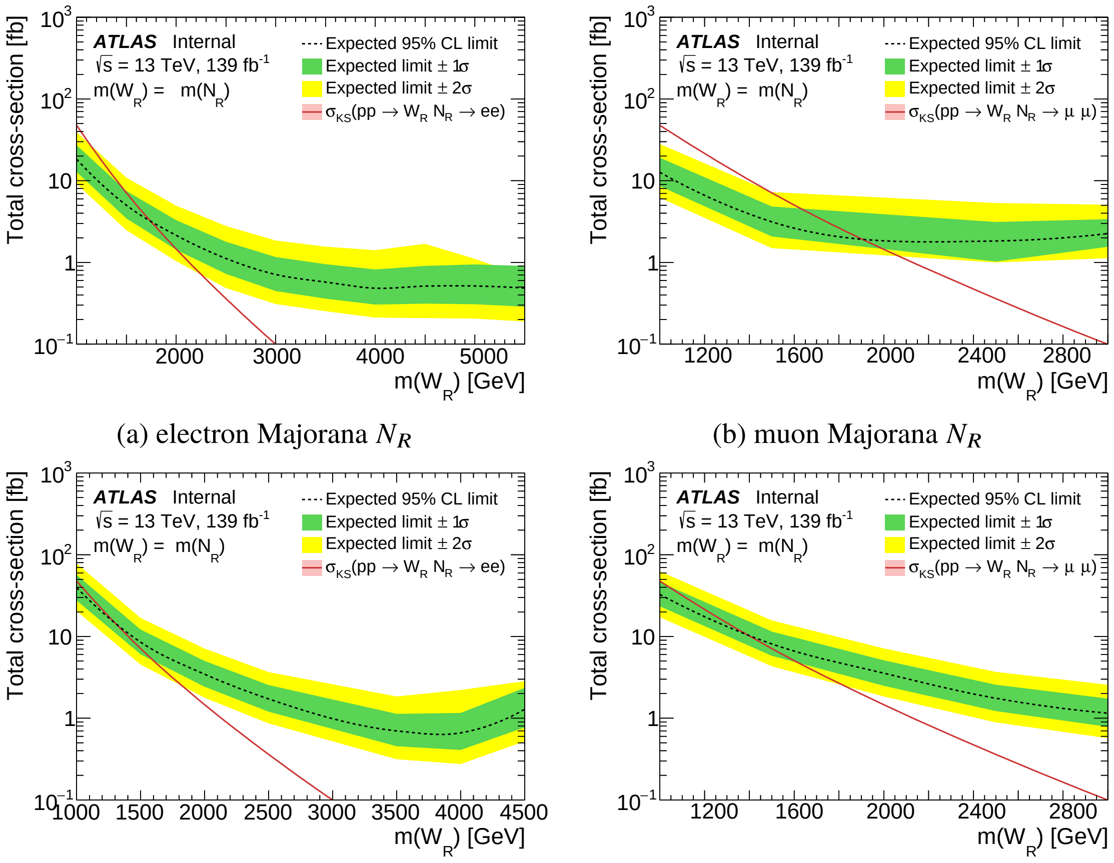

(a) electron Majorana N_R

(b) muon Majorana N_R

(c) electron Dirac N_R

(d) muon Dirac N_R

Figure 10.3: Upper limits on cross-section for the case when the W_R mass is equal to the N_R mass (slices of figure 10.1).

10.2 Discussion

No evidence for the existence of W_R and N_R has been found. For electron Majorana neutrinos, the excluded region extends to a W_R mass of 5.6 TeV and a N_R mass of 3.4 TeV. For muon Majorana neutrinos, W_R masses of up to 5.7 TeV were excluded, and N_R masses of up to 3.6 TeV. For electron Dirac neutrinos, the excluded region extends to a W_R mass of 6 TeV and a N_R mass of 3.5 TeV. For muon Dirac neutrinos, W_R masses of up to 5.8 TeV were excluded, and N_R masses of up to 3.7 TeV.

The limits from this analysis improve the previous results on W_R and Majorana N_R mass, obtained by the CMS collaboration at $\sqrt{s}$= 13 TeV [72]. The regions excluded by CMS excluded W_R masses up to 4.7 GeV in the resolved electron channel and 5.0 GeV in the resolved muon channel. There is no Dirac neutrino exclusion limit from CMS.

Compared to the last iteration of the resolved ATLAS analysis [61], the exclusion limits set by the resolved channel of the analysis improve them in the Nominal hierarchy case by 1.5 TeV in regards to the W_R mass. For the inverse hierarchy case (ie when m(N_R) > m(W_R) - above the black line in figure 10.1), this analysis did not show the same sensitivity as the previous iteration. It is in general hard to exclude any region in the m(N_R) > m(W_R) phase space for a number of reasons. Firstly, the KS production cross section, for a given value of m(W_R) , decreases as m(N_R) increases (see Figure 6.2 and figures 9.14,9.15). In phase space regions where the KS production cross section is not prohibitively low, the W_R mass is low, so the separation between signal and background is poor. In hindsight, a specialised analysis channel with looser baseline event selection and kinematic criteria (for example jet p_{T} and $|\eta|$) could have potentially given this analysis more sensitivity in that analysis region.

Between the last iteration of the ATLAS resolved analysis, and the work described in this thesis (resolved and boosted channels), these results set the most stringent limits on W_R and N_R masses in the world. A paper that includes the analysis and results described in this thesis is in the process of being published under the name "Search for heavy Majorana or Dirac neutrinos and right-handed W_R bosons in final states with charged leptons and jets at $\sqrt{s}$ = 13 TeV with the ATLAS detector".

10.3 Exclusion limits Overlay

The exclusion limits on the W_R and N_R mass plane, for both the resolved and boosted channels, as well as those from previous analyses are presented in Figure 10.4. The yellow colour corresponds to the results obtained in this thesis and is the same as the one shown in section 10.1. The green colour corresponds to the boosted channel (no statistical combination was performed between the two). The purple and blue colours are the previous iterations (resolved and boosted) of the ATLAS analysis [61, 67]. The grey colour corresponds to the latest result by CMS [72] (resolved and boosted).

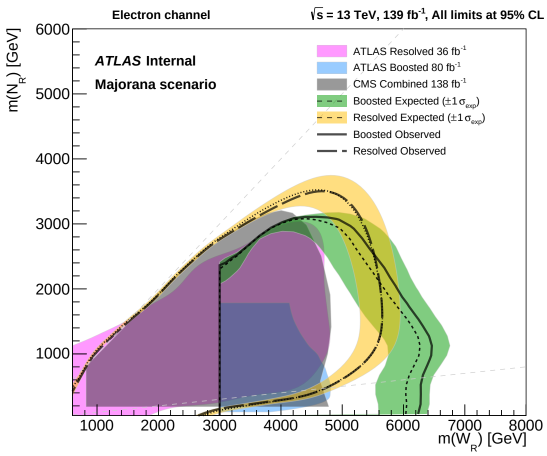

(a)

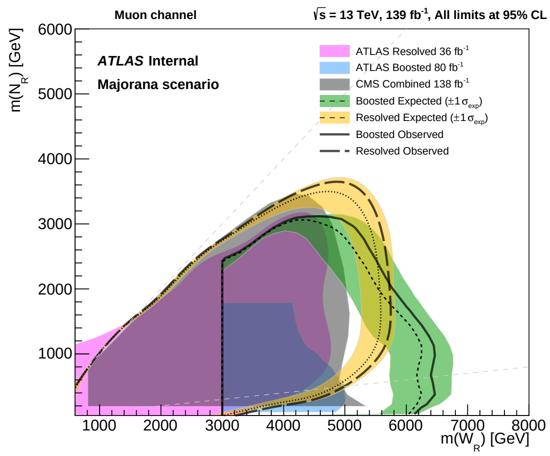

(b)

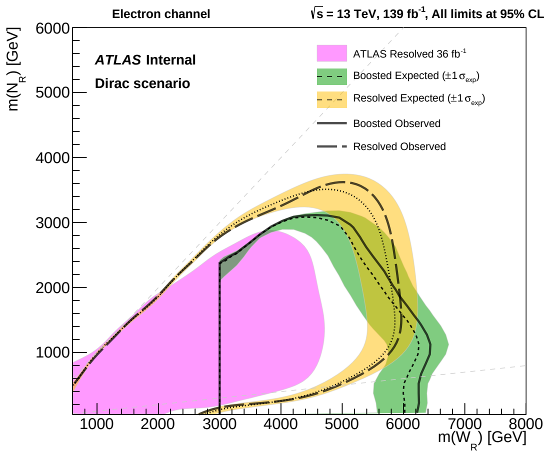

(c)

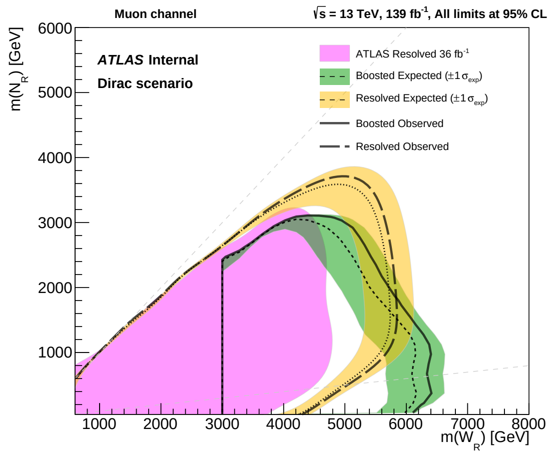

(d)

Figure 10.4: Expected and observed 95% CL exclusion contours in the m(W_R) - m(N_R) plane, along with the one- and two-standard-deviation uncertainty bands around the expected exclusion contour in the (a) ee and (b) $\mu\mu$ channels for Majorana N_R neutrinos, and (c) ee and (d) $\mu\mu$ channels for Dirac N_R neutrinos. See the text for a breakdown of the different limits.

Chapter 11

Conclusion

Left-Right Symmetric Models (LRSM) are a promising class of extensions to the Standard Model of particle physics (SM). By introducing a right-handed component to the weak force, LRSM can restore the parity symmetry to the SM and provide a viable mechanism for generating the small masses of the known neutrinos. Two forms of LRSM were considered in this thesis, which predict the existence of heavy right-handed W bosons, W_R, and either Majorana or Dirac heavy right-handed neutrinos, N_R.

An analysis searching for LRSM W_R and N_R in final states with two electrons or muons has been performed, focusing on the Keung-Senjanović (KS) process. In this analysis 139 fb^{-1} of high-quality collision data, collected during Run2 (2015-2018) by the ATLAS experiment at $\sqrt{s} = 13$ TeV were analysed. The signal and background processes were modelled using Monte Carlo datasets, and various selections were implemented to increase the analysis's sensitivity.

The data was found to be compatible with the SM prediction and exclusion limits were set on the possible masses of the W_R and N_R. The limits found are the current most stringent on m(W_R) and m(N_R), reaching W_R masses up to 6 TeV for N_R masses between $\sim$ 500 GeV and $\sim$ 3.5 TeV.

There are few items that could be addressed on a later iteration of this analysis. To start with, this search is bound by the amount of statistics, so the Run3 and beyond data will definitely be invaluable to further explore the phase-space in question. From a theoretical standpoint, the model used to generate the signal samples could be tuned to allow mixing between the various flavours of the N_R. From the analysis side, it would be potentially beneficial to have a specified channel for the inverse hierarchy case, to improve the sensitivity. Another novel direction for a new analysis to explore would be the use of the N_R mass in addition to the W_R mass. It was shown that a relatively simple model can estimate the mass of the N_R with high precision, but this was not utilised.

Bibliography

[1] ATLAS Collaboration. "Operation of the ATLAS trigger system in Run 2" ().

[2] Sheldon L Glashow. "Partial-symmetries of weak interactions". *Nuclear physics* 22.4 (1961), pp. 579–588.

[3] Abdus Salam and John Clive Ward. *Electromagnetic and weak interactions*. Tech. rep. IMPERIAL COLL OF SCIENCE and TECHNOLOGY LONDON (ENGLAND), 1964.

[4] Steven Weinberg. "A Model of Leptons". *Phys. Rev. Lett.* 19 (21 Nov. 1967), pp. 1264–1266. DOI: 10.1103/PhysRevLett.19.1264. URL: https://link.aps.org/doi/10.1103/PhysRevLett.19.1264.

[5] H. David Politzer. "Reliable Perturbative Results for Strong Interactions?" *Phys. Rev. Lett.* 30 (26 June 1973), pp. 1346–1349. DOI: 10.1103/PhysRevLett.30.1346. URL: https://link.aps.org/doi/10.1103/PhysRevLett.30.1346.

[6] Steven Weinberg. "Non-Abelian Gauge Theories of the Strong Interactions". *Phys. Rev. Lett.* 31 (7 Aug. 1973), pp. 494–497. DOI: 10.1103/PhysRevLett.31.494. URL: https://link.aps.org/doi/10.1103/PhysRevLett.31.494.

[7] David J. Gross and Frank Wilczek. "Ultraviolet Behavior of Non-Abelian Gauge Theories". *Phys. Rev. Lett.* 30 (26 June 1973), pp. 1343–1346. DOI: 10.1103/PhysRevLett.30.1343. URL: https://link.aps.org/doi/10.1103/PhysRevLett.30.1343.

[8] *D. Galbraith and C. Burgard, Standard Model Standard Infographic*. http://davidgalbraith.org/portfolio/ux-standard-model-of-the-standard-model/. Accessed: 2022-04-27.

[9] *C. Burgard, Example: Standard model of physics*. http://www.texample.net/tikz/examples/model-physics/. Accessed: 2022-04-27.

[10] M. Tanabashi et al. "Review of Particle Physics". *Phys. Rev. D* 98 (3 Aug. 2018), p. 030001. DOI: 10.1103/PhysRevD.98.030001. URL: https://link.aps.org/doi/10.1103/PhysRevD.98.030001.

[11] Peter W. Higgs. "Broken Symmetries and the Masses of Gauge Bosons". *Phys. Rev. Lett.* 13 (16 Oct. 1964), pp. 508–509. DOI: 10.1103/PhysRevLett.13.508. URL: https://link.aps.org/doi/10.1103/PhysRevLett.13.508.

[12] F. Englert and R. Brout. "Broken Symmetry and the Mass of Gauge Vector Mesons". *Phys. Rev. Lett.* 13 (9 Aug. 1964), pp. 321–323. DOI: 10.1103/PhysRevLett.13.321. URL: https://link.aps.org/doi/10.1103/PhysRevLett.13.321.

[13] ATLAS Collaboration. "Observation of a new particle in the search for the Standard Model Higgs boson with the ATLAS detector at the LHC". *Physics Letters B* 716.1 (2012), pp. 1–29.

[14] CMS Collaboration. "Observation of a new boson at a mass of 125 GeV with the CMS experiment at the LHC". *Physics Letters B* 716.1 (2012), pp. 30–61.

[15] Emmy Noether. "Invariant variation problems". *Transport theory and statistical physics* 1.3 (1971), pp. 186–207.

[16] T. D. Lee and C. N. Yang. "Question of Parity Conservation in Weak Interactions". *Phys. Rev.* 104 (1 Oct. 1956), pp. 254–258. DOI: 10.1103/PhysRev.104.254. URL: https://link.aps.org/doi/10.1103/PhysRev.104.254.

[17] C. S. Wu et al. "Experimental Test of Parity Conservation in Beta Decay". *Phys. Rev.* 105 (4 Feb. 1957), pp. 1413–1415. DOI: 10.1103/PhysRev.105.1413. URL: https://link.aps.org/doi/10.1103/PhysRev.105.1413.

[18] Richard L. Garwin, Leon M. Lederman, and Marcel Weinrich. "Observations of the Failure of Conservation of Parity and Charge Conjugation in Meson Decays: the Magnetic Moment of the Free Muon". *Phys. Rev.* 105 (4 Feb. 1957), pp. 1415–1417. DOI: 10.1103/PhysRev.105.1415. URL: https://link.aps.org/doi/10.1103/PhysRev.105.1415.

[19] Claudia Patrignani et al. "Review of particle physics" (2016), pp. 7, 11, 37, 73, 89.

[20] Bruno Pontecorvo. "Mesonium and antimesonium". *Soviet Journal of Experimental and Theoretical Physics* 6 (1958), p. 429.

[21] Bruno Pontecorvo. "INVERSE *beta* PROCESSES AND NONCONSERVATION OF LEPTON CHARGE". *Zhur. Eksptl'. i Teoret. Fiz.* 34 (1958).

[22] Ziro Maki, Masami Nakagawa, and Shoichi Sakata. "Remarks on the Unified Model of Elementary Particles". *Progress of Theoretical Physics* 28.5 (Nov. 1962), pp. 870–880. ISSN: 0033-068X. DOI: 10.1143/PTP.28.870. eprint: https://academic.oup.com/ptp/article-pdf/28/5/870/5258750/28-5-870.pdf. URL: https://doi.org/10.1143/PTP.28.870.

[23] Bruno Pontecorvo. "Neutrino experiments and the problem of conservation of leptonic charge". *Sov. Phys. JETP* 26.984-988 (1968), p. 165.

[24] Samoil M Bilenky and B Pontecorvo. *Lepton mixing and the"solar neutrino puzzle"*. Tech. rep. Joint Inst. for Nuclear Research, 1977.

[25] Bruce T. Cleveland et al. "Measurement of the Solar Electron Neutrino Flux with the Homestake Chlorine Detector". *The Astrophysical Journal* 496.1 (Mar. 1998), pp. 505–526. DOI: 10.1086/305343. URL: https://doi.org/10.1086/305343.

[26] Q. R. Ahmad et al. "Measurement of the Rate of $\nu_e + d \rightarrow p + p + e^-$ Interactions Produced by ^8B Solar Neutrinos at the Sudbury Neutrino Observatory". *Phys. Rev. Lett.* 87 (7 July 2001), p. 071301. DOI: 10.1103/PhysRevLett.87.071301. URL: https://link.aps.org/doi/10.1103/PhysRevLett.87.071301.

[27] Super-Kamiokande. "The Super-Kamiokande detector". *Nuclear Instruments and Methods in Physics Research Section A: Accelerators, Spectrometers, Detectors and Associated Equipment* 501.2 (2003), pp. 418–462. ISSN: 0168-9002. DOI: https://doi.org/10.1016/S0168-9002(03)00425-X. URL: https://www.sciencedirect.com/science/article/pii/S016890020300425X.

[28] K.A. Olive. "Review of Particle Physics". *Chinese Physics C* 40.10 (Oct. 2016), p. 100001. DOI: 10.1088/1674-1137/40/10/100001. URL: https://doi.org/10.1088/1674-1137/40/10/100001.

[29] Alexey Lokhov et al. "Background reduction at the KATRIN experiment by the shifted analysing plane configuration". *The European Physical Journal C* 82.3 (2022), pp. 1–11.

[30] ALEPH Collaboration. "An upper limit on the τneutrino mass from three- and five-prong tau decays" ().

[31] Zackaria Chacko et al. "Cosmological limits on the neutrino mass and lifetime". *Journal of High Energy Physics* 2020.4 (2020), pp. 1–33.

[32] Rabindra N Mohapatra and Palash B Pal. *Massive neutrinos in physics and astrophysics*. Vol. 72. World scientific, 2004.

[33] Paul Adrien Maurice Dirac. "The quantum theory of the electron". *Proceedings of the Royal Society of London. Series A, Containing Papers of a Mathematical and Physical Character* 117.778 (1928), pp. 610–624.

[34] Hideki Yukawa. "On the Interaction of Elementary Particles. I". *Progress of Theoretical Physics Supplement* 1 (Jan. 1955), pp. 1–10. ISSN: 0375-9687. DOI: 10.1143/PTPS.1.1. eprint: https://academic.oup.com/ptps/article-pdf/doi/10.1143/PTPS.1.1/5310694/1-1.pdf. URL: https://doi.org/10.1143/PTPS.1.1.

[35] J Tiomno. "Mass reversal and the universal interaction". *Il Nuovo Cimento (1955-1965)* 1.1 (1955), pp. 226–232.

[36] T. D. Lee and C. N. Yang. “Parity Nonconservation and a Two-Component Theory of the Neutrino”. *Phys. Rev.* 105 (5 Mar. 1957), pp. 1671–1675. DOI: 10.1103/PhysRev.105.1671. URL: https://link.aps.org/doi/10.1103/PhysRev.105.1671.

[37] L. Landau. “On the conservation laws for weak interactions”. *Nuclear Physics* 3.1 (1957), pp. 127–131. ISSN: 0029-5582. DOI: https://doi.org/10.1016/0029-5582(57)90061-5. URL: https://www.sciencedirect.com/science/article/pii/0029558257900615.

[38] Ettore Majorana. “Teoria simmetrica dell’elettrone e del positrone”. *Il Nuovo Cimento (1924-1942)* 14.4 (1937), pp. 171–184.

[39] Jogesh C. Pati and Abdus Salam. “Lepton number as the fourth "color"”. *Phys. Rev. D* 10 (1 1974), pp. 275–289. DOI: 10.1103/PhysRevD.10.275. URL: https://link.aps.org/doi/10.1103/PhysRevD.10.275.

[40] Rabindra N. Mohapatra and Jogesh C. Pati. “Left-right gauge symmetry and an "isoconjugate" model of CP violation”. *Phys. Rev. D* 11 (3 1975), pp. 566–571. DOI: 10.1103/PhysRevD.11.566. URL: https://link.aps.org/doi/10.1103/PhysRevD.11.566.

[41] R. N. Mohapatra and J. C. Pati. “"Natural" left-right symmetry”. *Phys. Rev. D* 11 (9 1975), pp. 2558–2561. DOI: 10.1103/PhysRevD.11.2558. URL: https://link.aps.org/doi/10.1103/PhysRevD.11.2558.

[42] G. Senjanovic and R. N. Mohapatra. “Exact left-right symmetry and spontaneous violation of parity”. *Phys. Rev. D* 12 (5 1975), pp. 1502–1505. DOI: 10.1103/PhysRevD.12.1502. URL: https://link.aps.org/doi/10.1103/PhysRevD.12.1502.

[43] Goran Senjanović. “Spontaneous breakdown of parity in a class of gauge theories”. *Nuclear Physics B* 153 (1979), pp. 334–364. ISSN: 0550-3213. DOI: https://doi.org/10.1016/0550-3213(79)90604-7. URL: https://www.sciencedirect.com/science/article/pii/0550321379906047.

[44] M Gell-Mann and P Ramond. *R. Slansky in Supergravity,(P. van Nieuwenhuizen and D. Freedman eds) North-Holland, Amsterdam, 1979; SL Glashow*. 1980.

[45] J. Schechter and J. W. F. Valle. “Neutrino masses in SU(2) $\bigotimes$ U(1) theories”. *Phys. Rev. D* 22 (9 1980), pp. 2227–2235. DOI: 10.1103/PhysRevD.22.2227. URL: https://link.aps.org/doi/10.1103/PhysRevD.22.2227.

[46] Peter Minkowski. “mu -> e gamma at a rate of one out of 109 muon decays?” *Physics Letters B* 67.4 (1977), pp. 421–428. ISSN: 0370-2693. DOI: https://doi.org/10.1016/0370-2693(77)90435-X. URL: https://www.sciencedirect.com/science/article/pii/037026937790435X.

[47] Rabindra N. Mohapatra and Goran Senjanovi ć. "Neutrino Mass and Spontaneous Parity Nonconservation". *Phys. Rev. Lett.* 44 (14 1980), pp. 912–915. DOI: 10.1103/PhysRevLett.44.912. URL: https://link.aps.org/doi/10.1103/PhysRevLett.44.912.

[48] R.E. Marshak and R.N. Mohapatra. "Quark-lepton symmetry and B - L as the U(1) generator of the electroweak symmetry group". *Physics Letters B* 91.2 (1980), pp. 222–224. ISSN: 0370-2693. DOI: https://doi.org/10.1016/0370-2693(80)90436-0. URL: https://www.sciencedirect.com/science/article/pii/0370269380904360.

[49] R. N. Mohapatra and R. E. Marshak. "Local $B - L$ Symmetry of Electroweak Interactions, Majorana Neutrinos, and Neutron Oscillations". *Phys. Rev. Lett.* 44 (20 1980), pp. 1316–1319. DOI: 10.1103/PhysRevLett.44.1316. URL: https://link.aps.org/doi/10.1103/PhysRevLett.44.1316.

[50] Rabindra N. Mohapatra. "Mechanism for understanding small neutrino mass in superstring theories". *Phys. Rev. Lett.* 56 (6 1986), pp. 561–563. DOI: 10.1103/PhysRevLett.56.561. URL: https://link.aps.org/doi/10.1103/PhysRevLett.56.561.

[51] R. N. Mohapatra and J. W. F. Valle. "Neutrino mass and baryon-number nonconservation in superstring models". *Phys. Rev. D* 34 (5 1986), pp. 1642–1645. DOI: 10.1103/PhysRevD.34.1642. URL: https://link.aps.org/doi/10.1103/PhysRevD.34.1642.

[52] Chien-Yi Chen and PS Bhupal Dev. "Multilepton collider signatures of heavy Dirac and Majorana neutrinos". *Physical Review D* 85.9 (2012), p. 093018.

[53] PS Bhupal Dev and RN Mohapatra. "Unified Explanation of the e e j j, Diboson, and Dijet Resonances at the LHC". *Physical Review Letters* 115.18 (2015), p. 181803.

[54] Chandan Hati et al. "Neutrino masses and leptogenesis in left–right symmetric models: a review from a model building perspective". *Frontiers in Physics* 6 (2018), p. 19.

[55] Rabindra N. Mohapatra and Goran Senjanovi ć. "Neutrino masses and mixings in gauge models with spontaneous parity violation". *Phys. Rev. D* 23 (1 1981), pp. 165–180. DOI: 10.1103/PhysRevD.23.165. URL: https://link.aps.org/doi/10.1103/PhysRevD.23.165.

[56] N. G. Deshpande et al. "Left-right-symmetric electroweak models with triplet Higgs field". *Phys. Rev. D* 44 (3 1991), pp. 837–858. DOI: 10.1103/PhysRevD.44.837. URL: https://link.aps.org/doi/10.1103/PhysRevD.44.837.

[57] S. M. Bilenky and S. T. Petcov. "Massive neutrinos and neutrino oscillations". *Rev. Mod. Phys.* 59 (3 1987), pp. 671–754. DOI: 10.1103/RevModPhys.59.671. URL: https://link.aps.org/doi/10.1103/RevModPhys.59.671.

[58] Chien-Yi Chen and P. S. Bhupal Dev. "Multilepton collider signatures of heavy Dirac and Majorana neutrinos". *Physical Review D* 85.9 (2012). DOI: 10.1103/physrevd.85.093018. URL: https://doi.org/10.1103%2Fphysrevd.85.093018.

[59] Lincoln Wolfenstein. "Different varieties of massive Dirac neutrinos". *Nuclear Physics B* 186.1 (1981), pp. 147–152. ISSN: 0550-3213. DOI: https://doi.org/10.1016/0550-3213(81)90096-1. URL: https://www.sciencedirect.com/science/article/pii/0550321381900961.

[60] Arindam Das, PS Bhupal Dev, and Rabindra N Mohapatra. "Same sign versus opposite sign dileptons as a probe of low scale seesaw mechanisms". *Physical Review D* 97.1 (2018), p. 015018.

[61] Morad Aaboud et al. "Search for a right-handed gauge boson decaying into a high-momentum heavy neutrino and a charged lepton in pp collisions with the ATLAS detector at s= 13 TeV". *Physics Letters B* 798 (2019), p. 134942.

[62] ATLAS collaboration et al. "Search for heavy neutrinos and right-handed W bosons in events with two leptons and jets in pp collisions at sqrt (s)= 7 TeV with the ATLAS detector". *arXiv preprint arXiv:1203.5420* (2012).

[63] CMS. "Search for Heavy Neutrinos and WR Bosons with Right-Handed Couplings in a Left-Right Symmetric Model in pp Collisions at sqrt(s) = 7 TeV" ().

[64] ATLAS. "Search for heavy Majorana neutrinos with the ATLAS detector in pp collisions at sqrt(s) = 8 TeV" ().

[65] Vardan Khachatryan et al. "Search for heavy neutrinos and W bosons with right-handed couplings in proton proton collisions at sqrt(s)= 8 TeV". *The European Physical Journal C* 74.11 (2014), pp. 1–23.

[66] Albert M Sirunyan et al. "Search for a heavy right-handed W boson and a heavy neutrino in events with two same-flavor leptons and two jets at s= 13 TeV". *Journal of High Energy Physics* 2018.5 (2018), pp. 1–37.

[67] "Search for a right-handed gauge boson decaying into a high-momentum heavy neutrino and a charged lepton in pp collisions with the ATLAS detector at s=13 TeV". *Physics Letters B* 798 (2019), p. 134942. ISSN: 0370-2693. DOI: https://doi.org/10.1016/j.physletb.2019.134942. URL: ATLAS.

[68] Armen Tumasyan et al. "Search for a right-handed W boson and a heavy neutrino in proton-proton collisions at sqrt(s) = 13 TeV". *Journal of High Energy Physics* 2022.4 (2022), pp. 1–43.

[69] Georges Aad et al. "Search for new resonances in mass distributions of jet pairs using 139 fb- 1 of pp collisions at s sqrt(s) = 13 TeV with the ATLAS detector". *Journal of high energy physics* 2020.3 (2020), pp. 1–41.

[70] Albert M Sirunyan et al. “Search for high mass dijet resonances with a new background prediction method in proton-proton collisions at s sqrt(s) = 13 TeV”. *Journal of High Energy Physics* 2020.5 (2020), pp. 1–45.

[71] ATLAS. “Search for W to tb decays with the ATLAS detector in pp collisions at sqrt(s) = 13 TeV” ().

[72] ATLAS. “Search for vector boson resonances decaying to a top quark and bottom quark in the lepton plus jets final state in pp collisions at s = 13 TeV with the ATLAS detector” ().

[73] Lyndon Evans and Philip Bryant. “LHC Machine”. *Journal of Instrumentation* 3.08 (Aug. 2008), S08001–S08001. DOI: `10.1088/1748-0221/3/08/s08001`. URL: `https://doi.org/10.1088/1748-0221/3/08/s08001`.

[74] Esma Mobs. “The CERN accelerator complex. Complexe des accélérateurs du CERN” (July 2016). General Photo. URL: `https://cds.cern.ch/record/2197559`.

[75] D J Warner. *Project study for a new 50 MeV linear accelerator for the C. P. S.* Tech. rep. Geneva: CERN, Oct. 1973. URL: `https://cds.cern.ch/record/414071`.

[76] The ATLAS Collaboration et al. “The ATLAS Experiment at the CERN Large Hadron Collider”. *Journal of Instrumentation* 3.08 (Aug. 2008), S08003–S08003. DOI: `10.1088/1748-0221/3/08/s08003`. URL: `https://doi.org/10.1088/1748-0221/3/08/s08003`.

[77] The CMS Collaboration et al. “The CMS experiment at the CERN LHC”. *Journal of Instrumentation* 3.08 (Aug. 2008), S08004–S08004. DOI: `10.1088/1748-0221/3/08/s08004`. URL: `https://doi.org/10.1088/1748-0221/3/08/s08004`.

[78] The ALICE Collaboration. “The ALICE experiment at the CERN LHC”. *Journal of Instrumentation* 3.08 (Aug. 2008), S08002–S08002. DOI: `10.1088/1748-0221/3/08/s08002`. URL: `https://doi.org/10.1088/1748-0221/3/08/s08002`.

[79] The LHCb Collaboration. “The LHCb Detector at the LHC”. *Journal of Instrumentation* 3.08 (Aug. 2008), S08005–S08005. DOI: `10.1088/1748-0221/3/08/s08005`. URL: `https://doi.org/10.1088/1748-0221/3/08/s08005`.

[80] *ATLAS Collaboration, Luminosity Public Results for Run 2 – Multiple Year Collision Plots*. `https://twiki.cern.ch/twiki/bin/view/AtlasPublic/LuminosityPublicResultsRun2`. Accessed: 2022-04-27.

[81] M Capeans et al. *ATLAS Insertable B-Layer Technical Design Report*. Tech. rep. Sept. 2010. URL: `https://cds.cern.ch/record/1291633`.

[82] Joao Pequenao. “Computer generated image of the whole ATLAS detector”. Mar. 2008. URL: `https://cds.cern.ch/record/1095924`.

[83] *Combined measurements of Higgs boson production and decay using up to 80 fb of proton–proton collision data at sqrt(s)= 13 TeV collected with the ATLAS experiment*. Tech. rep. All figures including auxiliary figures are available at https://atlas.web.cern.ch/Atlas/GROUPS/PHYSICS/CONFNOTES/ATLAS-CONF-2018-031. Geneva: CERN, July 2018. URL: https://cds.cern.ch/record/2629412.

[84] Akira Yamamoto et al. "The ATLAS central solenoid". *Nuclear Instruments and Methods in Physics Research Section A: Accelerators, Spectrometers, Detectors and Associated Equipment* 584.1 (2008), pp. 53–74.

[85] *Track Reconstruction Performance of the ATLAS Inner Detector at* $\sqrt{s}$ = 13 *TeV*. Tech. rep. Geneva: CERN, July 2015. URL: https://cds.cern.ch/record/2037683.

[86] ATLAS. "ATLAS pixel detector electronics and sensors". *Journal of Instrumentation* 3.07 (July 2008), P07007–P07007. DOI: 10.1088/1748-0221/3/07/p07007. URL: https://doi.org/10.1088/1748-0221/3/07/p07007.

[87] The ATLAS TRT collaboration et al. "The ATLAS Transition Radiation Tracker (TRT) proportional drift tube: design and performance". *Journal of Instrumentation* 3.02 (Feb. 2008), P02013–P02013. DOI: 10.1088/1748-0221/3/02/p02013. URL: https://doi.org/10.1088/1748-0221/3/02/p02013.

[88] Bartosz Mindur, ATLAS Collaboration, et al. "ATLAS Transition Radiation Tracker (TRT): Straw tubes for tracking and particle identification at the Large Hadron Collider". *Nuclear Instruments and Methods in Physics Research Section A: Accelerators, Spectrometers, Detectors and Associated Equipment* 845 (2017), pp. 257–261.

[89] Joao Pequenao. "Computer Generated image of the ATLAS calorimeter". 2008. URL: https://cds.cern.ch/record/1095927.

[90] Richard Wigmans. *Calorimetry: Energy Measurement in Particle Physics*. Oxford University Press, Sept. 2017. ISBN: 9780198786351. DOI: 10.1093/oso/9780198786351.001.0001. URL: https://doi.org/10.1093/oso/9780198786351.001.0001.

[91] Nikiforos Nikiforou. *Performance of the ATLAS Liquid Argon Calorimeter after three years of LHC operation and plans for a future upgrade*. Tech. rep. 2013. arXiv: 1306.6756. URL: http://cds.cern.ch/record/1558820.

[92] Atlas Collaboration. "Measurement of the photon identification efficiencies with the ATLAS detector using LHC Run-1 data" (2016).

[93] Joao Pequenao. "Computer generated image of the ATLAS Muons subsystem". 2008. URL: https://cds.cern.ch/record/1095929.

[94] William Axel Leight et al. *New fitting concept in ATLAS muon tracking for the LHC Run-2*. Tech. rep. Geneva: CERN, 2018. DOI: 10.1051/epjconf/201921406006. URL: https://cds.cern.ch/record/2649597.

[95] T Kawamoto et al. *New Small Wheel Technical Design Report*. Tech. rep. ATLAS New Small Wheel Technical Design Report. 2013. URL: https://cds.cern.ch/record/1552862.

[96] ATLAS. *Design Report for the Phase-I Upgrade of the ATLAS TDAQ System*. Tech. rep. 2013. URL: https://cds.cern.ch/record/1602235.

[97] ATLAS. *ATLAS Liquid Argon Calorimeter Phase-I Upgrade: Technical Design Report*. Tech. rep. 2013. URL: https://cds.cern.ch/record/1602230.

[98] *Technical Design Report for the ATLAS Inner Tracker Pixel Detector*. Tech. rep. Geneva: CERN, 2017. DOI: 10.17181/CERN.FOZZ.ZP3Q. URL: https://cds.cern.ch/record/2285585.

[99] *Technical Design Report for the ATLAS Inner Tracker Strip Detector*. Tech. rep. Geneva: CERN, 2017. URL: https://cds.cern.ch/record/2257755.

[100] *Technical Design Report for the Phase-II Upgrade of the ATLAS TDAQ System*. Tech. rep. Geneva: CERN, 2017. DOI: 10.17181/CERN.2LBB.4IAL. URL: https://cds.cern.ch/record/2285584.

[101] Morad Aaboud et al. "Performance of the ATLAS trigger system in 2015". *The European Physical Journal C* 77.5 (2017), pp. 1–53.

[102] *ATLAS level-1 trigger: Technical Design Report*. Technical design report. ATLAS. Geneva: CERN, 1998. URL: https://cds.cern.ch/record/381429.

[103] Peter Jenni et al. *ATLAS high-level trigger, data-acquisition and controls: Technical Design Report*. Technical design report. ATLAS. Geneva: CERN, 2003. URL: https://cds.cern.ch/record/616089.

[104] *2015 start-up trigger menu and initial performance assessment of the ATLAS trigger using Run-2 data*. Tech. rep. All figures including auxiliary figures are available at https://atlas.web.cern.ch/Atlas/GROUPS/PHYSICS/PUBNOTES/ATL-DAQ-PUB-2016-001. Geneva: CERN, 2016. URL: https://cds.cern.ch/record/2136007.

[105] The ATLAS collaboration. "Operation of the ATLAS trigger system in Run 2". *Journal of Instrumentation* 15.10 (2020), P10004–P10004. DOI: 10.1088/1748-0221/15/10/p10004. URL: https://doi.org/10.1088/1748-0221/15/10/p10004.

[106] *Trigger Menu in 2017*. Tech. rep. All figures including auxiliary figures are available at https://atlas.web.cern.ch/Atlas/GROUPS/PHYSICS/PUBNOTES/ATL-DAQ-PUB-2018-002. Geneva: CERN, 2018. URL: https://cds.cern.ch/record/2625986.

[107] Martin zur Nedden. "The ATLAS trigger monitoring and operation in proton-proton collisions". *2010 17th IEEE-NPSS Real Time Conference*. IEEE. 2010, pp. 1–9.

[108] *Grafana is a multi-platform open source analytics and interactive visualization web application. It provides charts, graphs, and alerts for the web when connected to supported data sources*. Accessed: 2023-01-23.

[109] ATLAS Collaboration. *Luminosity determination in pp collisions at $\sqrt{s} = 13$ TeV using the ATLAS detector at the LHC*. ATLAS-CONF-2019-021. 2019. URL: https://cds.cern.ch/record/2677054.

[110] G Avoni et al. "The new LUCID-2 detector for luminosity measurement and monitoring in ATLAS". *Journal of Instrumentation* 13.07 (2018), P07017.

[111] Tanju Gleisberg et al. "Event generation with SHERPA 1.1". *Journal of High Energy Physics* 2009.02 (2009), p. 007.

[112] Tanju Gleisberg and Stefan Höche. "Comix, a new matrix element generator". *Journal of High Energy Physics* 2008.12 (2008), p. 039.

[113] Fabio Cascioli, Philipp Maierhöfer, and Stefano Pozzorini. "Scattering amplitudes with open loops". *Physical review letters* 108.11 (2012), p. 111601.

[114] Steffen Schumann and Frank Krauss. "A parton shower algorithm based on Catani-Seymour dipole factorisation". *Journal of High Energy Physics* 2008.03 (2008), p. 038.

[115] Stefan Höche et al. "QCD matrix elements+ parton showers. The NLO case". *Journal of High Energy Physics* 2013.4 (2013), pp. 1–22.

[116] Richard D Ball et al. "Parton distributions for the LHC Run II". *Journal of High Energy Physics* 2015.4 (2015), pp. 1–148.

[117] Simone Alioli et al. "A general framework for implementing NLO calculations in shower Monte Carlo programs: the POWHEG BOX". *JHEP* 06 (2010), p. 043. DOI: 10.1007/JHEP06(2010)043. arXiv: 1002.2581 [hep-ph].

[118] Paolo Nason. "A new method for combining NLO QCD with shower Monte Carlo algorithms". *JHEP* 11 (2004), p. 040. DOI: 10.1088/1126-6708/2004/11/040. arXiv: hep-ph/0409146.

[119] Stefano Frixione, Paolo Nason, and Carlo Oleari. "Matching NLO QCD computations with parton shower simulations: the POWHEG method". *JHEP* 11 (2007), p. 070. DOI: 10.1088/1126-6708/2007/11/070. arXiv: 0709.2092 [hep-ph].

[120] T. Sjöstrand, S. Mrenna, and P. Skands. “A brief introduction to PYTHIA 8.1”. *Comput. Phys. Commun.* 178 (2008), pp. 852–867. DOI: 10.1016/j.cpc.2008.01.036. arXiv: 0710.3820 [hep-ph].

[121] ATLAS Collaboration. *ATLAS Pythia 8 tunes to 7 TeV data*. ATL-PHYS-PUB-2014-021. 2014. URL: https://cds.cern.ch/record/1966419.

[122] Richard D. Ball et al. “Parton distributions with LHC data”. *Nucl. Phys. B* 867 (2013), p. 244. DOI: 10.1016/j.nuclphysb.2012.10.003. arXiv: 1207.1303 [hep-ph].

[123] Pierre Artoisenet et al. “Automatic spin-entangled decays of heavy resonances in Monte Carlo simulations”. *JHEP* 03 (2013), p. 015. DOI: 10.1007/JHEP03(2013)015. arXiv: 1212.3460 [hep-ph].

[124] Michal Czakon and Alexander Mitov. “Top++: A program for the calculation of the top-pair cross-section at hadron colliders”. *Comput. Phys. Commun.* 185 (2014), p. 2930. DOI: 10.1016/j.cpc.2014.06.021. arXiv: 1112.5675 [hep-ph].

[125] Michiel Botje et al. “The PDF4LHC Working Group Interim Recommendations” (2011). arXiv: 1101.0538 [hep-ph].

[126] A. D. Martin et al. “Uncertainties on α_S in global PDF analyses and implications for predicted hadronic cross sections”. *Eur. Phys. J. C* 64 (2009), pp. 653–680. DOI: 10.1140/epjc/s10052-009-1164-2. arXiv: 0905.3531 [hep-ph].

[127] J. Gao et al. “CT10 next-to-next-to-leading order global analysis of QCD”. *Phys. Rev. D* 89 (2014), p. 033009. DOI: 10.1103/PhysRevD.89.033009. arXiv: 1302.6246 [hep-ph].

[128] Aviad Roitgrund, Gad Eilam, and Shaouly Bar-Shalom. “Implementation of the manifest left–right symmetric model in FeynRules”. *Computer Physics Communications* 203 (2016), pp. 18–44.

[129] Adam Alloul et al. “FeynRules 2.0—A complete toolbox for tree-level phenomenology”. *Computer Physics Communications* 185.8 (2014), pp. 2250–2300.

[130] *X. Hoad, Summary of LRSM model updates by F. Nesti and M. Nemevsek, 2016*. https://indico.cern.ch/event/570893/contributions/2309254/attachments/1341184/2019971/20160922Modelling.pdf. Accessed: 2023-01-13.

[131] Nicola Cabibbo. “Unitary Symmetry and Leptonic Decays”. *Phys. Rev. Lett.* 10 (12 1963), pp. 531–533. DOI: 10.1103/PhysRevLett.10.531. URL: https://link.aps.org/doi/10.1103/PhysRevLett.10.531.

[132] Makoto Kobayashi and Toshihide Maskawa. “CP-Violation in the Renormalizable Theory of Weak Interaction”. *Progress of Theoretical Physics* 49.2 (Feb. 1973), pp. 652–657. ISSN: 0033-068X. DOI: 10.1143/PTP.49.652. eprint: https://academic.oup.com/ptp/article-pdf/49/2/652/5257692/49-2-652.pdf. URL: https://doi.org/10.1143/PTP.49.652.

[133] Johan Alwall et al. “The automated computation of tree-level and next-to-leading order differential cross sections, and their matching to parton shower simulations”. *Journal of High Energy Physics* 2014.7 (2014), pp. 1–157.

[134] Torbjörn Sjöstrand, Stephen Mrenna, and Peter Skands. “A brief introduction to PYTHIA 8.1”. *Computer Physics Communications* 178.11 (2008), pp. 852–867.

[135] Richard D Ball et al. “Parton distributions with LHC data”. *Nuclear Physics B* 867.2 (2013), pp. 244–289.

[136] ATLAS Collaboration. “Reconstruction of primary vertices at the ATLAS experiment in Run 1 proton–proton collisions at the LHC”. *Eur. Phys. J. C* 77 (2017), p. 332. DOI: 10.1140/epjc/s10052-017-4887-5. arXiv: 1611.10235 [hep-ex].

[137] *Vertex Reconstruction Performance of the ATLAS Detector at sqrt(s) = 13 TeV*. Tech. rep. Geneva: CERN, 2015. URL: https://cds.cern.ch/record/2037717.

[138] ATLAS Collaboration. “Electron and photon energy calibration with the ATLAS detector using 2015–2016 LHC proton–proton collision data”. *JINST* 14 (2019), P03017. DOI: 10.1088/1748-0221/14/03/P03017. arXiv: 1812.03848 [hep-ex].

[139] ATLAS Collaboration. *ATLAS Inner Detector Group*. 2017. URL: https://twiki.cern.ch/twiki/bin/view/AtlasProtected/TrackingCPMoriond2017#Vertexing (visited on 03/06/2017).

[140] ATLAS Collaboration. *ATLAS ElectronGamma Group*. 2015. URL: https://twiki.cern.ch/twiki/bin/view/AtlasProtected/ElectronGamma (visited on 05/09/2016).

[141] ATLAS Collaboration. *Electron efficiency measurements with the ATLAS detector using the 2012 LHC proton–proton collision data*. ATLAS-CONF-2014-032. 2014. URL: https://cds.cern.ch/record/1706245.

[142] ATLAS Collaboration. “Electron reconstruction and identification efficiency measurements with the ATLAS detector using the 2011 LHC proton–proton collision data”. *Eur. Phys. J. C* 74 (2014), p. 2941. DOI: 10.1140/epjc/s10052-014-2941-0. arXiv: 1404.2240 [hep-ex].

[143] Atlas Collaboration atlas. publications@ cern. ch et al. “Muon reconstruction performance of the ATLAS detector in proton–proton collision data at s s= 13 TeV”. *The European Physical Journal C* 76 (2016), pp. 1–30.

[144] Morad Aaboud et al. "Jet energy scale measurements and their systematic uncertainties in proton-proton collisions at s= 13 TeV with the ATLAS detector". *Physical Review D* 96.7 (2017), p. 072002.

[145] Matteo Cacciari, Gavin P Salam, and Gregory Soyez. "The anti-kt jet clustering algorithm". *Journal of High Energy Physics* 2008.04 (2008), p. 063.

[146] Matteo Cacciari. "FastJet: a code for fast k_t clustering, and more". *arXiv preprint hep-ph/0607071* (2006).

[147] ATLAS collaboration et al. "Jet energy scale measurements and their systematic uncertainties in proton-proton collisions at sqrt(s)= 13 TeV with the ATLAS detector". *arXiv preprint arXiv:1703.09665* (2017).

[148] Atlas Collaboration et al. "ATLAS b-jet identification performance and efficiency". *arXiv preprint arXiv:1907.05120* (2019).

[149] ATLAS Collaboration. *Optimisation and performance studies of the ATLAS b-tagging algorithms for the 2017-18 LHC run*. ATL-PHYS-PUB-2017-013. 2017. URL: https://cds.cern.ch/record/2273281.

[150] ATLAS Collaboration. "Electron and photon performance measurements with the ATLAS detector using the 2015–2017 LHC proton–proton collision data". *JINST* 14 (2019), P12006. DOI: 10.1088/1748-0221/14/12/P12006. arXiv: 1908.00005 [hep-ex].

[151] ATLAS Collaboration. "Performance of pile-up mitigation techniques for jets in pp collisions at $\sqrt{s}$ = 8 TeV using the ATLAS detector". *Eur. Phys. J. C* 76 (2016), p. 581. DOI: 10.1140/epjc/s10052-016-4395-z. arXiv: 1510.03823 [hep-ex].

[152] ATLAS Collaboration. "ATLAS b-jet identification performance and efficiency measurement with $t\bar{t}$ events in pp collisions at $\sqrt{s}$ = 13 TeV". *Eur. Phys. J. C* 79 (2019), p. 970. DOI: 10.1140/epjc/s10052-019-7450-8. arXiv: 1907.05120 [hep-ex].

[153] H. Ikeda et al. "A detailed test of the CsI(Tl) calorimeter for BELLE with photon beams of energy between 20 MeV and 5.4 GeV". *Nuclear Instruments and Methods in Physics Research Section A: Accelerators, Spectrometers, Detectors and Associated Equipment* 441.3 (2000), pp. 401–426. ISSN: 0168-9002. DOI: https://doi.org/10.1016/S0168-9002(99)00992-4. URL: https://www.sciencedirect.com/science/article/pii/S0168900299009924.

[154] M Baak et al. "HistFitter software framework for statistical data analysis". *The European Physical Journal C* 75.4 (2015), pp. 1–20.

[155] Kyle Cranmer et al. *HistFactory: A tool for creating statistical models for use with RooFit and RooStats*. Tech. rep. 2012.

[156] ATLAS Collaboration. "Measurement of the Inelastic Proton–Proton Cross Section at $\sqrt{s} = 13$ TeV with the ATLAS Detector at the LHC". *Phys. Rev. Lett.* 117 (2016), p. 182002. DOI: 10.1103/PhysRevLett.117.182002. arXiv: 1606.02625 [hep-ex].

[157] ATLAS Collaboration. "Jet energy scale measurements and their systematic uncertainties in proton–proton collisions at $\sqrt{s} = 13$ TeV with the ATLAS detector". *Phys. Rev. D* 96 (2017), p. 072002. DOI: 10.1103/PhysRevD.96.072002. arXiv: 1703.09665 [hep-ex].

[158] ATLAS Collaboration. "Performance of electron and photon triggers in ATLAS during LHC Run 2". *Eur. Phys. J. C* 80 (2020), p. 47. DOI: 10.1140/epjc/s10052-019-7500-2. arXiv: 1909.00761 [hep-ex].

[159] ATLAS Collaboration. "Muon reconstruction and identification efficiency in ATLAS using the full Run 2 pp collision data set at $\sqrt{s} = 13$ TeV" (2020). arXiv: 2012.00578 [hep-ex].

[160] ATLAS Collaboration. "Jet energy scale and resolution measured in proton–proton collisions at $\sqrt{s} = 13$ TeV with the ATLAS detector" (2020). arXiv: 2007.02645 [hep-ex].

[161] ATLAS Collaboration. "Measurement of the c-jet mistagging efficiency in $t\bar{t}$ events using pp collision data at $\sqrt{s} = 13$ TeV collected with the ATLAS detector". *Eur. Phys. J. C* 82 (2021), p. 95. DOI: 10.1140/epjc/s10052-021-09843-w. arXiv: 2109.10627 [hep-ex].

[162] "Tools for estimating fake/non-prompt lepton backgrounds with the ATLAS detector at the LHC" (Nov. 2022). arXiv: 2211.16178 [hep-ex].

[163] ATLAS Collaboration. "Search for type-III seesaw heavy leptons in dilepton final states in pp collisions at $\sqrt{s} = 13$ TeV with the ATLAS detector". *Eur. Phys. J. C* 81 (2021), p. 218. DOI: 10.1140/epjc/s10052-021-08929-9. arXiv: 2008.07949 [hep-ex].

[164] Michiel Botje et al. "The PDF4LHC Working Group Interim Recommendations" (2011). DOI: 10.48550/ARXIV.1101.0538. URL: https://arxiv.org/abs/1101.0538.

[165] L. A. Harland-Lang et al. "Parton distributions in the LHC era: MMHT 2014 PDFs". *The European Physical Journal C* 75.5 (May 2015). DOI: 10.1140/epjc/s10052-015-3397-6. URL: https://doi.org/10.1140%5C%2Fepjc%5C%2Fs10052-015-3397-6.

[166] Sayipjamal Dulat et al. "New parton distribution functions from a global analysis of quantum chromodynamics". *Phys. Rev. D* 93 (3 Feb. 2016), p. 033006. DOI: 10.1103/PhysRevD.93.033006. URL: https://link.aps.org/doi/10.1103/PhysRevD.93.033006.

[167] Manuel Bähr et al. “Herwig++ physics and manual”. *The European Physical Journal C* 58.4 (Nov. 2008), pp. 639–707. DOI: 10.1140/epjc/s10052-008-0798-9. URL: https://doi.org/10.1140%5C%2Fepjc%5C%2Fs10052-008-0798-9.

[168] Glen Cowan et al. “Asymptotic formulae for likelihood-based tests of new physics”. *The European Physical Journal C* 71.2 (2011), pp. 1–19.

[169] A L Read. “Presentation of search results: the CLs technique”. *Journal of Physics G: Nuclear and Particle Physics* 28.10 (2002), p. 2693. DOI: 10.1088/0954-3899/28/10/313. URL: https://dx.doi.org/10.1088/0954-3899/28/10/313.